POLITECNICO DI MILANO
DIPARTIMENTO DI ELETTRONICA, INFORMAZIONE E BIOINGEGNERIA
DOCTORAL PROGRAMME IN INFORMATION TECHNOLOGY

AUTONOMOUS DRIVING AT THE LIMITS OF HANDLING

Doctoral Dissertation of:
Marco Baur

Supervisor:
Prof. Luca Bascetta

Tutor:
Prof. Simone Garatti

The Chair of the Doctoral Program:
Prof. Barbara Pernici

2019 – XXXI

Acknowledgments

There are several people who deserve to be mentioned.

Firstly, I owe a huge and sincere thank you to prof. Luca Bascetta, for the help, the support and the advice he has given me during this work.

Secondly, I would like to thank professor Gianni Ferretti for the trust he has given me, which has represented a great motivation for me.

A special thanks goes to my wife, Sara, who has always been supportive, especially in difficult and stressful moments.

Thanks to my father, Luciano, who helped me in building the experimental platform.

Thanks also to all master students who decided to do their thesis on the topics covered in my PhD research project: Filippo, Carlo, Federico.

To conclude, I thank my PhD mates, with whom I have spent and enjoyed many days in the department.

A PhD is not just research, it is an incredibly harsh but wonderful life experience, a journey into yourself.

Thanks to all

Abstract

To be safer than their human counterparts, automatic pilots must be able to control the car up to its limits of handling. Therefore, this PhD thesis focuses on the analysis and design of autonomous vehicles path tracking controllers, able of exploiting all the grip made available by tyre-ground interaction. In particular, two subtopics have been investigated. Firstly, attention has been devoted to path tracking controllers able to manage the so-called drifting technique, which consists of taking a turn in the presence of large values of vehicle sideslip angle and counter-steering. Such an aggressive and complex manoeuvre is typically used by expert rally drivers to go as fast as possible on low-grip terrains, but it has also been recognized as a driving technique expanding vehicle mobility, and it can be potentially adopted for autonomous emergency obstacle avoidance manoeuvres. In light of this, an autonomous drifting stabilization controller has been designed and experimentally tested. Then, the proposed approach has been extended to let the vehicle autonomously follow a circular trajectory while keeping in a sustained drifting dynamic equilibrium. Secondly, the analysis of a control oriented model, originally conceived by a Stanford research group, to simplify the design of a path tracking controller which is able of exploiting all the grip made available by tyre-ground interaction, has been carried out. This model is a variant of the well-known single-track model, featured by front tyre lateral force as the control input, in place of front tyre steering angle. This allows to easily (say linearly) express the hard saturation constraint on the lateral force developed by front tyre, which is dictated by tyre-ground friction coefficient. However, undamped

yaw rate oscillations, the so-called fish tail phenomenon, occurs when operating the vehicle at high speed. Therefore, a control-oriented analysis of this affine in the control input model, which explains and analytically demonstrates the reason behind the fish tailing phenomenon, has been conducted. After that, a possible solution to the previously described problem has been proposed and assessed, by means of simulations performed on a realistic multibody Dymola vehicle. Last but not least, to effectively test the proposed control strategies, a dedicated experimental platform, which consists in a 1:10 scale radio controlled car, made autonomous by the addition of a set of sensors (inertial measurement unit, odometer, marker for an optical motion tracking system) and processing units (Arduino, Odroid XU4), has been designed and assembled. A nonlinear single-track model has been used to describe the vehicle dynamics: its parameters have been measured or identified and its accuracy has been assessed. The dynamic similarity between the scaled car and a real vehicle, which has been verified, allows to use this setup as a realistic experimental setup for the evaluation of the proposed control strategies.

Contents

CHAPTER 1

Introduction

Many car makers, among all Ford, BMW, Mercedes, Toyota and FCA [52], with the novel addition of AI giants like Google and Apple, are investing a lot of resources to develop fully autonomous cars, with the promise of a dramatic decrease in accidents and of a revolution in the road mobility sector: people will not own cars anymore, but will temporarily rent autonomous ones just to be brought to their destination. This enormous breakthrough in the automotive sector looked like to be coming soon, i.e., by 2020, but in a recent interview released at the 2017 Las Vegas CES event [1], Gill Pratt, the CEO of the Toyota Research Institute, revealed that car makers are still far from reaching the top level of the SAE scale of on-road vehicle driving automation [55]. Many ethic, legal and technical problems have still to be solved to really bring the expected improvements in car safety.

The generic architecture of an autonomous car is usually made of three layers:

1. **perception layer**, accounts for the perception of the surrounding environment (obstacles detection) and for the measurement and estimation of vehicle states and parameters;

2. **path planning layer**, takes as input the data coming from the perception layer and outputs a reference trajectory which should in principle allow the vehicle to safely traverse the environment and reach the destination. More specifically, we can distinguish between the global path planner, which substantially accounts for the navigation of the vehicle, and the local path planner, which accounts for the generation of a local trajectory which satisfies kynodynamic constraints posed by vehicle non-holonomic dynamics, by actuator saturation limits and by obstacles. Moreover, the generated trajectory should satisfy passenger comfort constraints, which usually translates into limited longitudinal and lateral acceleration;

3. **control layer** computes control input to follow the reference trajectory generated by the path planner, while rejecting disturbances acting on the vehicle, while being robust to parameter uncertainties, and while taking into account kinematic, dynamic and passenger comfort constraints.

Today, most of the technical challenges currently dwell into perception and planning layers, which means autonomous perception of obstacles and prediction of the behaviour of other cars, pedestrians and even cyclists, as described, for example, in [23]. Nevertheless, unsolved problems can also be found in the control layer, and the present work aims at addressing some of them. In particular, this PhD thesis aims at overcoming some of the limiting assumptions under which most of the path tracking controllers which can be found in the literature, along with ADAS[1] [53], have been developed. In particular, we are mainly referring to the following two assumptions:

- small vehicle sideslip angle[2]. This assumption is not satisfied when the car drifts due to, for example, a sudden decrease of rear wheel friction coefficient, which may be the result of a wet or icy road patch.
- linear relation between tyre lateral force and slip angle[3]. This hypothesis is only valid for small values of the tyre slip angle. Therefore, automatic drivers leveraging on it cannot take advantage of all grip made available by tyre-ground interaction. This fact is restrictive when the car is traveling on a low grip terrain, as for instance a wet road, and when a suddenly appeared obstacle has to be avoided to prevent a collision.

[1] Advanced Driver Assistance System
[2] For the definition of vehicle sideslip angle, the interested reader can refer to Chapter 2.
[3] For the definition of tyre slip angle, the interested reader can refer to Chapter 2.

These two assumptions hold only in a normal driving condition, i.e., far from the limits of vehicle handling. However, we strongly believe that an automatic driver, to be really safer than his human counterpart, has to overcome these assumptions, being able to exploit all the grip made available by tyre-ground interaction and to hold car control even in the presence of a large sideslip angle.

To study the problem of autonomous driving in the presence of large vehicle sideslip angles, this work focuses on drifting manoeuvres. Drifting is an aggressive manoeuvre, which brings the car close to its limits of handling, and which is characterized by a large vehicle sideslip angle, countersteer and throttle action, for the control of vehicle lateral dynamics. The interest for this manoeuvre is justified by the fact that it is not only used by rally drivers on slippery terrains, but sometimes it is the only viable option to avoid an obstacle in an emergency condition [32]. In addition, drifting expands vehicle mobility capabilities at low speeds [62], giving the opportunity to navigate through tight spaces.

The autonomous execution of a drifting manoeuvre represents a complex control problem, due the multiple number of inputs and outputs, the saturation constraints on the control inputs, and the nonlinearities of the underlying dynamics. This work leverages on Linear Quadratic (LQ) control strategy to design a drifting stabilization controller. Though several works have already used this control approach for drifting stabilization, the following novel aspects characterize this thesis:

- differently from the other works which are present in literature, we used the same control input available to a human driver, namely front tyre steering angle and longitudinal force developed by rear tyres. The latter of these is related to torque delivered by motor, which, in turn, is linked to throttle command;
- for the first time, to the best of authors' knowledge, LQ approach has been extended to perform, simultaneously, drifting stabilization and tracking of a circular path;
- last but not least, LQ controllers have been tested by means of extensive experimental campaigns, aimed at assessing their performance, robustness and shortcomings. These experiments have highlighted the robustness of the LQ control approach in stabilizing drifting and in tracking a circular reference path.

To perform experimental tests, a dedicated setup was built for the purpose of this PhD research project. It consists of a Radio Controlled (RC) 1:10 scaled car, which has been made autonomous by the addition of sensors and computational units. To be able to design model based controllers, a model of steering actuator dynamics and of vehicle lateral and longitudinal dynamics were identified, and their parameters were estimated. Validation experiments highlighted that single-track vehicle dynamic model, which is typically used for the design of ADAS and real car path tracking controllers, is able to reproduce vehicle lateral dynamics, up to the limits of handling. To further confirm that a scaled vehicle, in place of a real car, can be used to assess performances, robustness and shortcomings of path tracking controllers, while avoiding the danger and the cost of accidental collisions, the dynamic similitude between the experimental platform and a real vehicle has been verified.

Apart from drifting, a control-oriented model, suitable to the development of path tracking controllers able to take advantage of all the grip made available by tyre-ground interaction, has been studied. This model, which is called Affine in the Force Input (AFI) model, takes front tyre lateral force as control variable, in place of front tyre steering angle. This implies that:

- nonlinearities of front tyre lateral force and front tyre slip angle relationship are extracted out from vehicle lateral dynamic model, yielding a linear dynamical system;
- constraints on maximum and minimum front tyre lateral force, which are dictated by tyre-ground friction coefficient and tyre normal load, are easily expressed as lower and upper bounds on the control input.

Therefore, AFI model is suited to the design of linear path tracking controllers, which are able to take advantage of the maximum lateral force which can be developed by tyres. In particular, AFI naturally calls for the adoption of a linear Model Predictive Control (MPC) approach, for the design of path tracking controllers.
AFI benefits come at the expense of yaw rate oscillations, which arise when vehicle is traveling at high speed and front tyre lateral force is the control variable. These oscillations severely hamper passenger comfort by giving to him the impression of an impending spinning and, hence, must be avoided. A novel aspect of this work lies in the analysis and explanation of the cause of these yaw rate fluctuations, which have never been addressed so far. It has been discovered that, by controlling front tyre lateral force, a hidden pole placement control law, which decreases yaw rate damping

at high speed, is applied. Then, it has been shown, by means of simulations, that undamped yaw rate dynamics not only affects system open loop response, but also the performance which can be achieved with a MPC path tracking controller. Therefore, a solution increasing the damping of yaw rate poles at high speed was proposed. In particular, a pole placement control law was designed and added to MPC path tracking controller. Simulations showed that these nested loops control architecture is able to track a reference path, while using all the grip made available by tyre-ground interaction, without yaw rate oscillations when vehicle is traveling at high speed.

This PhD thesis is organized as follows:

- **Chapter 2** presents vehicle analytical dynamic models, which are used to design model based vehicle path tracking controllers. Furthermore, this chapter also describes the multi-body vehicle models which have been used to test control algorithms which are presented in the next chapters.
- **Chapter 3** illustrates the experimental platform which has been built for the purpose of this PhD research project, along with the estimation of its parameters and the identification of steering actuator and vehicle lateral dynamic model.
- **Chapter 4** describes a drifting stabilization and circular path tracking controller, that is able of holding car control in sustained drifting condition. An extensive experimental campaign, aimed at assessing controller performance, robustness and shortcomings have been performed.
- **Chapter 5** analyses a dynamic model which allows to easily design a linear path tracking controller, that is capable of exploiting all the grip made available by tyre-ground interaction. As it is shown, this model suffers from poor damping of yaw rate dynamics when vehicle is traveling at high speed. An in-depth analysis of the cause of this phenomenon and a possible solution to it is presented and discussed.
- **Chapter 6** draws conclusions and illustrates future developments of this work.

CHAPTER 2

Vehicle dynamic models

Designing a control system under the model based control framework, which has been adopted throughout this work, a model of the controlled system is required. When available, as in the case of vehicle dynamics, an analytical dynamic model derived from first principles is the most straightforward choice. Therefore, such a kind of model has been extensively used in this work.

In the literature, the following vehicle dynamic models can be found:

- **kinematic models** have two great advantages: they are dependent only upon car geometric parameters, that can be easily measured, and they are not singular at zero velocity. On the other hand, they effectively reproduce vehicle dynamics when forces generated by tyre are small [27]. As a consequence, they correctly model vehicle dynamics only at low speed, and in the absence of aggressive manoeuvres, as, for example, in the presence of parking manoeuvres and none-emergency manoeuvres [15, 34]

- **dynamic models** can represent vehicle complex dynamics which arise during the execution of aggressive and high speed manoeuvres. On the other hand, they depend upon a model of tyre forces, whose pa-

rameters are difficult to be identified, and which vary with type and condition (dry, wet, etc) of the surface onto which the car is traveling. Most used vehicle dynamic models are the following:

- point-mass model, as the one used in [25] and in [2], neglects vehicle yaw dynamics at the advantage of simplicity, but at the expense of model accuracy;
- linear single-track model, also referred to as "bicycle"model [33], models car lateral dynamic under the simplifying assumptions of constant or slowly varying longitudinal speed, linear tyre model, small sideslip and steering angle, and neglectable lateral load transfer. It is a widely used model for the design of automatic lane-keeping controllers [17] and ADAS [53];
- nonlinear single-track model relaxes the hypothesis made for linear single-track model, with the exception of the neglection of the lateral load transfer, an assumption intrinsic to the single-track paradigm. This model has been used for the design of several nonlinear path tracking controllers, for the execution of emergency manoeuvres, as in [39, 40];
- nonlinear full-track model considers four wheels and therefore takes into account lateral load transfer. It is the most accurate analytical dynamic model which has been used so far for the design of path tracking controllers. However, its accuracy comes at the expense of simplicity, being a nonlinear model. Examples of the adoption of this model can be found in [14, 24].

As this work is focused on the autonomous execution of aggressive manoeuvres, which bring the car up to its limits of handling, only vehicle dynamic models have been considered.

2.0.1 Full-track vehicle dynamic model

In the following, the derivation of an analytical model of the in-plane motion of a car-like (non-holonomic) vehicle is presented. We firstly define all the quantities involved and the sign conventions. Fig. 2.1 illustrates a full-track vehicle model, with all kinematic and dynamic quantities sketched with positive sign. Two reference systems are shown, namely:

- a global, or earth fixed, inertial [28] reference system $\{X, Y\}$;
- a local, relative and non-inertial reference system $\{x, y\}$, fixed at vehicle Center Of Gravity (COG), and whose x axis is aligned to vehi-

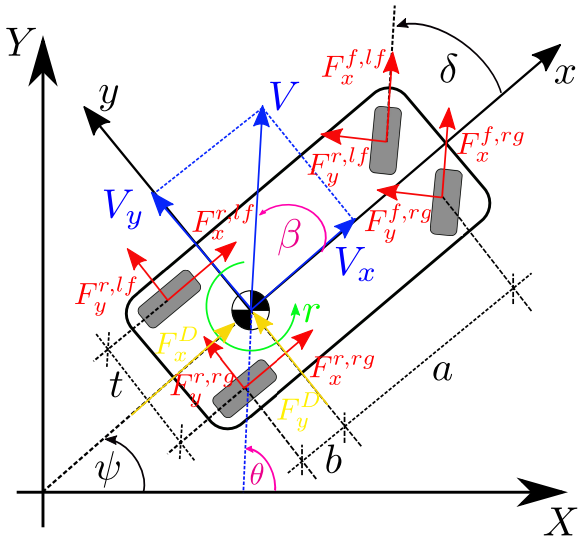

Figure 2.1: *Full-track vehicle model*

cle roll axis. The so-called European sign convention [27] has been adopted, which prescribes a positive y axis towards the left of the vehicle, in contrast to the SAE convention which assumes a positive y axis towards the right of the vehicle [54].

Coherently with the European sign convention, rotations are positive when counterclockwise for both these reference systems.
The following kinematic quantities are defined:

- the angle between X and x axis, called vehicle attitude or orientation angle and denoted as ψ;
- vehicle absolute speed V, whose components along the x and y axis are V_x and V_y, respectively. The angle between vehicle roll (x) axis and V is the so-called vehicle sideslip angle β, while the angle between X and V is the so-called course angle [64], which is given by

$$\theta = \psi + \beta; \tag{2.1}$$

- yaw rate r, i.e., the angular speed of the vehicle along the vertical z;
- the angle between x axis and the roll axis of the tyre, the so-called front-wheel steering angle[1] δ.

[1] Rear-wheel steering vehicles will not be considered in this work, as the vast majority of cars are not equipped with this technology, despite the considerable improvements of vehicle lateral stability and low-speed maneuverability [2].

Geometrical parameters are:

- a and b, the distance of the front and rear axle from the COG, respectively. Their sum, which yields vehicle wheelbase, is denoted as l;
- vehicle track t, which is approximated as constant along the whole vehicle length.

Inertial parameters are:

- vehicle mass m;
- vehicle yaw moment of inertia J_z.

Last but not least, dynamic quantities are:

- $F_y^{i,j}$ is the lateral force developed by each tyre, where $i = \{f, r\}$ with f and r meaning front and rear axle, respectively, and where $j = \{l, r\}$ with lf and rg meaning left and right wheel, respectively;
- $F_x^{i,j}$ is the longitudinal force developed by each tyre;
- F_x^d and F_y^d, additional external, longitudinal and lateral forces acting at vehicle COG which account for aerodynamic drag force, and the components of vehicle weight which act on the vehicle when it is traveling on a slope or banked road. These forces have been considered as disturbances acting on the vehicle, that have to be rejected by the control systems of the longitudinal and lateral dynamics.

Vehicle dynamic equations expressed in the local reference frame, which are typically used for designing model-based path tracking and lateral stability automotive controllers [53] as they are free of trigonometric functions and hence can be easily linearized [27], can be obtained by projecting the dynamic equations in the global reference frame onto the local reference frame. The advantage of this procedure lies in the fact that the global reference frame, as already stated before and in contrast to the local relative reference frame, is an inertial reference frame, hence Newton and Euler equations can be easily obtained:

$$m\ddot{X} = F_X \tag{2.2}$$

$$m\ddot{Y} = F_Y \tag{2.3}$$

$$J_z\ddot{\psi} = M_z \tag{2.4}$$

where F_X and F_Y summarize the total force in the X and Y directions, respectively, and M_z is the total yaw moment. Yaw moment equilibrium

equation (2.4) keeps the same in the relative reference frame, therefore we focus only on translational motion equations (2.2), (2.3). Rotation matrix $[R(\psi)]$

$$[R(\psi)] = \begin{bmatrix} \cos\psi & -\sin\psi \\ \sin\psi & \cos\psi \end{bmatrix} \tag{2.5}$$

can be exploited to project the velocities components in the local reference frame into the global reference frame, as follows:

$$\begin{bmatrix} \dot{X} \\ \dot{Y} \end{bmatrix} = [R(\psi)] \begin{bmatrix} V_x \\ V_y \end{bmatrix} \tag{2.6}$$

Then, by deriving with respect to time eq. (2.6), one obtains

$$\begin{aligned} \ddot{X} &= -\dot{\psi}V_x \sin\psi + \dot{V}_x \cos\psi - \dot{\psi}V_y \cos\psi - \dot{V}_y \sin\psi \\ \ddot{Y} &= \dot{\psi}V_x \cos\psi + \dot{V}_x \sin\psi - \dot{\psi}V_y \sin\psi + \dot{V}_y \cos\psi, \end{aligned}$$

which can be recasted as

$$\begin{bmatrix} \ddot{X} \\ \ddot{Y} \end{bmatrix} = [R(\psi)] \begin{bmatrix} \dot{V}_x - \dot{\psi}V_y \\ \dot{V}_y + \dot{\psi}V_x \end{bmatrix}. \tag{2.7}$$

Now, let's project tyre forces from the local into the global reference frame:

$$\begin{bmatrix} F_X \\ F_Y \end{bmatrix} = [R(\psi)] \begin{bmatrix} F_x \\ F_y \end{bmatrix}. \tag{2.8}$$

By simplifying the common term in equations (2.7) and (2.8), i.e., the rotation matrix, and by substituting $\dot{\psi}$ with $= r$, the dynamic motion equations in the local reference frame are finally obtained:

$$\begin{aligned} m\left(\dot{V}_x - rV_y\right) &= F_x \\ m\left(\dot{V}_y + rV_x\right) &= F_y \\ J_z\dot{r} &= M_z \end{aligned} \tag{2.9}$$

In eq. (2.9), F_x, F_y are the total forces acting on the x and y axis, respectively, which can be computed, along with M_z, as follows:

$$\begin{aligned}
F_x = \quad & \left[F_x^{r,l} + F_x^{r,r}\right] + \left[\left(F_x^{f,l} + F_x^{f,r}\right)\cos\delta - \left(F_y^{f,l} + F_y^{f,r}\right)\sin\delta\right] + \\
& + F_x^d \\
F_y = \quad & \left[F_y^{r,l} + F_y^{r,r}\right] + \left[\left(F_y^{f,l} + F_y^{f,r}\right)\cos\delta + \left(F_x^{f,l} + F_x^{f,r}\right)\sin\delta\right] + \\
& + F_y^d \\
M_z = \quad & \left[\left(F_y^{f,l} + F_y^{f,r}\right)\cos\delta a - \left(F_y^{r,l} + F_y^{r,r}\right) b\right] + \\
& + \left[\left(F_x^{f,l} + F_x^{f,r}\right)\sin\delta a\right] + \left[\left(F_x^{f,r} - F_x^{f,l}\right)\cos\delta\frac{t}{2}\right] + \\
& + \left[\left(F_x^{r,r} - F_x^{r,l}\right)\frac{t}{2}\right] + \left[\left(F_y^{f,l} - F_y^{f,r}\right)\sin\delta\right] + M_z^d
\end{aligned} \tag{2.10}$$

where M_z^d is a term which includes all the yaw moments which may act as disturbances on the vehicle, as for example the momentum impressed by lateral wind, considering that typically the center of pressure is not coincident with the COG, or an asymmetric brake force distribution due to a different friction coefficient among the two wheels of each axle, as it happens in the ISO μ-split dynamic test [36].
Eq. (2.9) along with eq. (2.10) define the so-called full-track vehicle dynamic model, since they take into account all vehicle wheels. Moreover, eq. (2.9) can also be expressed as follows, by recalling the second law of dynamics:

$$\begin{aligned}
\dot{V}_x &= a_x + rV_y \\
\dot{V}_y &= a_y - rV_x \\
\dot{r} &= \frac{M_z}{J_z}
\end{aligned} \tag{2.11}$$

2.0.2 Tyre force models

Tyre force model is the most important source of uncertainty, due to its nonlinearity and to the difficulties faced when identifying its parameters, which continuously change with road conditions.

Tyre longitudinal force models

Tyre longitudinal force is a nonlinear function of longitudinal slip σ, which is defined as

$$\sigma = \frac{w_w - w_w^0}{w_w^0} \tag{2.12}$$

where w_w is the measured wheel angular speed and w_w^0 is the theoretical wheel angular speed, calculated as the ratio between V_x and R_w, with R_w as wheel radius. It follows that, to use any longitudinal tyre model, the state equation of wheel rotational dynamics has to be included into the dynamic model of the vehicle. In particular, for each wheel a state equation can be formulated as:

$$J_w \dot{w}_w = T - F_x R_w \tag{2.13}$$

in which J_w is the moment of inertia of the wheel, T is the torque applied to the wheel by either the motor or the brake. In this work, in order to neglect the four wheel dynamic state equations, the longitudinal force developed by the traction tyre has been considered as the control input to the vehicle longitudinal dynamics. This can be done only if the torque delivered by the brakes and by the motor is controllable, which is the case for a combustion engine and, for an electric drive, when the current of the motor is the electrical quantity being controlled by the throttle. Moreover, it is supposed that the response time of this inner control loop is small enough, compared to vehicle longitudinal and lateral dynamics, to be neglected. In addition to this, the assumption of controlling F_x leaves room for low-level traction and anti-lock braking systems, which act at higher frequency with respect to a path tracking controller and which consequently works with σ.

Tyre lateral force models

Tyre lateral force models express $F_y^{i,j}$ as a nonlinear function of tyre slip angle $\alpha^{i,j}$, which is defined as the angle between tyre roll axis and tyre speed vector, as exemplified by Fig. 2.2, and which is computed as follows:

$$\alpha^{i,j} = \beta_w^{i,j} - \delta^{i,j} = \tan^{-1}\left(\frac{V_y^{i,j}}{V_x^{i,j}}\right) - \delta^{i,j}, \tag{2.14}$$

in which $\beta_w^{i,j}$ is tyre sideslip angle and $\delta^{i,j}$ is tyre steering angle. Eq. (2.14)

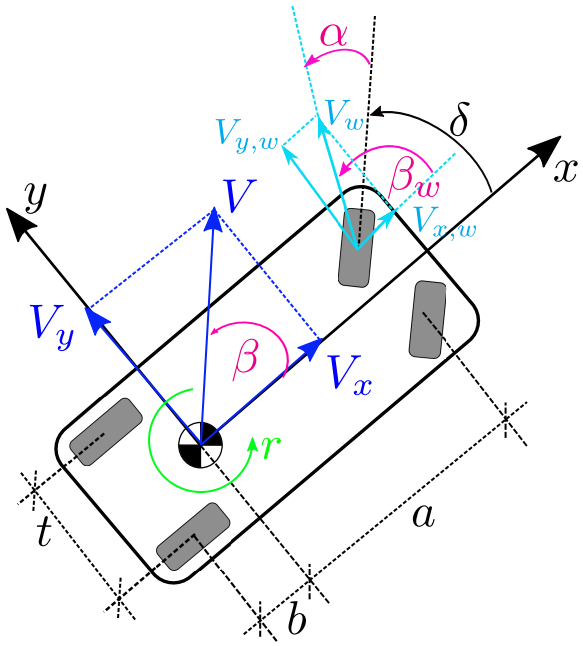

Figure 2.2: *Front tyre slip angle*

becomes, for each wheel:

$$
\begin{aligned}
\alpha^{f,l} &= \tan^{-1}\left(\frac{V_y + ra}{V_x - r\frac{t}{2}}\right) - \delta \\
\alpha^{f,l} &= \tan^{-1}\left(\frac{V_y + ra}{V_x + r\frac{t}{2}}\right) - \delta \\
\alpha^{r,l} &= \tan^{-1}\left(\frac{V_y - rb}{V_x - r\frac{t}{2}}\right) \\
\alpha^{r,r} &= \tan^{-1}\left(\frac{V_y - rb}{V_x + r\frac{t}{2}}\right).
\end{aligned}
\tag{2.15}
$$

When a single-track model is adopted, front and rear axle slip angles are computed as:

$$\begin{aligned} \alpha^f &= \tan^{-1}\left(\frac{V_y + ra}{V_x}\right) - \delta \\ \alpha^r &= \tan^{-1}\left(\frac{V_y - rb}{V_x}\right). \end{aligned} \tag{2.16}$$

The following simplifying assumptions allow to obtain linear slip angle equations:

- front tyre steering angle is assumed to be small, so that $\cos\delta \simeq 1$;
- vehicle sideslip angle is assumed to be small, namely $\cos\beta \simeq 1$. Consequently $\beta \simeq \dfrac{V_y}{V_x}$.

Thus, eq. (2.16) becomes

$$\begin{aligned} \alpha^f &\simeq \left(\frac{V_y + ra}{V_x}\right) - \delta \\ \alpha^r &\simeq \left(\frac{V_y - rb}{V_x}\right), \end{aligned} \tag{2.17}$$

or, equivalently

$$\begin{aligned} \alpha^f &\simeq \left(\beta + \frac{ra}{V_x}\right) - \delta \\ \alpha^r &\simeq \left(\beta - \frac{rb}{V_x}\right). \end{aligned} \tag{2.18}$$

The simplest lateral force model is the linear one:

$$F_y = -C_\alpha \alpha, \tag{2.19}$$

in which C_α is the slope of the tangent into the origin of the $\alpha - F_y$ curve, the so-called cornering stiffness. This model is generally adopted when the car is not traveling at its limits of handling, as the linear model loses its validity when lateral force approaches its saturation limit, which is dictated by the product between tyre normal load and tyre-ground friction coefficient. Cornering stiffness is a function of several physical parameters, as for example tyre inflate pressure [27]. In particular, cornering stiffness is

said to be linearly dependent upon tyre normal load [27] and tyre-ground friction coefficient [49].
Apart from the linear model, several lateral force models are present in the literature. They can be divided into analytical models, which are derived from first principles, and empirical models, which are directly fitted from experimental data.
A well-known analytical model is the brush model, which is derived starting from the assumption of a parabolic pressure distribution along tyre-ground contact patch [53]. Fiala model is a variant of brush model [38]:

$$F_y = \begin{cases} -C_\alpha z + \eta C_\alpha |z| z - \frac{1}{3}\eta^2 C_\alpha z^3, & |z| < \tan(\alpha_{sl}) \\ -\mu F_z sgn(\alpha), & |z| \geq \tan(\alpha_{sl}) \end{cases} \tag{2.20}$$

where

$$\alpha_{sl} = \tan^{-1}\left(\frac{1}{\eta}\right) \qquad z = \tan(\alpha) \qquad \eta = \frac{C_\alpha}{3\mu F_z}$$

The main advantage of this lateral force model lies in being dependent only upon a little bunch of physical parameters, namely cornering stiffness, tyre normal load and tyre-ground friction coefficient μ. This makes the Fiala model a perfect candidate for control oriented models. In addition to this, in [63] an extension of (2.20) was presented, which takes into account the difference between the peak and sliding friction coefficients.
Among empirical tyre force models, Pacejka model, also referred to as magic formula model, is the most famous one. The interested reader can refer to [27, 53] for a brief introduction and to [48] for a comprehensive description of this model, which is typically used in simulation, rather than for control purposes, due to its accuracy, which comes at the expense of simplicity.

Tyre combined force models

The maximum friction force which can be developed by each tyre is limited by the friction circle constraint:

$$F_x^2 + F_y^2 \leq (\mu F_z)^2 \tag{2.21}$$

Hence, eq. (2.21) must be taken into account when considering a combined force model, i.e. a force model which accounts for the interaction between longitudinal and lateral tyre forces, which are not negligible when traveling at the limits of handling.
In [35], an extended version of Fiala model (2.20) has been presented to

consider the friction circle constraint, by means of the so-called derating factor ξ:

$$F_y = \begin{cases} -C_\alpha z + \eta C_\alpha |z| z - \frac{1}{3}\eta^2 C_\alpha z^3, & |z| < \tan(\alpha_{sl}) \\ -\xi \mu F_z sgn(\alpha), & |z| \geq \tan(\alpha_{sl}) \end{cases} \tag{2.22}$$

where

$$\alpha_{sl} = \tan^{-1}\left(\frac{1}{\eta}\right) \qquad z = \tan(\alpha) \qquad \eta = \frac{C_\alpha}{3\xi\mu F_z}$$

$$\xi = \frac{\sqrt{(\mu F_z)^2 - F_x^2}}{\mu F_z}$$

It can be observed that longitudinal tyre force enters directly into eq. (2.22). Combined Pacejka model, which is a function of σ. which is defined by eq. (2.12), in place of F_x, reproduces with a higher accuracy the interaction between tyre forces, at the expense of simplicity. Therefore, as for lateral force models, Pacejka combined force models are generally adopted for simulation purposes, rather than for control purposes. A simplified version of the magic formula model was proposed and used for control design in [31]. However, such a model, despite being simpler, is still relying on a set of parameters which do not have a physical meaning, so in our opinion it does not bring significant benefits with respect to the combined Fiala model (2.22).

2.0.3 Nonlinear single-track vehicle dynamic model

In the field of automotive automatic drivers and lateral stability controllers, a common assumption is to neglect the effect of lateral load transfer, so that a simplified single-track dynamic model is obtained [53]. The single-track model, also referred to as bicycle model [33], takes its name from the fact that the wheels of each axle are shrunk into a fictitious wheel, as illustrated by Fig. 2.3. Lateral load transfer effect is negligible when vehicle lateral acceleration is low, which may not be true in emergency maneuvers. However, by taking into account any load transfer model, as the ones described in section 2.0.5, a nonlinear vehicle dynamic model is unavoidably obtained, even if a linear tyre model is used, and therefore more complex nonlinear control techniques are needed.
In accordance with the bicycle assumption, eq. (2.10) is simplified as fol-

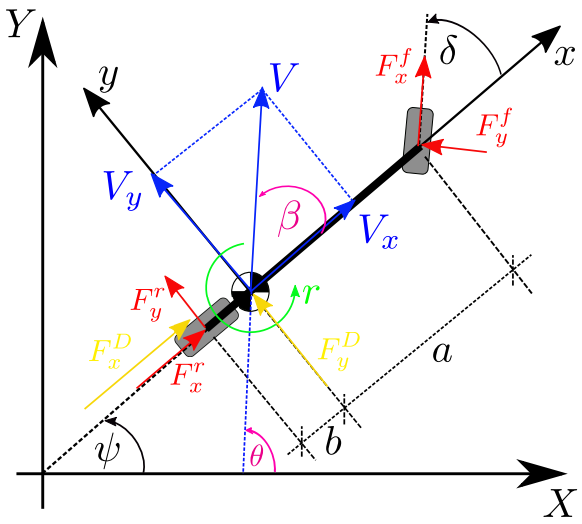

Figure 2.3: *Single-track model scheme*

lows:

$$\begin{aligned} F_x &= F_x^r + F_x^f \cos\delta - F_y^f \sin\delta + F_x^d \\ F_y &= F_y^r + F_y^f \cos\delta + F_x^f \sin\delta + F_y^d \\ M_z &= aF_y^f \cos\delta - bF_y^r + M_z^d \end{aligned} \tag{2.23}$$

Therefore, nonlinear single-track model is obtained adding eq. (2.9) to eq. (2.23).

2.0.4 Linear single-track vehicle dynamic model

A very commonly adopted model for the design of path tracking controllers and lateral stability controllers is the linear single-track model [53]. The linearity of this model can also be exploited to perform stability analysis of closed loop systems.
The linear single-track dynamic model is obtained by starting from the non-linear single-track model derived in section 2.0.3, and by making the following simplifying assumptions:

- longitudinal speed is assumed to be constant (or slowly varying), so that it can be considered as a parameter (or a slowly varying parameter, so that a linear time-varying system is obtained). This assumption allows to neglect longitudinal load transfer and, obviously, the state equation of longitudinal speed in eq (2.9);

- sideslip and steering angles are assumed to be small, namely

$$\cos\beta \simeq 1$$
$$\cos\delta \simeq 1;$$

and consequently

$$\beta \simeq \frac{V_y}{V_x}$$
$$\dot{\beta} \simeq \frac{\dot{V}_y}{V_x};$$

- linear lateral tyre force model, given by eq. (2.19) is used.

Consequently, the state equations of the linear single-track vehicle lateral dynamic model are:

$$\begin{aligned}\dot{V}_y &= -\left(\frac{C_\alpha^f + C_\alpha^r}{mV_x}\right)V_y + \left(\frac{-C_\alpha^f a + C_\alpha^r b}{mV_x} - V_x\right)r + \left(\frac{C_\alpha^f}{m}\right)\delta + \frac{F_y^d}{m}\\ \dot{r} &= \left(\frac{-C_\alpha^f a + C_\alpha^r b}{J_z V_x}\right)V_y - \left(\frac{C_\alpha^f a^2 + C_\alpha^r b^2}{J_z V_x}\right)r + \left(\frac{C_\alpha^f a}{J_z}\right)\delta + \frac{M_z^d}{J_z}\end{aligned} \tag{2.24}$$

when assuming V_y and r as state variables, and

$$\begin{aligned}\dot{\beta} &= -\left(\frac{C_\alpha^f + C_\alpha^r}{mV_x^2}\right)\beta + \left(\frac{-C_\alpha^f a + C_\alpha^r b}{mV_x^2} - 1\right)r + \left(\frac{C_\alpha^f}{mV_x}\right)\delta + \frac{F_y^d}{m}\\ \dot{r} &= \left(\frac{-C_\alpha^f a + C_\alpha^r b}{J_z}\right)\beta - \left(\frac{C_\alpha^f a^2 + C_\alpha^r b^2}{J_z V_x}\right)r + \left(\frac{C_\alpha^f a}{J_z}\right)\delta + \frac{M_z^d}{J_z}\end{aligned} \tag{2.25}$$

when considering β and r as state variables.

2.0.5 Load transfer models

Longitudinal and lateral accelerations trigger load transfer and suspension motion, which govern roll and pitch dynamics. Load transfer models are useful for computing the current normal force which is acting on each wheel, which dictates, along with tyre-ground fritction coefficient, the maximum friction force that can be developed by a tyre. It is important to stress that, by considering any load transfer model, vehicle dynamic equations will unavoidably be nonlinear. This is the reason why load transfer is usually neglected in the design of a vehicle control-oriented model.

Two types of load transfer model can be developed.
A quasi-steady state load transfer model, which considers only the effects of the accelerations while leaving out the effects of suspension motion. In such a model, wheel normal loads are computed as follows [62]:

$$\begin{aligned} F_z^{f,lf} &= F_z^{f,static} - \Delta F_z^{y,f} - \Delta F_z^x \\ F_z^{f,rg} &= F_z^{f,static} + \Delta F_z^{y,f} - \Delta F_z^x \\ F_z^{r,lf} &= F_z^{r,static} - \Delta F_z^{y,r} + \Delta F_z^x \\ F_z^{r,rg} &= F_z^{r,static} + \Delta F_z^{y,r} + \Delta F_z^x, \end{aligned} \tag{2.26}$$

where the static load (acting on each wheel) is given by

$$\begin{aligned} F_z^{f,static} &= \frac{1}{2}\frac{mgb}{l} \\ F_z^{r,static} &= \frac{1}{2}\frac{mga}{l}, \end{aligned} \tag{2.27}$$

the lateral load transfer is computed as

$$\begin{aligned} \Delta F_z^{y,f} &= \frac{mh_{COG}b}{lt}a_y \\ \Delta F_z^{y,r} &= \frac{mh_{COG}a}{lt}a_y, \end{aligned} \tag{2.28}$$

with h_{COG} as the height of the COG, and finally the longitudinal load transfer is given by

$$\Delta F_z^x = \frac{mh_{COG}}{2l}a_x. \tag{2.29}$$

The effect of a lateral or longitudinal known slope can be included into this quasi-steady state load transfer model, by adding the projection of the gravity acceleration in the lateral and longitudinal direction to a_y and a_x, respectively. Moreover, a_x and a_y can be expressed as a function of vehicle dynamic states and control inputs:

$$\begin{aligned} a_x &= \frac{F_x}{m} \\ a_y &= \frac{F_y}{m}; \end{aligned} \tag{2.30}$$

A more detailed load transfer model, which takes into account suspension motion and hence roll and pitch dynamics. This model has not been considered in this work, since roll and pitch dynamics are usually neglected

in the design of path tracking and lateral stability controllers [53]. The interested reader can refer to [30] for an analytical model of these out of plane dynamics.

2.0.6 Path tracking state equations

Path tracking state equations model vehicle dynamics with respect to a reference path, which is either the lane center line or the output of a local planner, as illustrated by Fig. 2.4. In particular, state equations are usu-

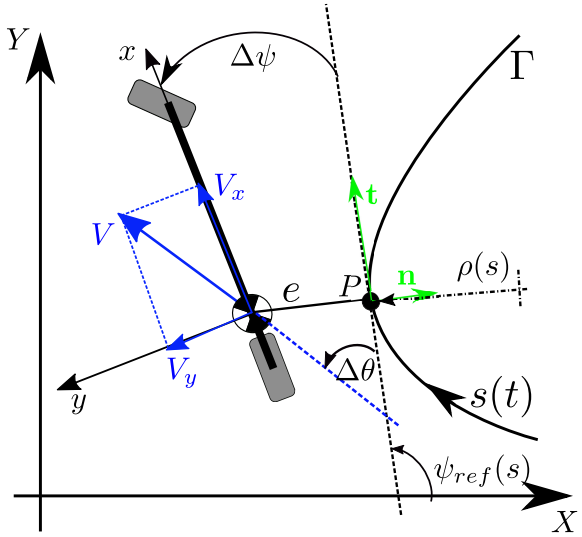

Figure 2.4: *Single-track vehicle model along with path tracking kinematic quantities*

ally formulated in Frenet reference frame [16], which is basically a relative right-handed reference system, fixed to the reference path and whose normal axis **n** is normal to the reference path and pointing towards the inside of the turn. Along with Frenet coordinate system, other quantities are represented in Fig. 2.4, namely:

- Γ is the reference path;
- e is the path tracking error, i.e., the distance between vehicle COG and P, a point lying on Γ and which can be thought of as the reference vehicle position;
- s is Γ curvilinear abscissa, i.e., the position of P along Γ;

- $\rho(s)$ is Γ curvature radius at P, which is assumed to be known. More in details, control engineers generally models it as a known, or measured external disturbance. Often, curvature $\kappa(s) = 1/\rho(s)$ is adopted;
- $\Delta\psi$ is the attitude angle error, i.e., the angle between vehicle attitude angle ψ and Γ attitude angle ψ_{ref}, which is defined by Frenet tangent vector $\mathbf{t}$;
- $\Delta\theta$ is the course angle error, i.e., the angle between V and θ_{ref}, which is equal to ψ_{ref}.

Frenet reference frame is generally preferred over the global reference frame shown in Fig. 2.4, since, under some simplifying assumptions, path tracking error dynamic equations are linear, as it will be shown later.
Three state variables are needed to completely describe the dynamics of the car with respect to Γ, given that a rigid body has three degrees of freedom in the 2-D space. The most common choice for path tracking state variables is the triplet $(\Delta\psi,\ e,\ s)$, which yields the following nonlinear path tracking state equations:

$$\begin{aligned} \dot{\Delta\psi} &= r - r_{ref} \\ \dot{e} &= V_x \sin(\Delta\psi) + V_y \cos(\Delta\psi) \\ \dot{s} &= \frac{1}{1 - \kappa(s)\, e} V_{\parallel}^{\Gamma}, \end{aligned} \tag{2.31}$$

where $V_{\parallel}^{\Gamma}$ is the component of V parallel to Γ at P, which is computed as

$$V_{\parallel}^{\Gamma} = V_x \cos(\Delta\psi) - V_y \sin(\Delta\psi), \tag{2.32}$$

and where r_{ref} is the reference yaw rate, which is computed as

$$r_{ref} = \kappa(s)\dot{s}. \tag{2.33}$$

It is interesting to understand the structure of s dynamics: the term which multiplies $V_{\parallel}^{\Gamma}$ has been introduced to take into account the fact that, when e is different from zero, the car is not traveling onto the reference path but on a shifted path. The following relation holds:

$$\frac{l}{\rho} = \frac{l_{car}}{\rho_{car}}, \tag{2.34}$$

where l is travelled arch length on Γ, l_{car} is travelled arc length on current car trajectory, whose curvature is ρ_{car}^{-1}. Then, by differentiating with respect

to time eq. (2.34), one obtains:

$$\frac{\dot{l}}{\rho} = \frac{\dot{l}_{car}}{\rho_{car}}, \tag{2.35}$$

which can be rewritten as

$$\dot{s} = \frac{\rho}{\rho_{car}} \dot{s}_{car}. \tag{2.36}$$

By substituting $\dot{s}_{car}$ with $V_{\parallel}^{\Gamma}$, ρ with $1/\kappa(s)$ and $\rho_{car} = \rho - e$ into eq. (2.36), the s dynamics in (2.31) is obtained. Path tracking state equations (2.31) are linear when the following hypothesis hold:

- $\Delta\psi$ is small, so that $\cos(\Delta\psi) \simeq 1$ and $\sin(\Delta\psi) \simeq \Delta\psi$;
- V_x is constant, a common assumption when dealing with the so-called lane-keeping controllers, which are especially used when driving along highways [53];
- e is small, so that the term before $V_{\parallel}^{\Gamma}$ can be neglected.

Consequently, path tracking error dynamics becomes:

$$\begin{aligned} \dot{\Delta\psi} &= r - V_x \kappa(s) \\ \dot{e} &= V_x(\Delta\psi) + V_y \\ \dot{s} &= V_x. \end{aligned} \tag{2.37}$$

Another way of deriving a linear path tracking state equation, which has been adopted in [53] and can be found in the literature of lane following controllers as in [49], is by differentiating with respect to time the path tracking error dynamic equation reported in eq. (2.31):

$$\ddot{e} = \dot{V}_x \sin(\Delta\psi) + V_x \cos(\Delta\psi)\,\dot{\Delta\psi} + \dot{V}_y \cos(\Delta\psi) - V_y \sin(\Delta\psi)\,\dot{\Delta\psi}. \tag{2.38}$$

By making the assumption of small $\Delta\psi$ angle, one obtains the following expression:

$$\ddot{e} \simeq \dot{V}_x \Delta\psi + V_x \dot{\Delta\psi} + \dot{V}_y - V_y \Delta\psi \dot{\Delta\psi}. \tag{2.39}$$

Then, by neglecting the last term of eq. (2.39), which is an infinitesimal of greater order, and by assuming a constant longitudinal speed, the following linear state equation is obtained:

$$\ddot{e} = V_x \dot{\Delta\psi} + \dot{V}_y. \tag{2.40}$$

Now, by expliciting the expression of $\dot{\Delta\psi}$ in eq. (2.40), and by recalling eq. (2.11), the following result is obtained:

$$\begin{aligned} \ddot{e} &= V_x\,(r - r_{ref}) + \dot{V}_y = \\ &= V_x r - V_x r_{ref} + (a_y - r V_x) = \\ &= a_y - a_y^{ref}, \end{aligned} \tag{2.41}$$

in which

$$a_y^{ref} = V_x r_{ref}, \tag{2.42}$$

and with a_y computed according to eq. (2.30). By adopting eq. (2.41) as the state equation for the path tracking error, path tracking state variables translate into the triplet $(e, \dot{e}, s)$. Finally, path tracking state equations can also be formulated with respect to the triplet of state variables $(\Delta\theta,\, e,\, s)$ and with reference to vehicle absolute speed vector V as follows:

$$\begin{aligned} \dot{\Delta\theta} &= \dot{\theta} - \dot{\theta}_{ref} \\ \dot{e} &= V \sin(\Delta\theta) \\ \dot{s} &= \frac{1}{1 - \kappa(s)\, e} V_{\parallel}^{\Gamma}, \end{aligned} \tag{2.43}$$

where

$$V_{\parallel}^{\Gamma} = V \cos(\Delta\theta) \tag{2.44}$$

$$V = \sqrt{V_x^2 + V_y^2} \tag{2.45}$$

$$\dot{\theta} = r + \dot{\beta} \tag{2.46}$$

$$\dot{\theta}_{ref} = r_{ref}. \tag{2.47}$$

2.1 Vehicle multi-body model

As already pointed out, analytical models are good at providing an explanation of the physics involved in vehicle motion. Moreover, they are the best choice for the design of a model based controller and, when linear, are also useful for performing stability analysis. However, to carefully assess the performance of a control system, tests must be performed over a more accurate model. To this purpose, two Modelica[2] multi-body vehicle models, taken from the Vehicle Dynamics Library (VDL) developed by Modelon[3], have been used. In particular, these models reproduce two Rear-Wheel-Driven (RWD) electric powered car, namely a sedan and a compact

[2] https://www.modelica.org/

[3] https://www.modelon.com/library/vehicle-dynamics-library/

vehicle. Both models includes powertrain, suspension and braking system dynamics, along with aerodynamic effects and tyre stiffness. A combined slip magic formula model [48] accounts for tyre-ground interaction, while ground friction coefficient can be tuned in order to test the vehicle on multiple surfaces. Finally, payloads can be added to account for passengers and luggages on rooftop and inside trunk. To perform simulation tests, the model has been exported out of the Dymola environment and subsequently imported into the Simulink environment. Model inputs are:

- the steering wheel angle, which is translated into front wheel steering angle by means of a linear gain, called $K_{s.w.}$;
- a normalized throttle command, i.e. a command in the range $[-1, +1]$ where $+1$ means that the electric motor is developing its maximum torque in the forward direction, while for a command equal to -1 in the backward direction (negative torque);
- brake pedal force.

Model outputs are:

- longitudinal and lateral speed and acceleration at the center of gravity;
- roll, pitch and yaw angular speed;
- roll and pitch angles;
- center of gravity absolute position;
- vehicle attitude or orientation angle;
- sideslip angle at the center of gravity;
- tyre longitudinal, lateral and normal force.

Vehicle single-track model parameters, which are summarized in Table 2.1, have been estimated by running an identification experiment contained into the Vehicle Dynamics Library.

Table 2.1: *Multibody vehicle data*

	Sedan	Compact
m [Kg]	1659	1197
J_z $\left[\mathrm{Kg\,m^2}\right]$	2817	1510
a [m]	1.22	1.07
b [m]	1.48	1.40
μ	1	1
C_α^f $\left[\mathrm{N\,rad^{-1}}\right]$	86781	72660
C_α^r $\left[\mathrm{N\,rad^{-1}}\right]$	75515	58075
$K_{s.w.}$	11.8521	17.9827

CHAPTER 3

The experimental platform

In general, any experimental campaign offers a more realistic environment compared to any accurate multi-body simulation, allowing to effectively assess controller performance, robustness, and shortcomings. On the other hand, the execution of aggressive autonomous maneuvers on a real vehicle reveals to be dangerous, from the safety point of view, and expensive, due to accident risk and the need for a dedicated test track. Therefore, as a compromise between these two opposite considerations, a scaled autonomous vehicle has been built from scratch for the purpose of this PhD research project. The idea of testing autonomous vehicle control algorithms on a scaled car is not new. In fact, it has already been exploited by several research groups. For example, [11] describes one of the first works using a scaled car for the purpose of testing vehicle control algorithms. A detailed analysis based on Pi theorem was conducted to assess the dynamic similitude between a scaled car and a real vehicle. In [43], 1:43 Rear-Wheel-Driven (RWD) scaled cars have been used by ETH researchers to test Model Predictive Control (MPC) in order to follow a reference path while avoiding static and moving obstacles. A camera mounted above the track provided, with the addition of an extended Kalman filter, the estimate of vehicle position, velocity and yaw rate at a frequency of $100\,Hz$. The

controller was run on a desktop computer and the computed control inputs were sent via Bluetooth to the car, onto which only low-level actuators control loops were running. In [65], Georgia Tech researches took advantage of a fifth-scale rally vehicle to test a variant of MPC, called path integral MPC, which allows to solve in real-time the nonlinear path tracking optimization problem in presence of nonlinear dynamics, which arise as a consequence of aggressive maneuvers. More in details, this experimental platform is characterized by powerful hardware computational units which allow to perform all the calculations directly onboard, without the aid of external devices. Vehicle dynamic states are estimated thanks to installed sensors, i.e., encoder for longitudinal speed measurement, an Inertial Measurement Unit (IMU) for yaw rate, lateral and longitudinal acceleration measurements, a GPS for the estimation of vehicle position along the track, and a vision system which, coupled with a dedicated estimation algorithm, provides information regarding the surrounding environment at a frequency of $60\,Hz$. In [18] a 1:8 scaled All-Wheel-Driven (AWD) car has been built to assess the performance of a coordinated lateral and longitudinal vehicle dynamics control strategy, aimed at helping a human driver in controlling the vehicle at high speed and at the limits of handling. The vehicle was equipped with a IMU and a motor Hall effect speed sensor, whose measurements have been fused together to estimate vehicle longitudinal speed. The control algorithm was run onboard on a dedicated Embedded Control Unit (ECU), running at $100\,Hz$. In [31, 37, 66] a 1:10 scaled car has been used to test autonomous drifting controllers. The car was equipped with an IMU and a camera, which was used to estimate vehicle lateral and longitudinal velocity. Finally, in [5], three scaled cars have been utilized to verify an intersection collision avoidance system. Feedback of position is provided by 6 cameras mounted on the top of the test track, while an encoder measures vehicle speed.

3.1 The scaled car

A 1:10 RWD scaled autonomous car has been built for the purpose of this PhD research project.
The choice of a RWD experimental platform has been driven by the following considerations. Firstly, a Forward-Wheel-Driven (FWD) vehicle cannot perform sustained drifting, which requires the action of a tractive longitudinal force on rear tyres to keep a constant vehicle longitudinal speed. Secondly, it is much more difficult to drift a RWD vehicle than an AWD vehicle. In other words, we wanted to test our drifting controller in the

worst condition to highlight controller robustness, performances and shortcomings.
The platform comes from a RC RWD car, namely a Sakura D4 RWD[1], which has been made autonomous by adding sensors and computational units. Fig. 3.1 illustrates its first configuration, while Fig. 3.2 and 3.3 portray its most recent configuration, which is characterized by a more rational distribution of hardware components. The car features four independent suspensions, with fully adjustable geometries and angles. A belt transmission, along with a rear differential, transferring motor torque to rear wheels. Two different sets of tyre, which are shown in Fig. 3.4 are available, namely a set of drifting, low grip tyre, and a set of rubber tyre, which offers higher grip.

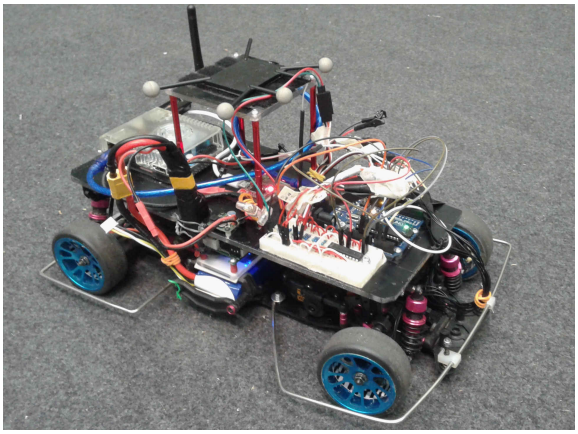

Figure 3.1: *Experimental platform first configuration*

3.1.1 Electric motor and motor control board

The scaled car is driven by an electric brushless motor, equipped with three hall sensors, which provide a feedback of rotor position. Motor, along with hardware devices, are powered by a three cell LiPo battery. A picture of the motor[2] is shown in Fig. 3.5, while motor parameters are listed in Table 3.1. In particular, motor torque constant K_t has been computed starting from the parameters generally given by RC motor manufacturers, namely motor speed constant K_ω, which corresponds to the number of motor revolutions in a minute for a unitary voltage applied. This parameter is nothing but the

[1] https://www.3racing.it/sakura-d4-rwd/
[2] taken from http://www.hobbyqueenitalia.com/prodotto-144829/Turnigy-TrackStar-105T-Sensored-Brushless-Motor-3250KV.aspx

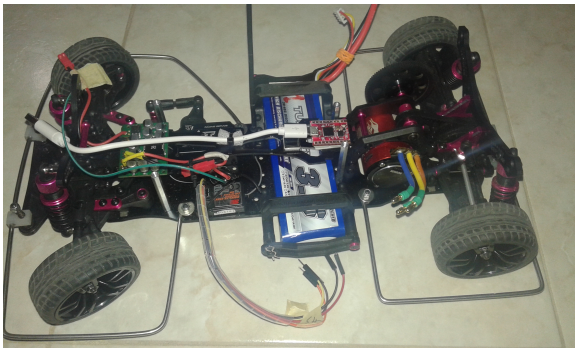

Figure 3.2: *Experimental platform most recent configuration: chassis view*

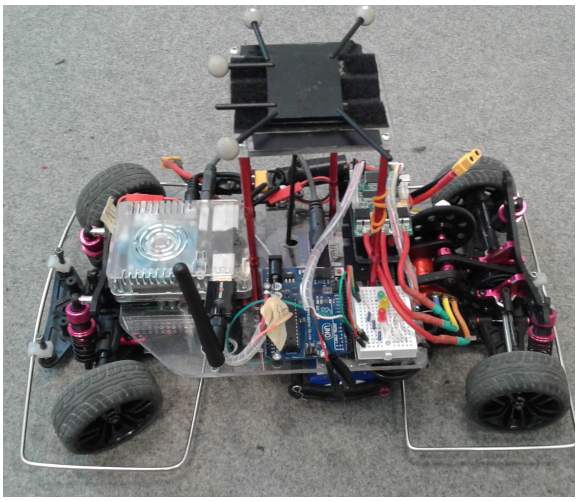

Figure 3.3: *Experimental platform most recent configuration*

(a) *Drifting tyre* **(b)** *Rubber tyre*

Figure 3.4: *Scaled car tyre sets*

Table 3.1: *Scaled car brushless motor parameters*

m [Kg]	0.158
V_{in} [V]	7.4-11.1
I_{max} [A]	26
P_{max} [W]	290
k_ω $\left[\mathrm{rpmV}^{-1}\right]$	3250
K_t $\left[\mathrm{NmA}^{-1}\right]$	$2.93\,10^{-3}$

inverse of motor electric constant K_e. Therefore, the following formula has been used:

$$K_t \left[\frac{Nm}{A}\right] = K_e \left[\frac{V}{rad\,s^{-1}}\right] = \frac{1}{K_\omega \left[\frac{rad}{s\,V}\right]} = \frac{1}{K_\omega \left[\frac{rpm}{V}\right] \frac{2\pi}{60}}$$

Interestingly, Fig. 3.6 shows that motor back electromotive force profile,

Figure 3.5: *The brushless motor which equips the experimental platform*

which has been obtained by measuring motor phase to phase voltage when manually turning it, is sinusoidal.
At the time this research project began, RC Electronic Speed Control (ESC) boards were controlling motor speed with a Pulse-Width-Modultated (PWM) voltage signal, whose duty cycle was the control variable. It follows that this speed regulator were, in practice, not controlling neither motor speed nor its current, but merely the voltage that was applied to motor phases. To control either motor speed or motor current, VESC motor control board[3], which is shown in Fig. 3.7, has been adopted. In fact, this board, which

[3] http://vedder.se/2015/01/vesc-open-source-esc/

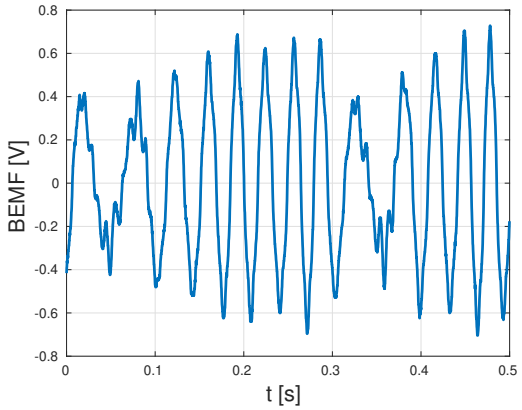

Figure 3.6: *Brushless motor back electromotive force profile*

in the meanwhile has start spreading also across RC world, allow to select different motor control strategies: duty cycle, speed control and current control. We used speed control for the tests that required to keep an almost constant car speed, while motor current control has been used for autonomous drifting, as it will be explained in the second chapter of this work. To improve the performance of the motor control strategy, we leveraged on motor hall sensors and use the Field Oriented Control (FOC) strategy, which provides smoother current and speed profiles compared to a traditional trapezoidal voltage profile.
Motor speed or current is set by means of a standard RC PWM signal, which is received by VESC and converted to a normalized throttle command which varies in the interval $[-1, +1]$, where $+1$ means maximum speed or current (which are set by the user). More in detail, a standard RC PWM signal consist of a train of square impulses, whose frequency is fixed to $60\,Hz$ while the high-voltage time varies in the interval $[1000, 2000]\ \mu s$, with $1500\,\mu s$ as the neutral (zero) point.

3.1.2 Transmission

Motor torque is transmitted to rear wheels through a belt transmission. More in detail, the transmission features two speed reduction stages, whose

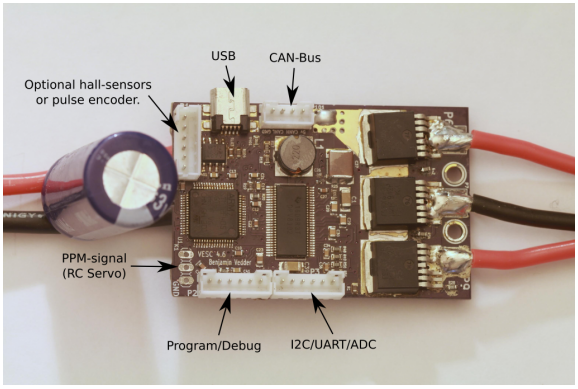

Figure 3.7: *VESC electronic control board*

transmission ratio τ has been determined by the following formulae:

$$\tau_{1-2} = \frac{\omega_2}{\omega_1} = \frac{z_1}{z_2} \tag{3.1}$$

$$\tau_{3-4} = \frac{\omega_4}{\omega_3} = \frac{z_3}{z_4}, \tag{3.2}$$

in which ω_i is shaft rotational speed while z_i is the number of teeth of the i-th pulley. Then:

$$\tau = \tau_{1-2}\,\tau_{3-4}.$$

Finally, motor current I is mapped to the total longitudinal force developed by rear tyres through the following formula:

$$F_x^r = \frac{I\,K_t}{\tau\,R_w}, \tag{3.3}$$

in which R_w is wheel radius. Table 3.2 lists the values of the aforementioned transmission parameters.

3.1.3 Steering actuator

Car steering actuation is provided by a standard RC servo, where the commanded steering angle is received as a standard RC PWM signal. Initially, a slower servo was used (Savox 1225MG). Then, as newer and faster servos become available on the marked, a faster and more powerful servo, SRT BH 8015[4], has been adopted, which is shown in Fig. 3.8. Servo is powered from car LiPo battery, with a step-down voltage converter splitting the pair.

[4] http://www.srt-rc.com/index.php?id=43

Table 3.2: *Transmission parameters*

z_1	22
z_2	92
τ_{1-2}	0.239
z_3	16
z_4	39
τ_{3-4}	0.410
τ	0.09799
R_w [m]	0.0245

Figure 3.8: *SRT BH 8015 steering servo*

3.2 Sensors and state estimation

In order to successfully operate a path tracking controller, the following states has to be measured or estimated:

- vehicle longitudinal velocity V_x;
- vehicle lateral velocity V_y, or sideslip angle β;
- vehicle yaw rate r;
- vehicle absolute position (X, Y), or vehicle position with respect to the reference trajectory $(e, \Delta\psi)$.

Vehicle yaw rate r, along with lateral and longitudinal accelerations, are directly measured onboard, at a frequency of $100\,Hz$, with an Attitude Heading Reference System (AHRS)[5]. In particular, compared to an IMU, an AHRS is equipped with a gyroscope, which provides vehicle roll and pitch angles, which are used to compute the correct values of yaw rate and accelerations.
All the other states are online estimated, starting from the measurements of a 12-camera OptiTrack motion tracking system[6], which gives car position at a frequency of $100Hz$. To this purpose, a reflective marker has been put on the rooftop of the car, as shown in Fig. 3.3. Then, velocities are estimated by differentiating with respect to time two consecutive car positions.

3.3 Hardware and Software configuration

The "brain"of the scaled car consists of an embedded PC Odroid XU4[7], that runs a ROS[8] control architecture. Low level communication between Odroid and actuators (steering servo and VESC, which are commanded through standard RC PWM signals) is managed by means of an Arduino Uno board, connected via serial link to Odroid and running at $100\,Hz$. The Arduino board also transmits manual commands sent to the car to the Odroid. In fact, the car can be either manually controlled with a standard RC radio system, or can autonomously drive. Fig. 3.9 shows a sketch of hardware car configuration, along with exchanged ROS topics. In particular, there is one ROS node in charge of serial communication management,

[5] https://www.hardkernel.com/shop/myahrs/
[6] https://optitrack.com/products/motive/
[7] https://wiki.odroid.com/odroid-xu4/odroid-xu4
[8] https://www.ros.org/

one that receives AHRS messages, and another one that receives motion tracking messages in real time through a wi-fi connection[9].

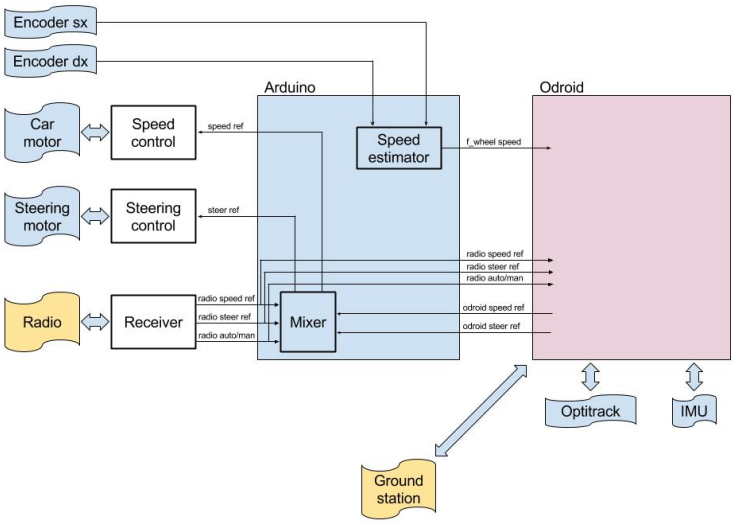

Figure 3.9: *Scaled car hardware configuration*

3.4 Actuator dynamics identification

Actuator dynamics have to be known in advance in order to properly design path tracking controllers. In the following, the identification of their dynamics is presented.

3.4.1 Steering actuator dynamics identification

The kinematic relationship between servo angular position and car steering angle is nonlinear and unknown. In addition to this, standard RC servos do not provide a feedback of their angular position, which is regulated to the reference value set by a standard RC PWM signal by servo internal digital controller. Therefore, the map between PWM pulse width and car steering angle δ had to be identified as well. The following experimental procedure was adopted: the car has been run in circle, with constant speed and steering angle, and the following kinematic relationship has been exploited to

[9]More in details, a dedicated ROS node has been developed in the context of this thesis. In particular, such a node takes advantage of a unicast streaming protocol to receive data coming from OptiTrack in real-time

estimate car steering angle [27]:

$$\delta = \frac{a+b}{R}, \tag{3.4}$$

where R is the radius of the traveled path, a and b are the distance from vehicle COG of front and rear axle, respectively. As eq. (3.4) is valid under the hypothesis of negligible lateral forces developed by tyres, the car has been running at the lowest possible speed, setting the VESC in the speed control mode. Path radius R has been estimated by fitting a circumference to the measured position points with the algorithm presented in [51]. Fig. 3.10 illustrates the map obtained with the faster servo. The following considerations can be made:

- the map is almost linear ($R^2 = 0.991$), as nonlinearities arise only at large values of commanded steering angle. Based on this consideration, a linear map, which converts the desidered car steering angle δ into the corresponding PWM pulse width, has been adopted;
- steering angle is non zero at PWM neutral point ($1500\,\mu s$). This is due to the fact that when assembling the servo one cannot avoid an angular misalignment with respect to its neutral position. Moreover, this implies that if the servo is disassembled from the car, the identification of the PWM - steering angle map has to be done again. A video[10] shows the offset of the misalignment which is automatically done when the car is turned on;
- maximum achieved steering angle is not equal for left and right direction. This is due to steering mechanism asymmetry: servo is located on the right of the car, so it is closer to the right wheel. This generates different mechanical backlash between the two wheels and, consequently, different maximum steering angles in the two directions;
- steering mechanism mechanical backlash constitutes a great source of uncertainty over the value of the steering angle, which call for greater robustness of the developed control algorithms. A video[11] shows such phenomenon.

After that, servo dynamics had to be identified. As standard RC servos do not provide a feedback of their angular position, motion tracking system marker had been fixed to front steering wheels, and its angular rotation in response to a step command has been recorded and used to fit a

[10] Available at `https://youtu.be/qHcYwNGMlKc`
[11] Available at `https://youtu.be/nKepLd3HZPs`

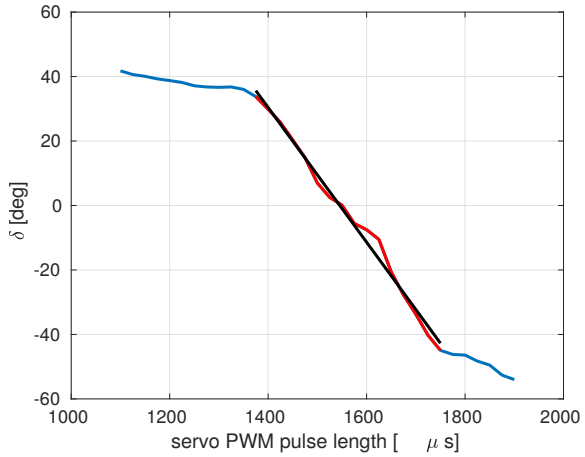

Figure 3.10: *Steering servo PWM - steering angle map (measured data as blue line, portion of data used for linear model fitting as red line, linear fitted model as black line)*

model of servo dynamics, as shown in a video of the experiment[12]. Servo dynamic behavior has been identified when the car was standing still; this represents a worst-case scenario, as servo response will certainly be faster when the car is traveling, due to the reduction of the tyre-ground friction force as a consequence of rolling. Fig. 3.11 shows faster servo normalized step response, along with the dynamic model $A_s(s)$ which best fitted experimental data, namely a second order model, with a couple of complex conjugate poles ($\xi = 0.75$, $\omega_n = 87.62\, rad\, s^{-1}$):

$$A_s(s) = e^{-\tau_s s} \frac{1}{\frac{s^2}{\omega_n^2} + \frac{2\xi}{\omega_n} s + 1}.$$

Hence, faster servo bandwidth is approximately equal to $14\, Hz$, a quite satisfactory value for the steering actuator of an autonomous car, which typically has a bandwidth of no more than $10\, Hz$, as for example in [49, 52]. Fig. 3.11 also highlighted that the steering servo is affected by a large delay, in particular $0.065\, s$ in that test performed with the car lying on the ground and standing still. However, we expected this delay to be lower when the car is moving. Therefore, a test aimed at correctly identifying steering servo delay has been performed: the car has been accelerated up

[12] available at `https://youtu.be/MYW9SXZtk0Y`. This video illustrates, for clarity purposes, the experiment performed with the car upside down, i.e. with wheels not touching ground

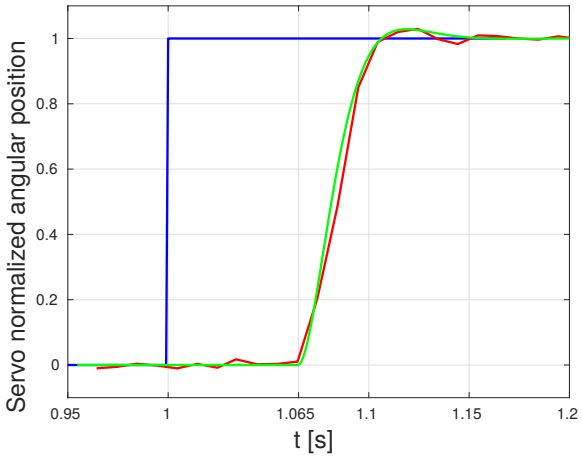

Figure 3.11: *Faster steering servo unitary step response (reference, measured and simulated angular position as blue, red and green line, respectively)*

to a constant speed and then a step on the steering angle has been commanded to the servo. The yaw rate response, in place of motion tracking system measurements (which are affected by wi-fi communication delay), has been used to assess servo delay, as illustrated in Fig. 3.12, which was found to be equal to $0.055\,s$ (and, hence, $0.01\,s$ is the delay of motion tracking system measurements due to the wi-fi communication). However, it is important to understand that what has been really estimated is not the delay of the servo, but the delay of the servo with the addition of the transmission delay of servo command signal. In fact, when the step reference signal is generated from the reference generator node in the Odroid, its signal has to pass through the serial port, which is working at $100\,Hz$, then it has to be received by the Arduino, which is working at $100\,Hz$ and, finally, it is transmitted to the servo with the standard RC PWM signal, which works at $60\,Hz$. So, we can assume that transmission delay corresponds to $0.01 + 0.01 + 1/60\,s$, for a total delay of $0.037\,s$. Therefore, the delay of the steering actuator is equal to $0.018\,s$. This value is close to the delay of the servos used in [18] and in [12], which represent, to the best of authors' knowledge, the only examples of work in which RC servo delay has been estimated.
Servo dynamic model is

$$A_s(s) = e^{-\tau_s s} \frac{1}{\frac{s^2}{\omega_n^2} + \frac{2\xi}{\omega_n} s + 1}, \tag{3.5}$$

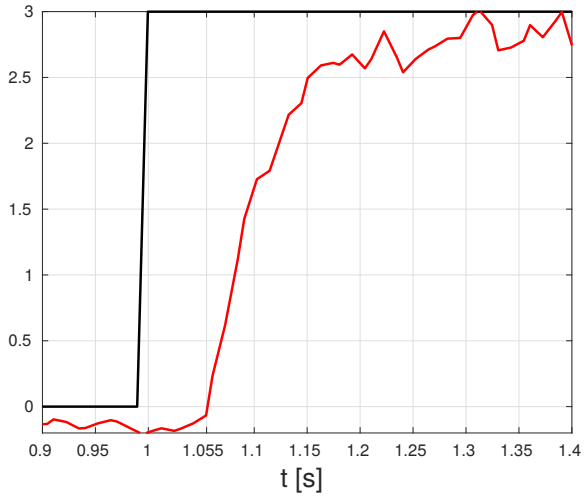

Figure 3.12: *Steering servo delay estimation (normalized commanded steering angle as black line, measured yaw rate, expressed in $rad\,s^{-1}$, as red line)*

Table 3.3: *Faster steering servo dynamic model parameters*

Model Order	II
ω_n $\left[\mathrm{rad\,s^{-1}}\right]$	87.62
ξ	0.75
τ_s [s]	0.018
Transmission delay [s]	0.037

where parameters take the value listed in Table 3.3. An analogue analysis has been conducted also for the older and slower servo. Its dynamic transfer function is the following:

$$A_s(s) = e^{-\tau_s s}\frac{1}{T_s s + 1}, \tag{3.6}$$

where parameters take the values listed in Table 3.4. In particular, servo bandwidth was equal to $8\,Hz$ and servo delay was significantly larger.

Table 3.4: *Slower steering servo dynamic model parameters*

Model Order	I
T_s [s]	0.125
τ_s [s]	0.053
Transmission delay [s]	0.037

3.4.2 Motor dynamics identification

The dynamics of the motor could not be identified, due to the lack of a motor speed sensor, which could have provided motor angular speed. Longitudinal speed measurements coming from motion tracking system and longitudinal acceleration measurements coming from AHRS are too noisy and not fast enough to capture the faster motor dynamics. Therefore, we assumed that motor dynamics is fast enough to be neglected and the delay associated to it is simply the transmission delay, which, as already explained in Section 3.4.1, is equal to $0.037\ s$. This approximation is more valid when the current of the motor, hence its torque, is the controlled variable, as speed transients are longer.

3.5 Nonlinear single-track model parameters estimation

Model based control leverages on a model of the system to be controlled. Therefore, in order to be able to control the scaled car, a dynamic model of its lateral dynamics had to be identified. Given its widespread use in the automotive field, single-track model, which was described in Section 2.0.3, has been selected. Fiala model, see eq. (2.20), has been used for modeling tyre lateral force, given its simplicity and dependency only on physical parameters, while wheel rotational dynamics have been considered fast enough to be neglected. Therefore, the following vehicle parameters have to be estimated:

- mass m;
- center of gravity position, i.e., a and b;
- tyre-ground friction coefficient μ;
- vehicle yaw moment of inertia J_z;
- tyres cornering stiffnesses C_α^f, C_α^r;

3.5.1 Mass and longitudinal position of the center of gravity estimation

Car mass and the position of the center of gravity had been estimated with a digital balance. In particular, longitudinal position of the center of gravity has been estimated by measuring the longitudinal weight distribution, i.e., by measuring the mass acting on the front (m_f) and rear (m_r) axle and by

Table 3.5: *Scaled car: mass and longitudinal position of the center of gravity*

m [Kg]	1.90
a [m]	0.1368
b [m]	0.1232

exploiting the following formulae, in which l is car wheelbase, which is given by $a + b$:

$$\frac{m_f}{m} = \frac{b}{l}$$
$$\frac{m_r}{m} = \frac{a}{l}.$$

Table 3.5 lists the value of these parameters. It follows that the longitudinal weight distribution of the car is $47 - 53\%$. Moreover, it can be observed that the mass of the scaled car is three orders of magnitude smaller than the typical mass of a real car, in accordance with the fact that the mass scales with the volume.

3.5.2 Tyre-ground friction coefficient estimation

Static friction coefficient μ has been estimated by measuring vehicle lateral accelearation a_y at the center of gravity during a steady-state turning manoeuvre which brings the car up to its limits of handling. Infact, maximum lateral acceleration which can be experienced by the car can be approximated as follows [27]:

$$a_y^{max} = \mu g,$$

in which g is gravity acceleration. It can be observed that this identification technique does not give the opportunity to estimate also tyre dynamic friction coefficient. However, Fiala lateral force model, which has been used throughout this work, does not distinguish between static and kinetic friction, since it comes from brush model. As a consequence, Fiala model does not reproduce the negative slope portion of the $\alpha - F_y$ curve, in contrast to, for example, Pacejka Magic Formula. Therefore, the friction coefficient of interest for Fiala model is the one which yields the maximum value of tyre force, i.e., static friction μ.
Static friction coefficient has been estimated on two different surfaces, namely carpet and wood flooring, and with two different set of tyres, i.e., drifting tyres (hard compound) and rubber tyres (soft compound). Table 3.6 sums up the estimated friction coefficient for the two surfaces and the two sets

Table 3.6: *Estimated friction coefficient for the two different test surfaces*

Surface	Drifting tyres	Rubber tyres
Carpet	0.385	0.650
Wood floring	0.255	0.380

of tyres. In particular, drifting tyre set and carpet or wood flooring surface yield a friction coefficient which is close to that of a real car traveling on a road covered with gravel or snow, respectively. Rubber tyre set and carpet or wood flooring surface gives a friction coefficient which, in both these cases, resembles that of a real vehicle traveling on a wet, asphalt road. Fig. 3.13 depicts, as an illustrative example, the result of the identification experiment performed over carpet flooring with drifting tyres. Lateral acceleration fluctuations are due to measurement noise and mechanical vibration of the car while traveling.

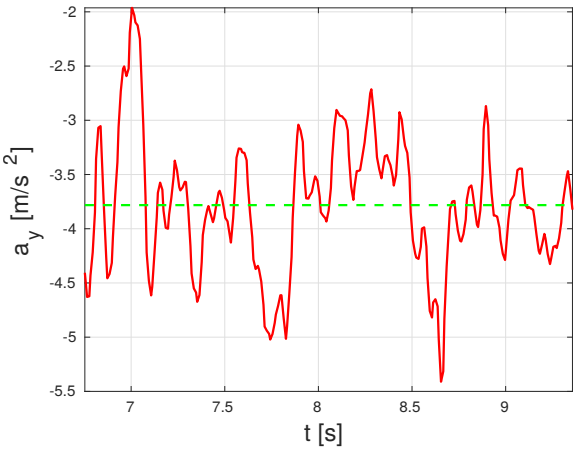

Figure 3.13: *Tyre ground friction coefficient estimation on carpet flooring and drifting tyres: red, solid line represents AHRS measurement while green, dashed line stands for the mean acceleration, which is equal to* $-3.78\,ms^{-2}$

3.5.3 Vehicle Yaw moment of inertia, tyre cornering stiffness estimation

Yaw moment of inertia and front and rear tyre cornering stiffness have been estimated using the methodology described in [22]. Basically, errors between measured and simulated yaw rate, lateral velocity and lateral acceleration have been minimized. It is important to be aware that, from a con-

ceptual point of view, this parameter estimation procedure does not yield the real, physical value of the unknown parameters, but their values which, substituted inside the adopted dynamic model, yield the best simulation results, which, however, is what was needed: a dynamic model of the system which correctly reproduces its dynamics, being thus suitable for designing dynamic controllers.
Formally, the nonlinear optimization problem which has been solved is the following:

$$\underset{X}{\text{minimize}} \qquad \sum_{j=1}^{N_y} \sum_{i=1}^{N} \left[\frac{w_j}{s_j} \left(\tilde{y}_j(i) - \hat{y}_j(i) \right) \right]^2 \tag{3.7}$$

$$\text{subject to} \qquad \dot{\xi} = f_\xi \left(\xi, u, X \right) \tag{3.8}$$

$$\xi(0) = \xi_0 \tag{3.9}$$

$$\hat{y} = f_y \left(\xi, u, X \right) \tag{3.10}$$

$$L \leq X \leq U. \tag{3.11}$$

In particular:

- N is the number of samples collected, while N_y is the number of output variables being compared;
- X is the vector of unknown parameters, which have to be determined, namely $X = \left[C_\alpha^f, C_\alpha^r, J_z \right]$;
- $\tilde{y}$ is a measured output, while $\hat{y}$ is a simulated output;
- w_j and s_j are j-th output weight and normalization coefficient, respectively;
- ξ is system state vector, which is composed of the following state variables: $\xi = [V_y, r]$;
- f_ξ are vehicle lateral dynamics state equations. Nonlinear single-track model presented in Section 2.0.3 has been adopted, where Fiala model given by eq (2.20) has been used to model tyre lateral force;
- u is the vector of control inputs: $u = [\delta, V_x]$. In particular, V_x has been considered as an input signal as we carried out only the identification of the lateral dynamics of the vehicle, and therefore the longitudinal state equation has not been considered;

- L and U are X lower and upper bound, respectively. More extensively:

$$\begin{bmatrix} C_\alpha^{f,min} \\ C_\alpha^{r,min} \\ J_z^{min} \end{bmatrix} \leq \begin{bmatrix} C_\alpha^{f} \\ C_\alpha^{r} \\ J_z \end{bmatrix} \leq \begin{bmatrix} C_\alpha^{f,max} \\ C_\alpha^{r,max} \\ J_z^{max} \end{bmatrix}.$$

In particular, the lower bound on the value of the yaw moment of inertia has been taken as the yaw moment of inertia of the car without the hardware components. This value has been estimated by hanging the car to the tip of an industrial manipulator, as shown in Fig. 3.14, equipped with a torque sensor, and measuring the reaction torque to a trapezoidal angular speed profile applied to the vehicle yaw axis, which is shown in Fig. 3.15. Fig. 3.16 shows the comparison between simulated and measured car yaw angular speed. The upper bound has been taken as the yaw moment of inertia obtained by concentrating the whole mass of the vehicle at the front, m_f, and rear, m_r, axles: $J_z^{max} = m_f a^2 + m_r b^2$. On the other hand, cornering stiffness minimum and maximum values have been selected based on experience and considering their order of magnitude for a real car. Therefore:

$$\begin{bmatrix} 0 \\ 0 \\ 0.015 \end{bmatrix} \leq \begin{bmatrix} C_\alpha^{f}\,[\mathrm{N\,rad^{-1}}] \\ C_\alpha^{r}\,[\mathrm{N\,rad^{-1}}] \\ J_z\,[\mathrm{Kg\,m^2}] \end{bmatrix} \leq \begin{bmatrix} 1000 \\ 1000 \\ 0.032 \end{bmatrix}.$$

To solve the optimization problem defined by eq. (3.7), single-track nonlinear dynamic model has been discretized with forward Euler method and a sampling time T_s of $0.01\ s$ (which allowed to obtain a stable discrete time system):

$$\xi(k+1) = \xi(k) + T_s\, f_\xi\left(\xi(k), u(k), X\right).$$

To assess the quality of the identified model, simulation outputs have been compared against measured outputs in a validation experiment, i.e., a dataset different from identification dataset. Normalized Mean Prediction Error (NMPE, [22]), has been used to assess the quality of the identified model. To perform the estimation, the scaled car has been driven along a mixed trajectory, which includes turns characterized by different turning radii and taken at low and high speed, in order to excite all the involved dynamics. Fig. 3.17 shows an example of such a trajectory. Finally, since this parameter estimation method is prone to fall into local minima, optimization problem (3.7) has been solved starting from 125 combination of initial conditions, obtained by picking 5 equally spaced points from each unknown parameter's range. Then, the solution which gives the minimum of the cost

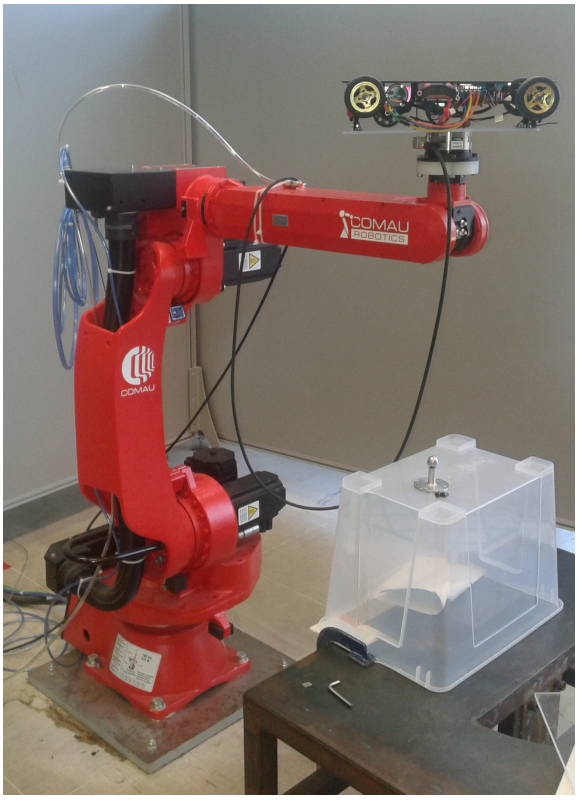

Figure 3.14: *Car yaw moment of inertia lower bound estimation experiment*

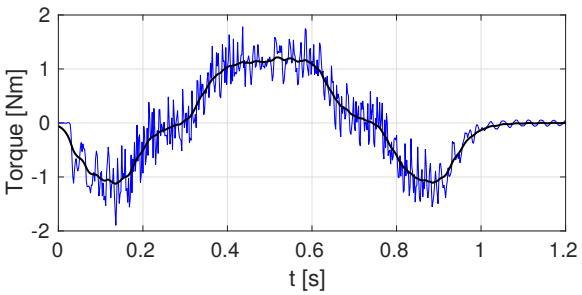

Figure 3.15: *Car yaw moment of inertia lower bound estimation: measured and filtered torque as blue and black line, respectively*

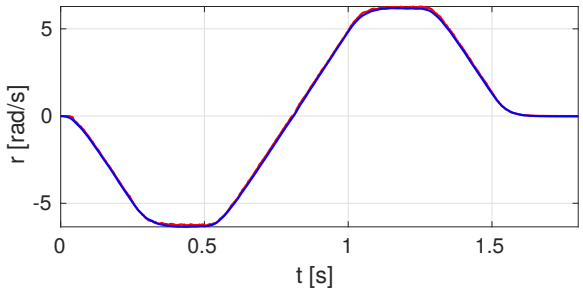

Figure 3.16: *Car yaw moment of inertia lower bound estimation validation experiment: comparison between simulated (as a blue line) and measured (as a red line) car yaw angular speed*

function has been selected. Tables 3.7 and 3.8 sums up the results obtained on carpet and wood flooring surface, respectively. Fig. 3.18, 3.19, 3.20

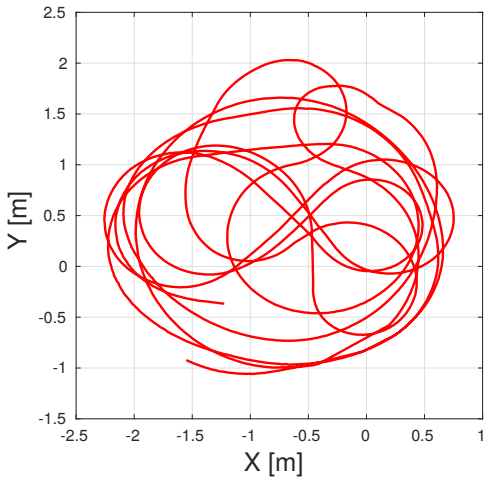

Figure 3.17: *Single-track parametere estimation: example of travelled trajectory*

and 3.21 illustrates the results of the validation experiments on the two different surfaces and with different tyre sets. These figures, along with the low value of NMPE in Tables 3.7 and 3.8, suggest that nonlinear single-track model is able to correctly reproduce vehicle lateral dynamics, up to the limits of vehicle handling.

Table 3.7: *Scaled car parameters for carpet surface*

Parameter	Drifting tyres	Rubber tyres
J_z $\left[\mathrm{Kg\,m^2}\right]$	0.029	0.0263
C_α^f $\left[\mathrm{N\,rad^{-1}}\right]$	50.13	42.58
C_α^r $\left[\mathrm{N\,rad^{-1}}\right]$	122.05	214.21
$NMPE$	0.255	0.196

Table 3.8: *Scaled car parameters for wood flooring surface*

Parameter	Drifting tyres	Rubber tyres
J_z $\left[\mathrm{Kg\,m^2}\right]$	0.032	0.032
C_α^f $\left[\mathrm{N\,rad^{-1}}\right]$	244.51	48.77
C_α^r $\left[\mathrm{N\,rad^{-1}}\right]$	224.41	88.95
$NMPE$	0.369	0.232

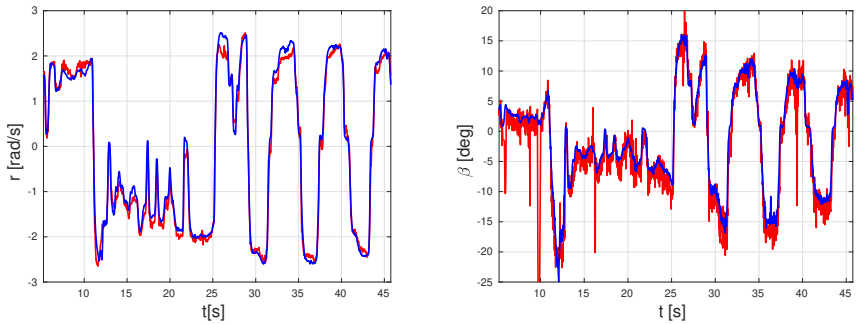

(a) *Yaw rate* **(b)** *Sideslip angle*

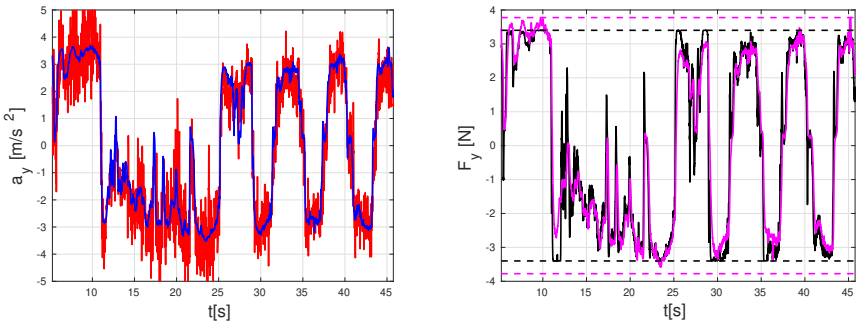

(c) *Lateral acceleration* **(d)** *Tyre lateral force*

Figure 3.18: *Single-track parameter estimation on carpet surface, drifting tyres: comparison between experimental (as red line) and simulated (as blue line) results on the validation dataset. In Fig. 3.18d black line indicates front tyre lateral force while magenta line stands for rear tyre lateral force*

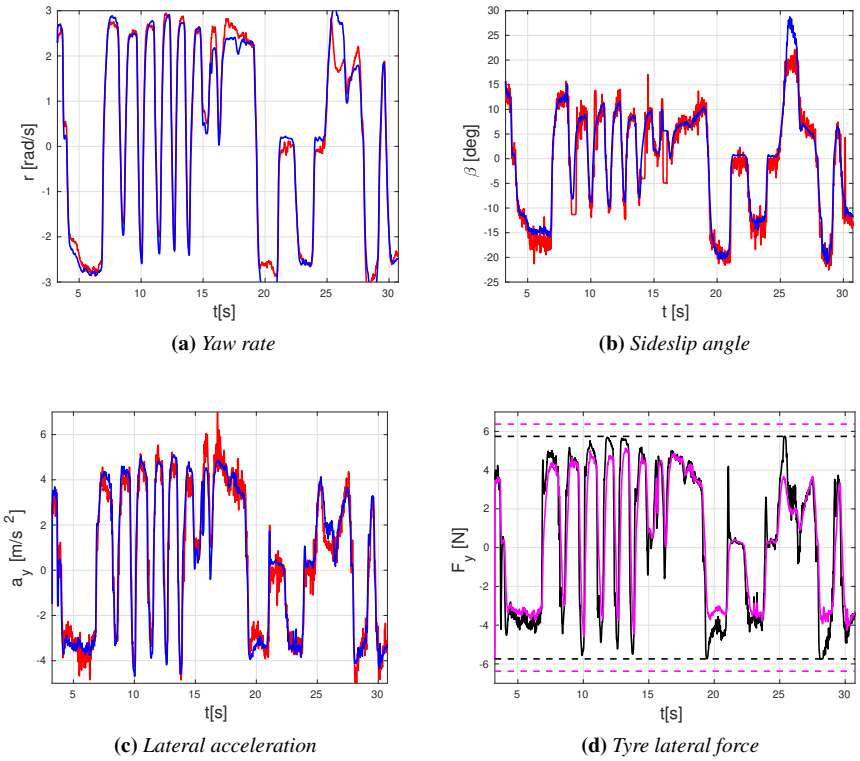

(a) *Yaw rate*

(b) *Sideslip angle*

(c) *Lateral acceleration*

(d) *Tyre lateral force*

Figure 3.19: *Single-track parameter estimation on carpet surface, rubber tyres: comparison between experimental and simulated results on the validation dataset. In Fig. 3.19d black line indicates front tyre lateral force while magenta line stands for rear tyre lateral force*

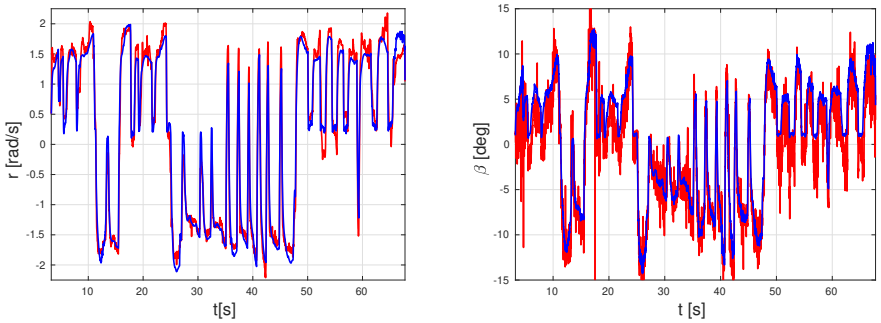

(a) *Yaw rate*

(b) *Sideslip angle*

(c) *Lateral acceleration*

(d) *Tyre lateral force*

Figure 3.20: *Single-track parameter estimation on wood flooring surface, drifting tyres: comparison between experimental and simulated results on the validation dataset. In Fig. 3.20d black line indicates front tyre lateral force while magenta line stands for rear tyre lateral force*

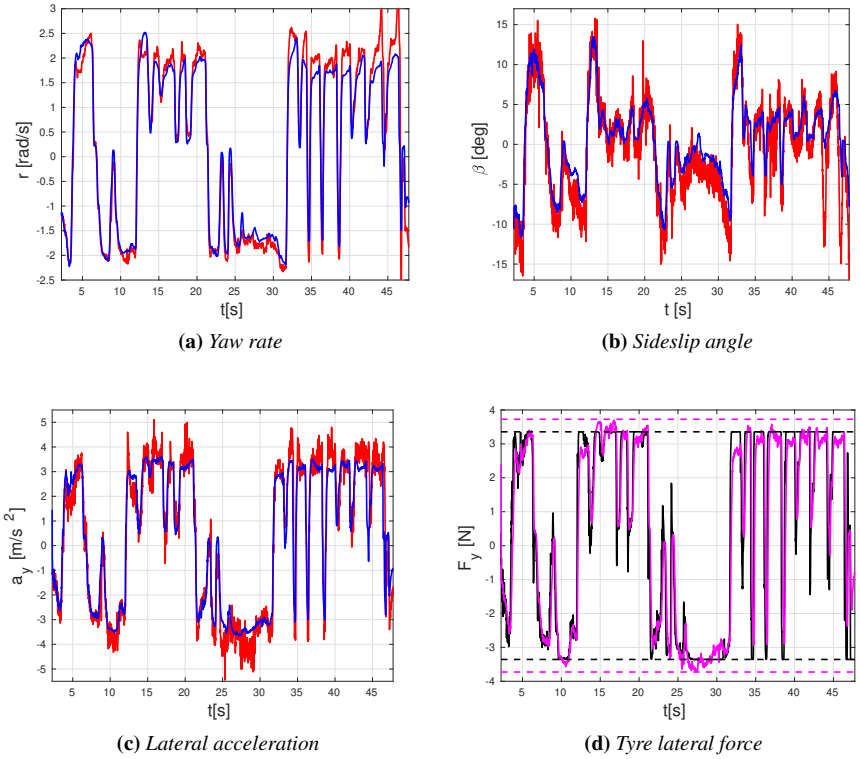

(a) *Yaw rate*

(b) *Sideslip angle*

(c) *Lateral acceleration*

(d) *Tyre lateral force*

Figure 3.21: *Single-track parameter estimation on wood flooring surface, rubber tyres: comparison between experimental and simulated results on the validation dataset. In Fig. 3.21d black line indicates front tyre lateral force while magenta line stands for rear tyre lateral force*

Table 3.9: *Scaled car drag force model coefficients*

F_d^0 [N]	3.25
F_d^1 $\left[\mathrm{Nm^{-1}s}\right]$	0
F_d^2 $\left[\mathrm{Nm^{-2}s^2}\right]$	0

Drag force estimation

When controlling motor current, and hence torque, it is necessary to estimate the drag force which is acting on the car, due to mechanical friction, tyre rolling friction and aerodynamic drag force. The same technique described in Section 3.5.3 has been used, considering only the dynamic equation relative to longitudinal motion, to determine the parameters of the following drag model:

$$F_d = F_d^0 + F_d^1 V_x + F_d^2 V_x^2,$$

where F_d is the drag force and F_d^i are the coefficients of the $i-th$ power of V_x. Table 3.9 lists the values of those parameters.
According to the results of the identification procedure, a constant friction model has been adopted.

3.6 Dynamic similitude

As already mentioned, [11] presented an analysis, based on the Pi theorem, which ensures that a real car and a scaled one are in dynamic similitude, when the following non-dimensional coefficients take the same value:

$$\begin{aligned}
\Pi_1 &= \frac{a}{a+b} \\
\Pi_2 &= \frac{b}{a+b} \\
\Pi_3 &= \frac{C_\alpha^f (a+b)}{m V_x^2} \\
\Pi_4 &= \frac{C_\alpha^r (a+b)}{m V_x^2} \\
\Pi_5 &= \frac{J_z}{m\,(a+b)^2},
\end{aligned} \tag{3.12}$$

where Π_1 and Π_2 refers to longitudinal weight distribution.
In general, once vehicle physical parameters are known and Π_1, Π_2 and Π_5 coefficients are identical for both vehicles, longitudinal velocity V_x of

Table 3.10: *Scaled car dynamic similitude*

Parameter	Scaled car, rubber tyre	Sedan
μ	0.38 (wood flooring)	1 (asphalt)
V_x $\left[\mathrm{ms}^{-1}\right]$	7.5	30
Π_1	0.53	0.45
Π_2	0.47	0.55
Π_3	0.12	0.16
Π_4	0.21	0.15
Π_5	0.25	0.23

the compared vehicles is selected in order to verify the dynamic similitude, i.e., to match Π_3 and Π_4. In other words, using the Buckingham-Pi theorem one can show that the solutions of the nonlinear differential equations modelling a real vehicle are identical, after accounting for the dimensional scaling of each parameter in the equations, to the solutions of the differential equations describing the scaled model.
Table 3.10 lists non-dimensional coefficients (3.12) for the scaled car, running with rubber tyre set on wood flooring surface at a speed of $7.5\,ms^{-1}$, and for the Sedan vehicle, which was presented in 2.1, running on asphalt at a speed of $30\,ms^{-1}$. Values of non-dimensional coefficients are of the same order of magnitude. Moreover, they are almost identical. An even closer match of Π_1 and Π_2 coefficients could be achieved by modifying scaled car weight distribution, which differs from Sedan weight distribution mainly due to the fact that scaled car motor is located behind vehicle COG, while Sedan motor is mounted in front of car COG, closer to vehicle front axle. Therefore, Pi theorem, along with the values of non-dimensional coefficients (3.12) reported in Table 3.10, ensure that it is possible and meaningful to use the scaled car to test vehicle dynamic controllers, as the dynamics of the scaled car matches that of a real car.

CHAPTER 4

Autonomous drifting with LQR approach

Drifting is the art of driving a car sideways, up to its limits of handling. It is used by rally drivers to go as fast as possible on slippery surfaces, as shown in [59–61], it expands vehicle mobility capabilities at low speeds [62], and sometimes it is the only viable option to avoid an obstacle in an emergency condition [32]. Moreover, drifting is an exciting experience, as demonstrated by the recent interest of automotive companies in the development of drifting-assistants.
From the control perspective, sustained drifting can be formulated as the problem of stabilizing an unstable equilibrium point [20], which is the result of a bifurcation [19], and whose distinctive traits are a large sideslip angle, counter-steering, and the use of longitudinal force developed by tyres as an additional control input for the vehicle lateral dynamics. The complexity of this problem comes from the multiple number of inputs and outputs, the saturation constraints on the control inputs, and the nonlinearities of the underlying dynamics.

LQ control strategy has already been used to stabilize drifting in several works. In [63] steering is used to manage drift, and throttle action is exploited to control vehicle longitudinal speed, while an expert human driver takes advantage of a coordinated longitudinal and lateral control [62].

In [31] a scaled car has been used to test a drifting stabilizing LQR which relies only on on-board sensors for state estimation, and stabilizes longitudinal and lateral velocities, and yaw rate. Nevertheless, front tyre lateral force rather than steering angle has been considered as control input, along with the longitudinal force developed by rear tyres. Moreover, only a few experimental results were presented and a robustness analysis has not been performed. Finally, in [62] and [4], a LQR synthesized on a linearised full-track vehicle model, which includes the model of the rear limited-slip differential, has been tested but only in simulation. Wheel rotational dynamics has been also considered, and a low-level longitudinal slip controller has been designed.
Besides the LQ control strategy, other control approaches have been adopted to solve the drifting stabilization problem. In [35], which represents an evolution of [63], yaw rate is assumed as an additional fictitious control input to the sideslip angle dynamics, and a coordinated lateral and longitudinal control law is developed. Longitudinal speed is not tracked, but a numerical test showing the asymptotic stability of the longitudinal dynamics is provided. This approach was further extended in [29], to track a circular path while drifting at constant speed. In [64] the tracking of a reference velocity vector absolute angle and the stabilization of the sideslip angle are decoupled and assigned to steering and throttle, respectively. The proposed controller, which has been derived exploiting feedback linearisation and sliding mode theory, has been successfully tested on a production car equipped with a combustion engine. Nevertheless, the decoupling limits the basin of attraction of the closed-loop system, and does not resemble what an expert human driver does [29]. Moreover, the controller has been derived upon the linear approximation of the front lateral force-slip angle relation, an assumption which is not verified in drifting [63]. The same assumption has also been used in [47], to obtain a drifting stabilizing controller which takes advantage of control inputs not available to a human driver, namely the driving forces of the four independently driven wheels. Finally, a completely different approach, based on learning from demonstration, has been adopted in [46] to let a scaled car autonomously execute drifting maneuvers even in the presence of large variations of the friction coefficient.

This work aims at providing a detailed analysis based on an extensive experimental campaign, which offers a more realistic environment compared to any accurate multi-body simulation, allowing to assess performance, robustness, and shortcomings of a linear-quadratic-regulator (LQR) applied to the problem of sustained drifting stabilization and circular path tracking,

using the same controls available to a human driver, namely steering angle and longitudinal force developed by tyres. Firstly, only the stabilization of an unstable drifting equilibrium point has been addressed. Then, for the first time to the best of author's knowledge, path tracking capability of a circular path has been added to the aforementioned controller, yielding a drifting circular path tracking controller. The proposed control approach is developed for a rear-wheel-driven (RWD) vehicle, although it could be easily extended to an all-wheel-driven (AWD) car. Part of this work has been published in [7].

4.1 Autonomous drifting stabilization

In this Section, the LQ control strategy is applied to the problem of drifting stabilization of a RWD vehicle. The controller uses the same controls available to a human driver, namely front tyre steering and rear tyre longitudinal force, to stabilize longitudinal and lateral velocities and yaw rate, and it is designed on a linearised single-track model of the vehicle, which, differently from [4, 62], does not include a model of the rear differential and of wheel rotational dynamics. The performance and robustness of this control approach are assessed with an extensive experimental campaign performed on the scaled car presented in Chapter 3.

4.1.1 System model

Drifting, due to a large force involved, calls for the adoption of a dynamic model of vehicle motion [27]; therefore, the single-track model [53] (Fig. 2.3, Section 2.0.3) has been used, as in [35, 63], under the hypothesis of negligible roll and pitch motion, and lateral load transfer. The latter always holding at low speed and on low-grip terrains, as it is usually the case of drifting.
The state variables are the longitudinal and lateral velocities, V_x and V_y, along with the yaw rate r, while the control inputs are the front wheel steering angle δ and the longitudinal force developed by the rear tyres F_x^r, as the

considered vehicle is RWD. The state equations are the following:

$$\begin{aligned} \dot{V}_x &= \frac{F_x^r - F_y^f sin(\delta)}{m} + rV_y \\ \dot{V}_y &= \frac{F_y^f cos(\delta) + F_y^r}{m} - rV_x \\ \dot{r} &= \frac{aF_y^f cos(\delta) - bF_y^r}{J_z}. \end{aligned} \tag{4.1}$$

Front and rear lateral tyre forces, F_y^f and F_y^r, are modelled with the modified version of the Fiala model introduced in [35] to account for the coupling between the longitudinal and lateral tyre force through the so-called derating factor ξ, as follows:

$$F_y = \begin{cases} -C_\alpha z + \eta C_\alpha |z| z - \frac{1}{3}\eta^2 C_\alpha z^3, & |z| < \tan(\alpha_{sl}) \\ -\xi \mu F_z sgn(\alpha), & |z| \geq \tan(\alpha_{sl}) \end{cases}$$

where

$$\alpha_{sl} = \tan^{-1}\left(\frac{1}{\eta}\right) \qquad z = \tan(\alpha) \qquad \eta = \frac{C_\alpha}{3\xi\mu F_z}$$

in which α is the sideslip angle of the front and rear wheels, given by

$$\begin{aligned} \alpha^f &= \tan^{-1}\left(\frac{V_y + ar}{V_x}\right) - \delta \\ \alpha^r &= \tan^{-1}\left(\frac{V_y - br}{V_x}\right), \end{aligned}$$

F_z is the normal load acting on the axle according to

$$F_z^f = mg\frac{b}{a+b} \qquad F_z^r = mg\frac{a}{a+b},$$

in which C_α is the cornering stiffness, μ is the friction coefficient, a and b are the distance of vehicle COG from front and rear axle, respectively. Finally, ξ is the so-called derating factor, which is defined as

$$\xi = \frac{\sqrt{(\mu F_z)^2 - F_x^2}}{\mu F_z}.$$

It must be noticed that the lateral velocity has been assumed as the state variable for the vehicle lateral dynamics instead of the vehicle sideslip angle

$\beta = \tan^{-1}(V_y/V_x)$, in order to avoid the coupling between longitudinal and lateral dynamics that is intrinsic into the analytical expression of the sideslip angle. In addition, rear differential and wheel rotational dynamics have not been considered, as it has been assumed that their dynamics are fast enough to be neglected. Moreover, assuming F_x^r is the control variable, one leaves room, if needed, for the adoption of a lower-level longitudinal slip controller, though the experimental tests performed on the scaled car revealed that such a traction controller is not necessary.

4.1.2 LQR control approach

Nonlinear system (4.1) has been linearised around a drifting equilibrium point, yielding a linear time invariant controllable system. Defining

$$\Delta\mathbf{x} = [\Delta V_x, \Delta V_y, \Delta r]^T \qquad \Delta\mathbf{u} = [\Delta\delta, \Delta F_x^r]^T$$

as the difference between state and control input variables and their equilibrium value, a LQR state feedback control law $\Delta\mathbf{u} = -K\Delta\mathbf{x}$ has been adopted, where matrix K has been chosen in order to minimize the cost function $J = \int_0^\infty \left(\mathbf{x}^T Q\,\mathbf{x} + \mathbf{u}^T R\,\mathbf{u}\right) dt$. To ease the controller tuning process, the state and control input weight matrices Q and R have been selected as follows:

$$Q = diag\left(\frac{w_{\Delta x_i}}{\Delta x_{i,max}^2}\right) \quad R = diag\left(\frac{w_{\Delta u_j}}{\Delta u_{j,max}^2}\right) \tag{4.2}$$

where $w_{\Delta x_i}$, $w_{\Delta u_j}$ are weights which penalize the i-th state variable and the j-th control input, respectively, and $\Delta x_{i,max}$, $\Delta u_{j,max}$ are normalizing terms, introduced to take into account state and control input saturation constraints, respectively. Selecting strictly positive weights for Q and R matrices, given that the linearised system is controllable, the closed-loop system is guaranteed to be asymptotically stable [44].

4.1.3 Drifting equilibrium point computation

To compute cornering equilibria of the single-track nonlinear model (4.1), five unknowns have to be determined: $\bar{V}_x, \bar{V}_y, \bar{r}, \bar{\delta}, \bar{F}_x^r$. Since there are only three state equations, the values of the longitudinal speed $\bar{V}_x$ and of the steering angle have been arbitrarily selected. Fig. 4.1 illustrates the computed cornering equilibria for a longitudinal speed of $1\,m/s$, carpet surface, drifting tyre set, and scaled car newest configuration, shown in Fig. 3.3.
In particular, cornering equilibria points fall inside three classes:

Table 4.1: *Scaled car selected drifting equilibrium point, on carpet surface and drifting tyre set*

$\bar{V}_x$	1	$\mathrm{m\,s^{-1}}$
$\bar{V}_y$	-0.74	$\mathrm{m\,s^{-1}}$
$\bar{\beta}$	-37	deg
$\bar{r}$	2.32	$\mathrm{rad\,s^{-1}}$
$\bar{\delta}$	-20	deg
$\bar{F}_x^r$	2.53	N

- traditional cornering equilibria, which are not characterized by understeering or countersteering;
- understeering cornering equilibria;
- drifting cornering equilibria, whose distinctive traits are large sideslip angle, counter-steering and saturation of rear tyre friction force, as highlighted by the friction circle portrayed in Fig. 4.1f. In particular, counter-steer can be inferred by the steering angle sign, which is equal to the sign of the sideslip angle and opposite to the sign of the yaw rate.

Stars in Fig. 4.1 highlight the selected drifting equilibrium point, while Table 4.1 lists the values assumed by state and input variables at that equilibrium point. Moreover, linearized system state and control input matrices at the selected equilibrium point are equal to:

$$A = \begin{bmatrix} -1.4 & -0.99 & -1.2 \\ -6.3 & -9.1 & -2.2 \\ -35.5 & -81.1 & -11.1 \end{bmatrix} \quad B = \begin{bmatrix} 2.8 & 0.5 \\ 11.2 & -0.6 \\ 100.2 & 4.7 \end{bmatrix}$$

The fact that both the state and the control input matrices are full corroborate the idea that a coordinated lateral and longitudinal control strategy is needed, since the dynamics are not decoupled. Moreover, the computation of the eigenvalues of the open loop system confirms that the selected drifting equilibrium point is unstable [20]. Finally, linearized system is controllable.

4.1.4 Experimental results

This section presents the experimental results obtained by testing the proposed LQR drifting stabilization controller on the experimental platform described in detail in Chapter 3. To perform the experiments, the controller has been coded into a ROS node which runs at $100\,\mathrm{Hz}$. Then, it has been

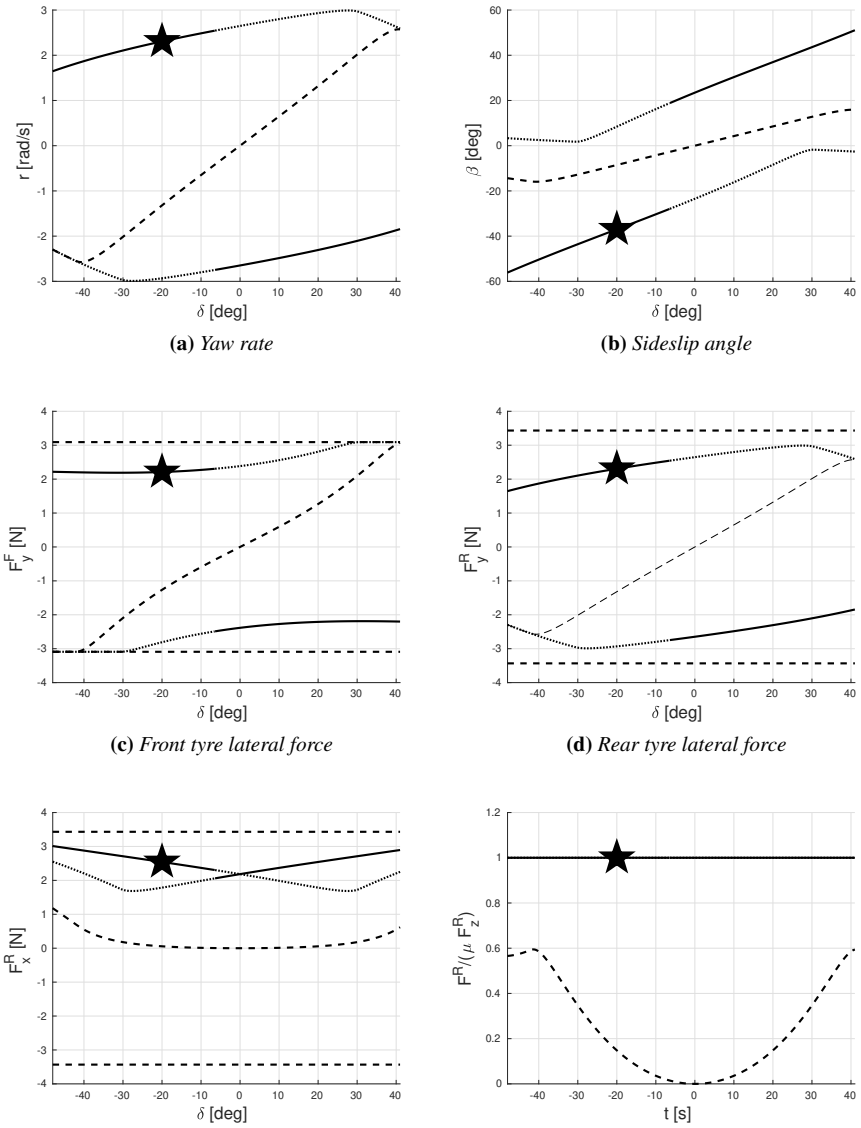

(a) *Yaw rate*

(b) *Sideslip angle*

(c) *Front tyre lateral force*

(d) *Rear tyre lateral force*

(e) *Rear tyre longitudinal force*

(f) *Rear tyre friction circle*

Figure 4.1: *Scaled car cornering equilibria on carpet surface and drifting tyre set: normal cornering equilibria as dashed line, understeering equilibria as dotted line, drifting equilibria as solid line; star denotes selected drifting equilibrium point*

Table 4.2: *LQR drifting stabilization controller parameters, for scaled car old configuration, carpet surface and drifting tyre set*

$\Delta V_{x,max}$	0.5	$\mathrm{m\,s^{-1}}$	$w_{\Delta V_x}$	1
$\Delta V_{y,max}$	0.45	$\mathrm{m\,s^{-1}}$	$w_{\Delta V_y}$	5
Δr_{max}	0.5	$\mathrm{rad\,s^{-1}}$	$w_{\Delta r}$	0.5
$\Delta \delta_{max}$	0.45	rad	$w_{\Delta \delta}$	1
$\Delta F^r_{x,max}$	1.07	N	$w_{\Delta F^r_x}$	0.75

tuned by first testing it in simulation on system (4.1), and then on the real experimental platform. The car is initially manually driven in circle and then the controller is activated by manually pressing a button on the radio. Thanks to factorization (4.2), the tuning process has been very intuitive: for instance, if the car accelerated too much, a higher weight on the longitudinal velocity error was selected. On the other side, the weights on the control input allowed to shift the control effort towards the steering or the rear longitudinal force.

Tests performed using the old scaled car configuration

Initially, LQR drifting stabilization controller has been tested on the old scaled car configuration, illustrated in Fig. 3.1, which mounted the slower servo, whose dynamics is described by first-order model (3.6), and characterized by a delay equal to $0.09\,s$. Table 4.2 lists the selected controller parameters, which give the best trade-off between performance and robustness.

The designed LQR is able to stabilize the vehicle around the selected drifting equilibrium point, as illustrated in Fig. 4.2, which show a portion of an experiment performed over the carpet surface with drifting tyre set, proving that the modeling of wheel and differential dynamics is not necessary. Fluctuations which characterize yaw rate profile in Fig. 4.2c are, unsurprisingly, due to the large delay of the steering servo. This hypothesis has been verified by the lack of yaw rate fluctuations when the same LQR controller has been tested against non-linear single-track model given by eq. (4.1), without the presence of steering actuator delay.

In addition, the tuning is made complex by the dynamics of the process: a too large gain on the yaw rate error produces a chattering like behaviour, with large oscillations of the yaw rate; while a too large gain on the lateral velocity error yields yaw rate oscillations as well, due to the fact that the lateral velocity dynamics is slower than the yaw rate dynamics (Fig. 4.3), as

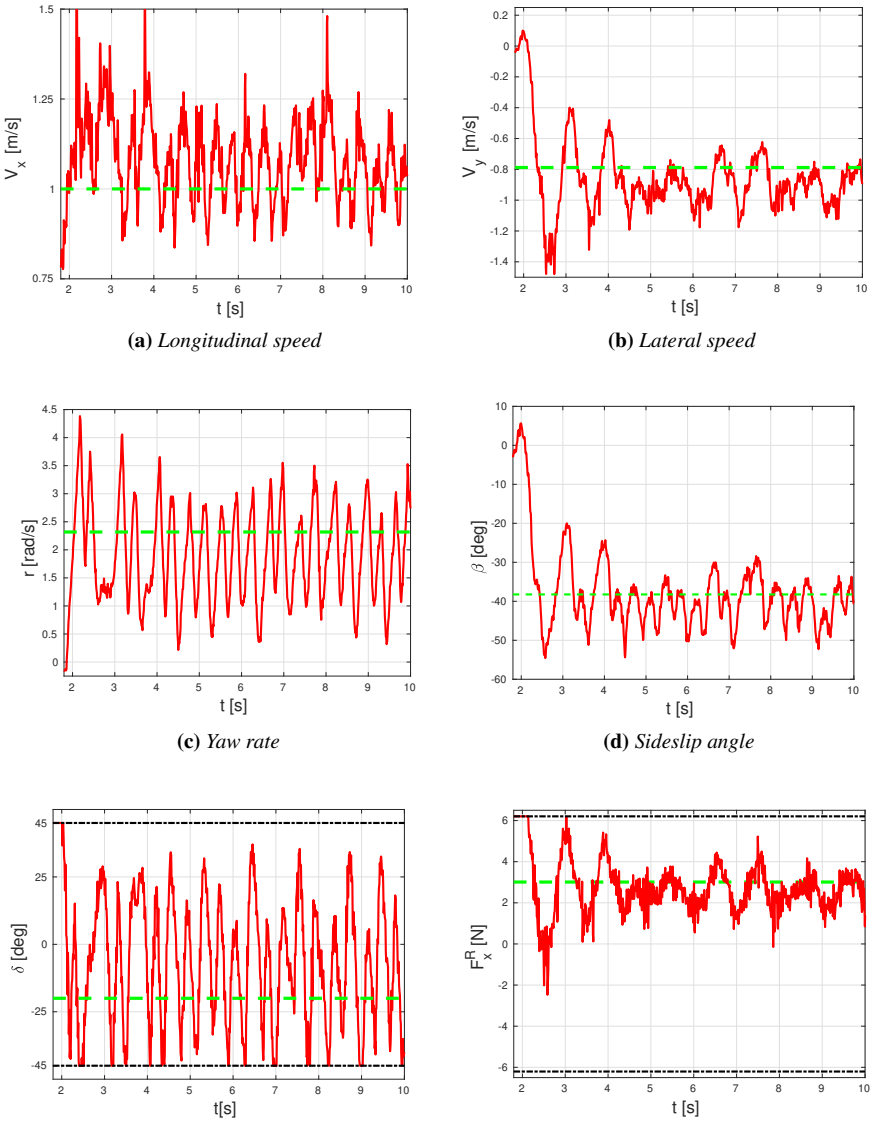

(a) *Longitudinal speed*

(b) *Lateral speed*

(c) *Yaw rate*

(d) *Sideslip angle*

(e) *Steering angle*

(f) *Rear tyre longitudinal force*

Figure 4.2: *Drifting stabilization on carpet surface, drifting tyre set and scaled car old configuration. Experimental data as red solid line, equilibrium value as green dashed line and actuator saturation as black, dash-dotted line*

already observed in [63]. On the other hand, the adopted control approach

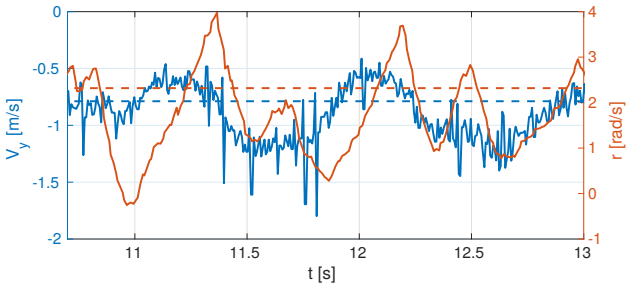

Figure 4.3: *Drifting stabilization on carpet surface, drifting tyre set and scaled car old configuration: comparison between lateral velocity and yaw rate profiles (equilibrium values as dashed lines).*

proved to be very robust. A slight slope of the ground caused a shift in the followed circular trajectory, as it can be seen in Fig. 4.4, but did not prevent the controller to successfully drift for a long time without loosing car's control. Moreover, the LQR tuned on the carpet surface can successfully

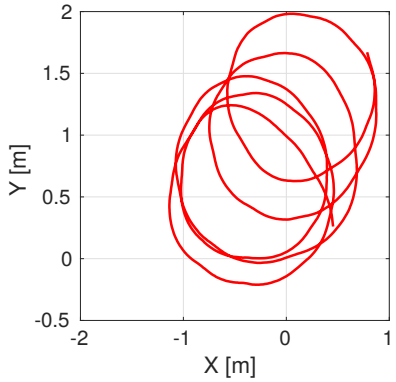

Figure 4.4: *Drifting stabilization on carpet surface, drifting tyre set and scaled car old configuration: the path followed by the car during the experiment.*

handle car's control even in presence of a 34% reduction of the friction coefficient, obtained running the car on the more slippery wood flooring surface (Fig. 4.5, Table 3.6). This shows that a low-level longitudinal slip tracking controller, as developed in [62], is not necessary: only a traction controller, which prevents wheels from spinning in the unstable region of the longitudinal slip - longitudinal force curve [27] would be beneficial.
Furthermore, Figs. 4.2 and 4.5 show that the controller is able to bring the

Table 4.3: *LQR drifting stabilization controller parameters, for scaled car newest configuration, carpet surface and drifting tyre set*

$\Delta V_{x,max}$	0.5	$\mathrm{m\,s^{-1}}$	$w_{\Delta V_x}$	1
$\Delta V_{y,max}$	0.45	$\mathrm{m\,s^{-1}}$	$w_{\Delta V_y}$	5
Δr_{max}	0.5	$\mathrm{rad\,s^{-1}}$	$w_{\Delta r}$	0.001
$\Delta\delta_{max}$	0.45	rad	$w_{\Delta\delta}$	1
$\Delta F^r_{x,max}$	1.07	N	$w_{\Delta F^r_x}$	0.75

car to the desired equilibrium point when the car is starting both from standing still and large longitudinal velocity, a fact which highlights the extent of the basin of attraction.
Finally, a video[1] shows some experiments which highlight the robustness of the LQR, and the difficulties faced when manually driving the car in the presence of large sideslip angles.

Tests performed using the newest scaled car configuration

LQR drifting stabilization control has also been tested on the newest scaled car configuration, depicted in Figs. 3.2 and 3.3. In particular, tests have been performed to verify that a faster steering servo (see eq. (3.5) and Table 3.3) reduces yaw rate oscillations, thus yielding better closed-loop performance.
Table 4.3 reports controller tuning parameters, which, compared to tuning parameters used for the older car configuration (Table 4.2), differ only for yaw rate error weight $w_{\Delta r}$. This confirms the ease with which controller parameters could be selected to achieve good closed-loop performances. Fig. 4.6 illustrates the results achieved by testing the controller on carpet surface, with drifting tyre set. Lower yaw rate oscillations can be observed, thanks to the faster steering servo. Longitudinal velocity equilibrium value is not perfectly tracked, with the car traveling at a speed slightly above the reference. However, this tuning yielded the larger basin of attraction and the best robustness. In particular, robustness against external disturbance forces and parameter uncertainties have been assessed[2], as illustrated in Appendix **??**.

[1] The video is available here: `https://goo.gl/38H2Ff`.
[2] A video of these experiments is available at `https://youtu.be/Q7k9pDSBMFI`

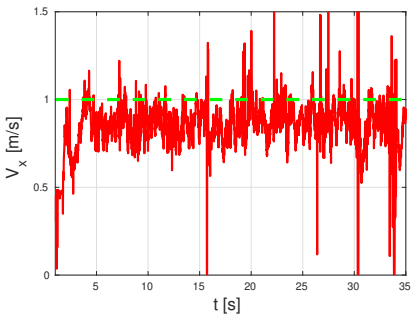

(a) *Longitudinal speed*

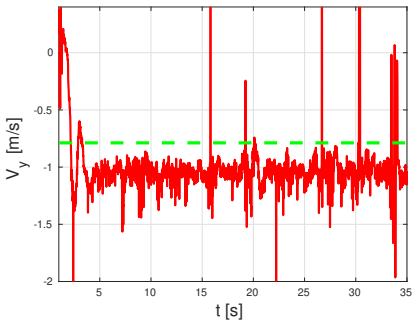

(b) *Lateral speed*

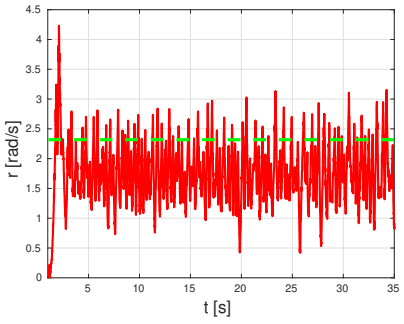

(c) *Yaw rate*

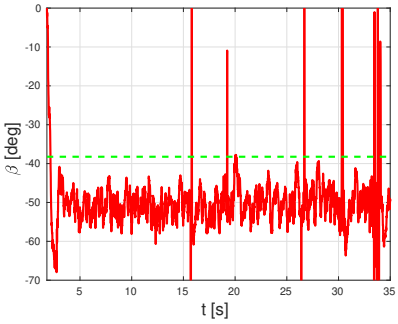

(d) *Sideslip angle*

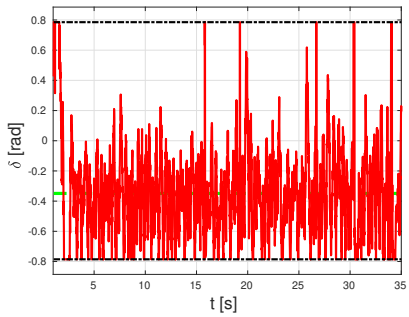

(e) *Steering angle*

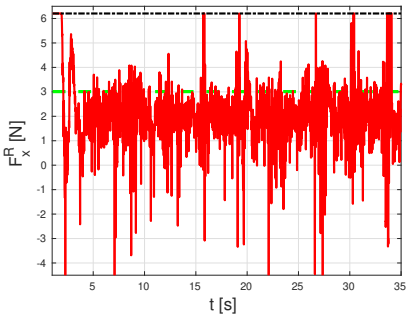

(f) *Rear tyre longitudinal force*

Figure 4.5: *Drifting stabilization on wood flooring surface, drifting tyre set and scaled car old configuration. Experimental data as red solid line, carpet surface equilibrium value as green dashed line and actuator saturation as black, dash-dotted line*

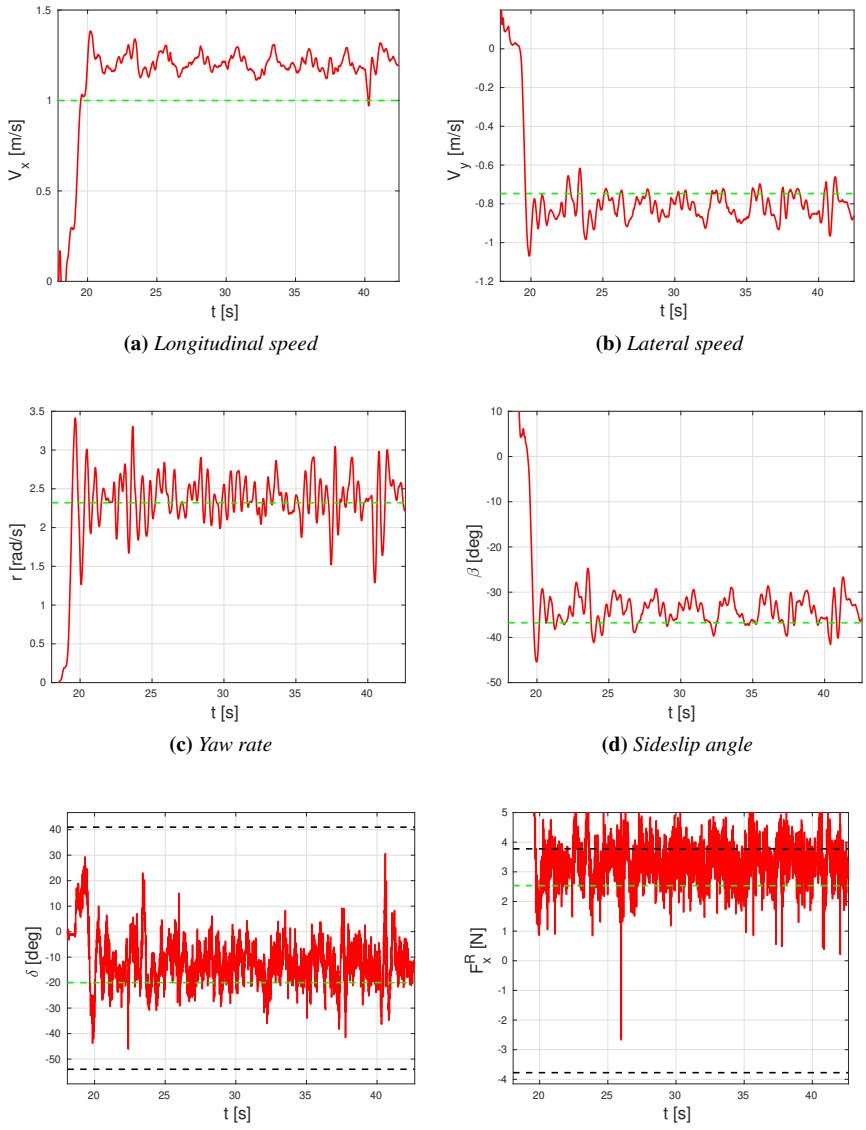

(a) *Longitudinal speed*

(b) *Lateral speed*

(c) *Yaw rate*

(d) *Sideslip angle*

(e) *Steering angle*

(f) *Rear tyre longitudinal force*

Figure 4.6: *Drifting stabilization on carpet surface, drifting tyre set and scaled car new configuration. Experimental data as red solid line, carpet surface equilibrium value as green dashed line and actuator saturation as black dashed line*

4.2 Autonomous drifting stabilization and circular path tracking

As already explained at the beginning of this Chapter, only a few works have considered drifting along with path tracking so far. In [64] a decoupled approach has been used: a steering controller tracks a reference course angle while a sliding mode throttle controller tracks reference sideslip angle. However, to follow a reference course angle does not mean to track a reference path. In [29] a coordinated throttle-steering control law has been designed to track a circular path while being in sustained drifting. The proposed approach was based on the assumption of controlling front tyre lateral force rather than front steering angle, and it was successfully tested on a real car. However, no robustness tests were performed. Finally, [65] presented a path-integral MPC which, although not being designed specifically for drifting, is able of holding car control even in presence of large sideslip angle and nonlinear dynamics. Even in this case, no robustness tests have been performed.
This Section presents, for the first time to the best of authors' knowledge, an extension of the LQR approach to the problem of drifting circular path tracking. The proposed control approach has been developed for a RWD vehicle, but it can be easily adapted to an AWD vehicle. An extensive experimental validation campaign has been performed, which includes several robustness tests.

4.2.1 System model and control approach

Single-track model given by eq. (4.1) has been extended to consider also path tracking state variables:

$$\begin{aligned} \dot{\Delta\psi} &= r - r_{ref} \\ \dot{e} &= V_x \sin(\Delta\psi) + V_y \cos(\Delta\psi) \\ \dot{I}_e &= e, \end{aligned} \tag{4.3}$$

in which r_{ref} represents the yaw rate at the equilibrium. Integral of path tracking error I_e has been introduced to get rid of steady state path tracking errors. For simplicity, ψ_{ref} has been computed as follows:

$$\psi_{ref} = \tan^{-1}\left(\frac{Y - Y_c}{X - X_c}\right) + \frac{\pi}{2}, \tag{4.4}$$

where X_c, Y_c defines the absolute position of the center of the reference circular path. Then, the same LQR control approach described in Sec-

Table 4.4: *LQR circular drifting stabilization controller parameters, for scaled new car configuration, carpet surface and drifting tyre set, without path tracking error intergral*

$\Delta V_{x,max}$	0.5	$\mathrm{m\,s^{-1}}$	$w_{\Delta V_x}$	1
$\Delta V_{y,max}$	0.45	$\mathrm{m\,s^{-1}}$	$w_{\Delta V_y}$	5
Δr_{max}	0.5	$\mathrm{rad\,s^{-1}}$	$w_{\Delta r}$	0.001
$\Delta \psi_{max}$	0.436	rad	$w_{\Delta \psi}$	0
Δe_{max}	0.25	m	$w_{\Delta e}$	0.5
$\Delta \delta_{max}$	0.45	rad	$w_{\Delta \delta}$	1
$\Delta F^r_{x,max}$	1.07	N	$w_{\Delta F^r_x}$	0.75

tion 4.1.2 has been used. In particular, nonlinear system given by eq. (4.1) and eq. (4.3) has been linearized around the steady state drifting equilibrium point computed in Section 4.1.3, with $\Delta\psi_{eq} = -\beta_{eq}$ and, obviously, $e_{eq} = 0$. Radius of reference circular path, for the selected drifting equilibrium point (see Section 4.1.3, Table 4.1), is equal to $0.539\,m$.

4.2.2 Experimental results

Even in this case, LQR circular drifting controller runs at $100\,Hz$ on a dedicated ROS node. In addition to this, simulations performed on nonlinear single-track model have been used to find a suitable initial controller tuning, which has been refined with experimental tests. Table 4.4 lists controller selected tuning parameters, in which Δe_{max} has been taken as equal to vehicle track. Figs. 4.7 and 4.8, along with a video[3], illustrate the results obtained without the integral on path tracking error. As expected, a steady-state path tracking error is present. When integral action is inserted (with controller's tuning parameters listed in Table 4.5) steady-state path tracking error converges to zero, as illustrated in Figs. 4.9, 4.10 and 4.11, 4.12 and a video of the experiment[4]. Convergence is quite slow due to the complexity of the maneuver and to actuators saturation, which limit the maximum achievable speed of closed-loop system response. In other words, a more aggressive controller tuning would results in closed-loop system instability. However, compared to the results obtained without the integral action on path tracking error, convergence speed is faster and basin of attraction is larger. In addition to this, controller is robust to friction coefficient and cornering stiffness variations, which occur on wood flooring surface.

[3]Available at `https://youtu.be/HqK_gv_fwCQ`

[4]A video of these experiments is available at `https://youtu.be/HqK_gv_fwCQ`

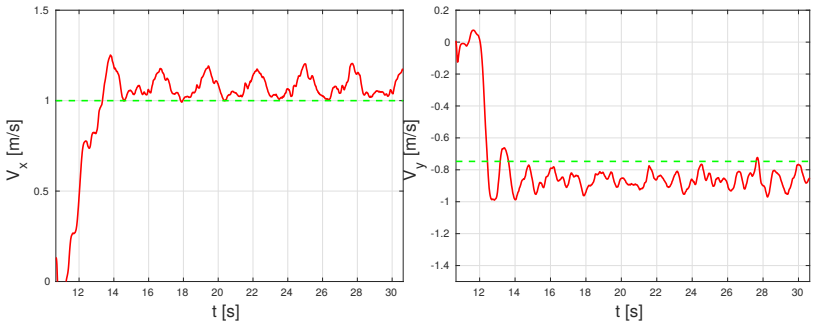

(a) *Longitudinal speed*

(b) *Lateral speed*

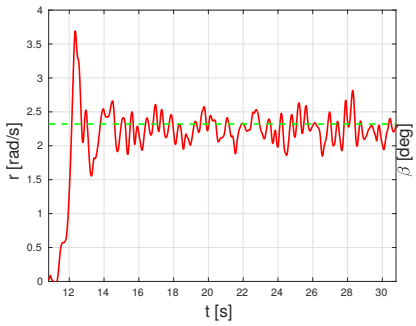

(c) *Yaw rate*

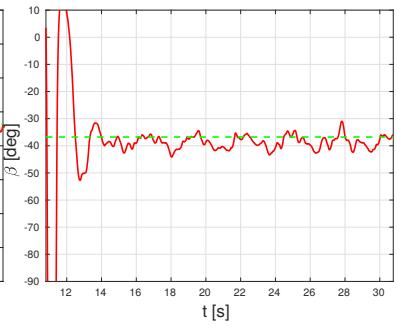

(d) *Sideslip angle*

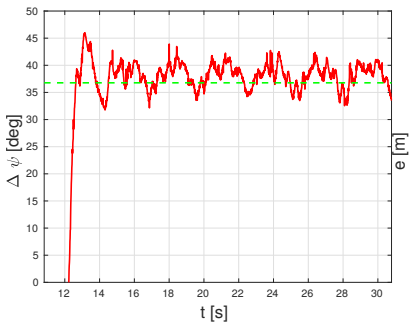

(e) *Attitude angle error*

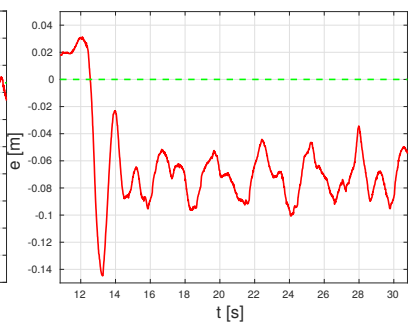

(f) *Path tracking error*

Figure 4.7: *Circular drifting stabilization on carpet surface, drifting tyre set and scaled car new configuration. Experimental data as red solid line, carpet surface equilibrium value as green dashed line*

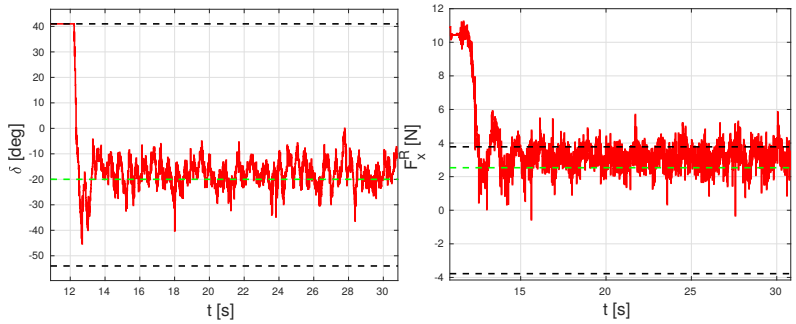

(a) *Steering angle* **(b)** *Rear tyre longitudinal force*

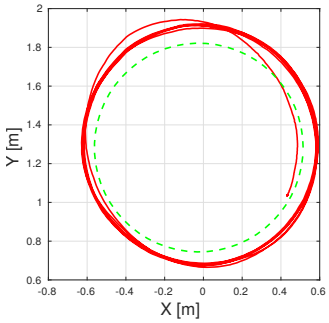

(c) *Followed path*

Figure 4.8: *Circular drifting stabilization on carpet surface, drifting tyre set and scaled car new configuration. Experimental data as red solid line, carpet surface equilibrium value as green dashed line and actuator saturation as black dashed line*

Table 4.5: *LQR circular drifting stabilization controller parameters, for scaled new car configuration, carpet surface and drifting tyre set, with path tracking error integral*

$\Delta V_{x,max}$	0.5	$\mathrm{m\,s^{-1}}$	$w_{\Delta V_x}$	1
$\Delta V_{y,max}$	0.45	$\mathrm{m\,s^{-1}}$	$w_{\Delta V_y}$	5
Δr_{max}	0.5	$\mathrm{rad\,s^{-1}}$	$w_{\Delta r}$	0.001
$\Delta \psi_{max}$	0.436	rad	$w_{\Delta \psi}$	0
Δe_{max}	0.25	m	$w_{\Delta e}$	$1\,10^{-5}$
$\Delta I_{e,max}$	1	ms	$w_{\Delta I_e}$	3
$\Delta \delta_{max}$	0.45	rad	$w_{\Delta \delta}$	1
$\Delta F^r_{x,max}$	1.07	N	$w_{\Delta F^r_x}$	1.25

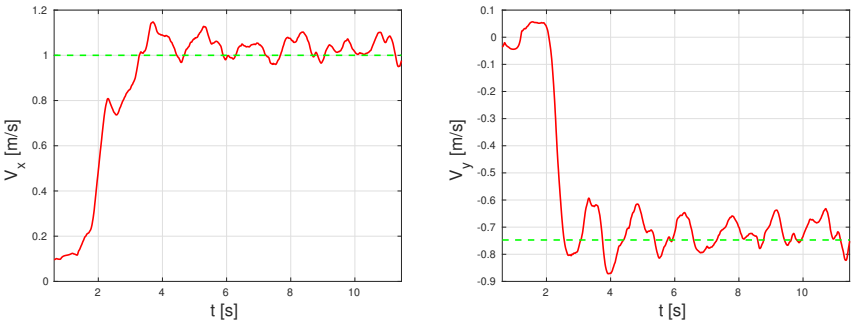

(a) *Longitudinal speed*

(b) *Lateral speed*

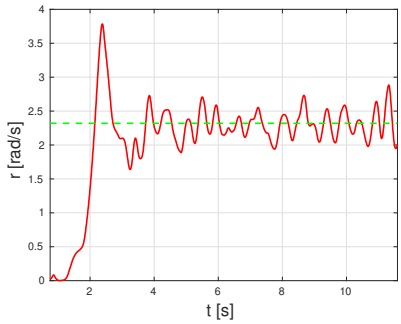

(c) *Yaw rate*

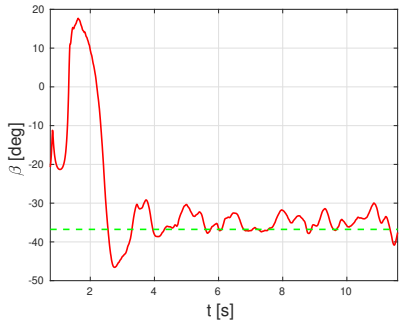

(d) *Sideslip angle*

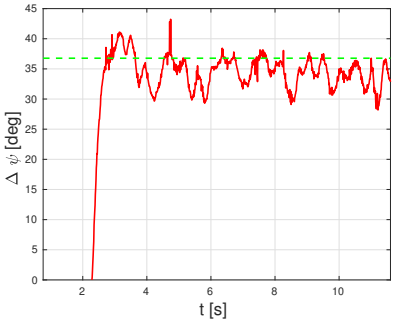

(e) *Attitude angle error*

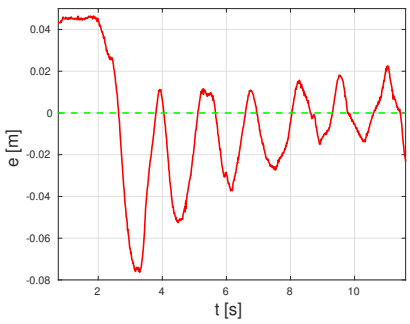

(f) *Path tracking error*

Figure 4.9: *Circular drifting stabilization with path tracking error integral action, carpet surface, drifting tyre set scaled car new configuration. Experimental data as red solid line, carpet surface equilibrium value as green dashed line. In this test, car started inside reference circular path*

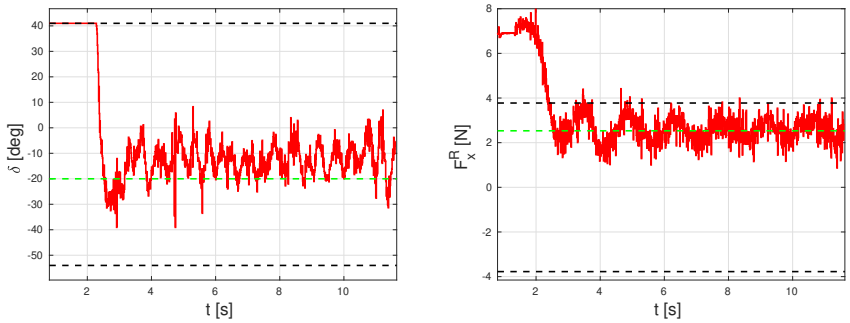

(a) *Steering angle* **(b)** *Rear tyre longitudinal force*

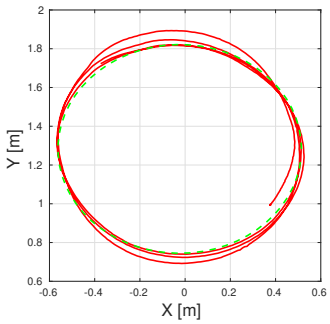

(c) *Followed path*

Figure 4.10: *Circular drifting stabilization with path tracking error integral action, carpet surface, drifting tyre set and scaled car new configuration. Experimental data as red solid line, carpet surface equilibrium value as green dashed line and actuator saturation as black dashed line. In this test, car started inside reference circular path*

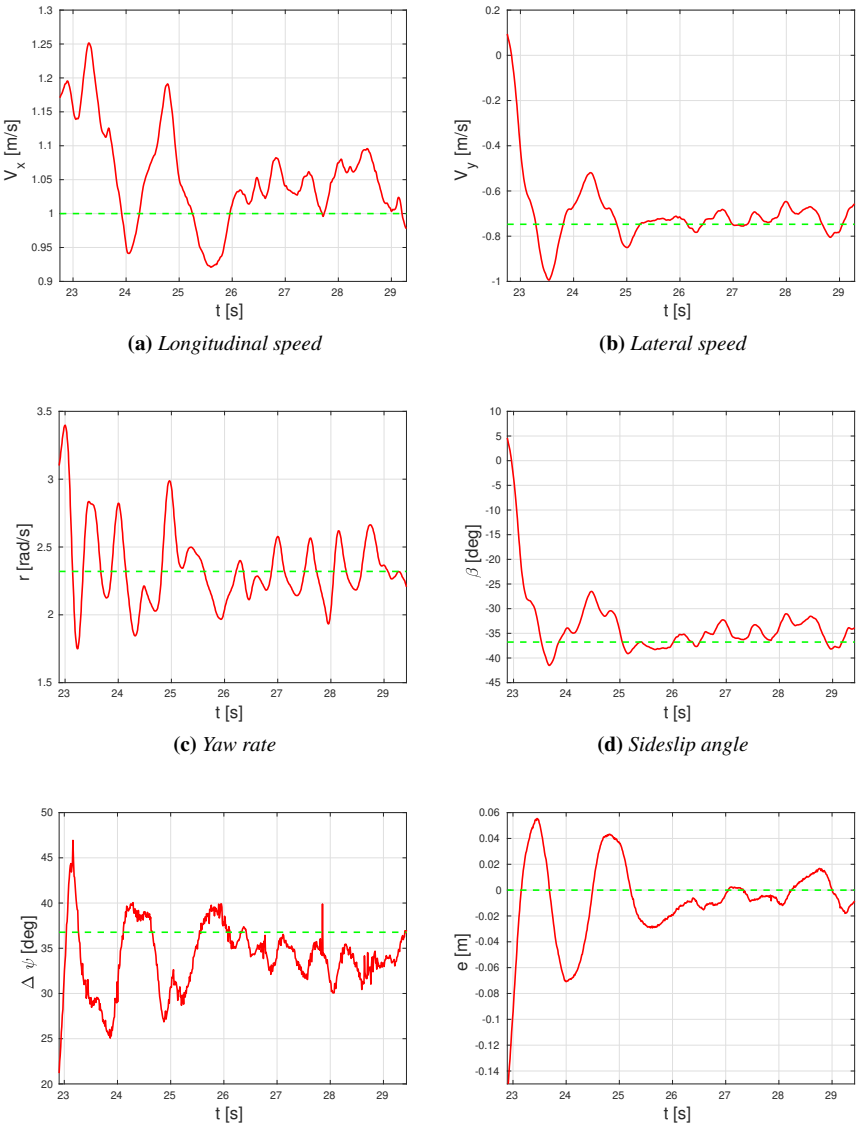

(a) *Longitudinal speed*

(b) *Lateral speed*

(c) *Yaw rate*

(d) *Sideslip angle*

(e) *Attitude angle error*

(f) *Path tracking error*

Figure 4.11: *Circular drifting stabilization with path tracking error integral action, carpet surface, drifting tyre set scaled car new configuration. Experimental data as red solid line, carpet surface equilibrium value as green dashed line. In this test, car started outside reference circular path*

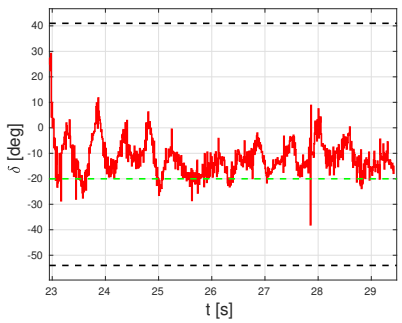

(a) *Steering angle*

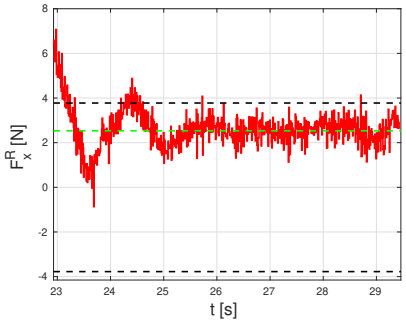

(b) *Rear tyre longitudinal force*

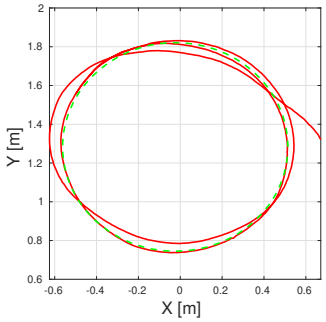

(c) *Followed path*

Figure 4.12: *Circular drifting stabilization with path tracking error integral action, carpet surface, drifting tyre set and scaled car new configuration. Experimental data as red solid line, carpet surface equilibrium value as green dashed line and actuator saturation as black dashed line. In this test, car started outside reference circular path*

CHAPTER 5

High speed autonomous driving with the Affine in the Force Input model

To be safer than their human counterpart, an automatic pilot must be capable of driving a car up to its handling limits, holding its control while exploiting all the grip made available by tyre-ground interaction, to avoid obstacles and follow the road, especially in an emergency scenario. However, the design of such a controller is not an easy task: nonlinearities of vehicle dynamics, which arise during the execution of aggressive manoeuvres, and the presence of multiple inputs and outputs, hamper the design of an automatic path-tracking controller by limiting considerably the range of control techniques which can be used, and by posing a challenge on the real-time feasibility of the control algorithm, when limited computational resources are available.
An obvious way to avoid the aforementioned issues, is to adopt a linear model of vehicle dynamics. However, classical [53] linear single-track models (see Section 2.0.4) cannot correctly reproduce vehicle dynamics up to the limits of handling [58], due to the linear lateral force model, given by eq. (2.19). A smart idea to circumvent this problem came from Stanford research group guided by professor Gerdes. In [8] the so-called Affine in the

Force Input (AFI) model was introduced. This single-track model assumes front tyre lateral force F_y^f as a virtual control input, in place of front tyre steering angle δ, yielding a linear model for the vehicle lateral dynamics:

$$\begin{aligned} \dot{\beta} &= \left(-\frac{C_\alpha^r}{mV_x}\right)\beta + \left(\frac{C_\alpha^r b}{mV_x^2} - 1\right) r + \left(\frac{1}{mV_x}\right) F_y^f \\ \dot{r} &= \left(\frac{bC_\alpha^r}{J_z}\right)\beta + \left(-\frac{b^2 C_\alpha^r}{J_z V_x}\right) r + \left(\frac{a}{J_z}\right) F_y^f. \end{aligned} \tag{5.1}$$

This model is linear under the following assumptions:

- small front tyre steering angle, so that $\cos\delta \simeq 1$;
- longitudinal speed V_x is constant or slowly varying, and is thus as a parameter instead of an input;
- linear rear tyre lateral force, i.e. $F_y^r \simeq -C_\alpha^r \alpha^r$. More in details, to increase model accuracy, rear tyre lateral force model can be iteratively linearized at current rear slip angle, as it has already been done in several works, which are described later on.

AFI model is suited to the design of linear path tracking controllers, which are capable of exploiting all the grip made available by tyre-ground interaction, as nonlinear constraint on maximum available lateral force translates into a linear bound on the maximum available control action, dictated by friction coefficient μ and front tyre normal load F_z^f:

$$|F_y^f| \leq \mu F_z^f. \tag{5.2}$$

In other words, with the adoption of AFI model, tyre lateral force model nonlinearity is extracted out of vehicle lateral dynamic model. Indeed, once the needed value of F_y^f has been computed, front tyre lateral model has to be inverted to calculate the steering angle δ [8].
AFI model has been used in several works to design linear path tracking controllers. In [8, 9], which mark the first appearance of AFI model, a linear controller based on MPC framework has been presented. The controller, which runs at $100\,Hz$, is based on the assumption of a constant vehicle longitudinal speed, and assists the driver in driving the vehicle at its limits of handling. Moreover, rear tyre lateral force has been iteratively linearized around current rear slip angle operating point, to achieve a better approximation of vehicle lateral dynamics. The controller has been tested on a real vehicle running at low speed (no more than $50\,Kmh^{-1}$) on a low-grip

terrain, and has been able to exploit all the grip made available by tyre-ground interaction. In [21], the approach has been extended to consider obstacle avoidance constraints. In [42], AFI model has been used to compute a feed-forward control action to autonomously follow a reference path while traveling at high speed. Then, a closed-loop controller based on the well-known linear single-track dynamic model has been superimposed to offset modeling errors and external disturbances. The proposed approach has been successfully tested on a real, high performance car on a dedicated test track. In [13] an MPC based autonomous path tracking controller has been designed and experimentally tested. Then, in [26] a prediction horizon with variable length time steps has been included, to cope with different time scales associated to vehicle stabilization and collision avoidance, while [57] describes a low-level control architecture suited to the direct control of front tyre lateral force.
In addition to these works from Stanford researchers, AFI model has been also used by other research groups. In [45] a path tracking controller based on model inversion has been developed and tested in simulation. Finally, in [50] AFI model has been used for designing a flatness-based path tracking controller, which has been tested in simulation.

5.1 Yaw rate oscillations at high speed

As stated before, to adopt AFI model means to assume front tyre lateral force as input to vehicle lateral dynamics. However, directly controlling F_y^f, yaw rate oscillations arise when the car is traveling at high speed[1], as it has been already observed, for example, in [50] and in [42]. Fig. 5.1 shows the response to a step of F_y^f of the Compact multi-body vehicle model (which was presented in Section 2.1), traveling at a constant longitudinal speed of $40\, ms^{-1}$. This simulation confirms the presence of non-negligible yaw rate and, consequently, sideslip angle oscillations when directly controlling front tyre lateral force at high vehicle speeds. These fluctuations severely hamper passenger riding comfort, reasonably giving them the feeling of an impending loss of car's control, and hence must be avoided. In [38], those yaw rate oscillations have been observed and they have been ascribed to the complex modeling of tyre lateral force at large velocities. In particular, [42] blamed a reduction of tyre damping, which occurs at high speed, as the most likely source of steering (and hence yaw rate) fluctuations. Despite this phenomenon may foster high speed yaw rate oscilla-

[1] As a general premise, we clarify that with "high speed"we refer to highway speeds, namely velocities between $100\, Kmh^{-1}$ and $140\, Kmh^{-1}$.

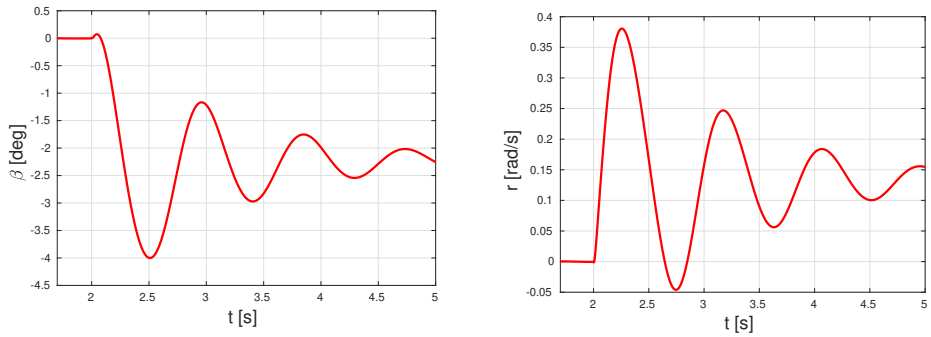

(a) *Sideslip angle* **(b)** *Yaw rate*

Figure 5.1: *Compact vehicle response to a step of front tyre lateral force. The car is traveling at a constant speed of* $40\,ms^{-1}$

tions, simulations performed on a nonlinear single-track dynamic model (see Section 2.0.3) based on Fiala tyre lateral force model (that does not include tyre stiffness and damping), reveal the presence of yaw rate oscillations when directly controlling F_y^f. Fig. 5.2 compares Sedan vehicle (see Section 2.1) response to a step of F_y^f and δ, when the car is traveling at different highway speeds. We conclude that an undamped yaw rate dynamics is the primary source of yaw rate oscillations at high vehicle speeds when F_y^f is the control input. Fig. 5.3 compares damping of the complex conjugate poles of yaw rate transfer function when either F_y^f or δ is the control input. As it can be seen, yaw rate undamped dynamics is present only when F_y^f is the control input.

5.2 The reason behind high speed yaw rate undamped dynamics

One of the novel aspects of this work is the explanation of the reason why AFI model exhibits an undamped yaw rate dynamics at high speed. The reason lies in the way the AFI model works. In fact, the adoption of front tyre lateral force as control input to car lateral dynamics, implicitly implies the implementation of the following procedure:

1. driver, or automatic controller, sets the required front tyre lateral force F_y^f;
2. tyre lateral force model is inverted, to determine required front tyre slip angle. Under the assumptions of small vehicle sideslip angle and

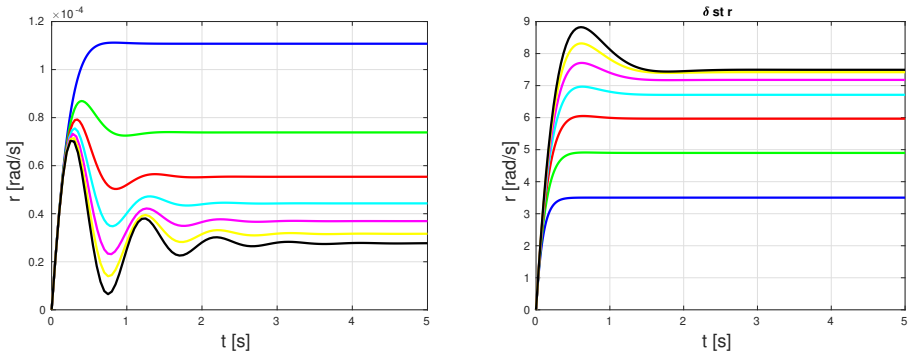

(a) *AFI model* **(b)** *Linear single-track model*

Figure 5.2: *Sedan yaw rate response to a step of either front tyre lateral force (AFI model) or front tyre steering angle (linear single-track model). Blue, green, red, cyan, magenta, yellow and black line refers to a speed of* 10, 15, 20, 25, 30, 35 *and* $40\,ms^{-1}$, *respectively*

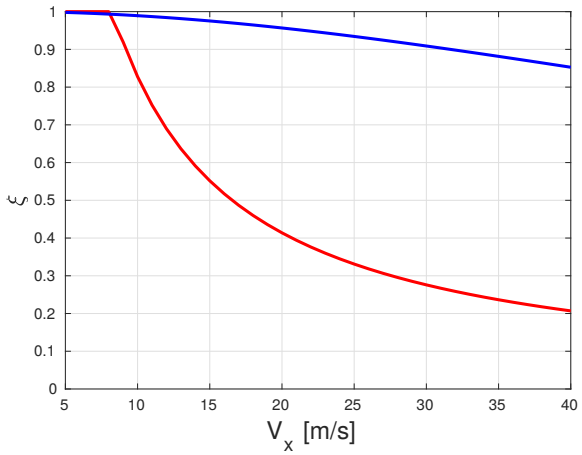

Figure 5.3: *Damping of yaw rate dynamics complex conjugate poles for Sedan vehicle: red line represents AFI model damping while blue line linear-single track model damping*

Figure 5.4: *AFI model working principle*

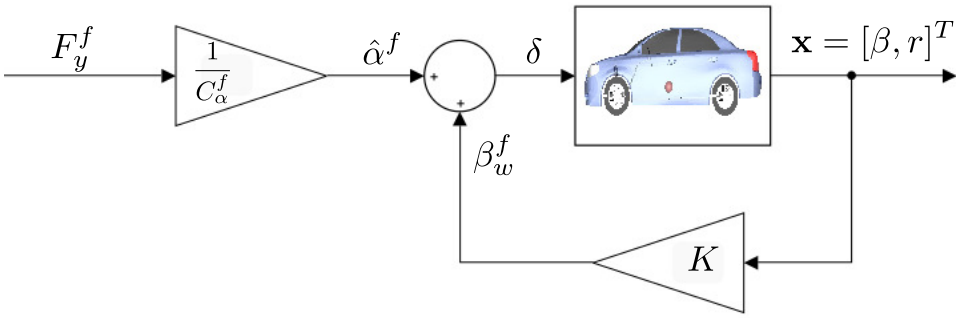

front tyre slip angle, linear tyre model can be used, so that

$$F_y^f = -C_\alpha^f \alpha^f = C_\alpha^f \hat{\alpha}^F, \tag{5.3}$$

in which $\hat{\alpha}^f$ is equal to $-\alpha^f$. Consequently,

$$\hat{\alpha}^f = F_y^f \frac{1}{C_\alpha^f}; \tag{5.4}$$

3. δ is computed in order to track required front tyre slip angle. In particular, when linear tyre model is considered, and $\hat{\alpha}^f$ has to be tracked, the following equation holds:

$$\begin{aligned} \delta &= \hat{\alpha}^f + \beta_w^f = \\ &= \hat{\alpha}^f + \beta + \frac{a}{V_x} r. \end{aligned} \tag{5.5}$$

Eq. (5.5) is nothing but a pole placement control law, in which β and r are the state variables and δ is the control input. In other words:

$$\begin{aligned} \delta &= \hat{\alpha}^f + \begin{bmatrix} 1 & \frac{a}{V_x} \end{bmatrix} \begin{bmatrix} \beta \\ r \end{bmatrix} \\ &= \hat{\alpha}^f + \begin{bmatrix} K_\beta & K_r \end{bmatrix} \begin{bmatrix} \beta \\ r \end{bmatrix} \\ &= \hat{\alpha}^f + K\mathbf{x}, \end{aligned} \tag{5.6}$$

with $\mathbf{x} = [\beta,\ r]^T$ as system state vector. Fig. 5.4 illustrates eq. (5.6). Therefore, AFI model, given by eq. (5.1), is equivalent to a linear single-track

model, with δ as control input, with the addiction of pole placement control law given by eq. (5.6). This equivalence, besides being also confirmed by the fact that these two models share the same zeros, as feedback does not modify the location of the zeros of a linear system, can also be analytically demonstrated. State-space matrices of linear single-track model with δ as control input and β and r as state variables are the following:

$$A_{st} = \begin{bmatrix} \dfrac{-C_\alpha^r - C^f}{mV_x} & \dfrac{C_\alpha^r b - C_\alpha^f a}{mV_x^2} - 1 \\ \dfrac{C_\alpha^r b - C_\alpha^f a}{J_z} & \dfrac{-C_\alpha^r b^2 - C_\alpha^f a^2}{J_z V_x} \end{bmatrix}, B_{st} = \begin{bmatrix} \dfrac{C_\alpha^f}{mV_x} \\ \dfrac{aC_\alpha^f}{J_z} \end{bmatrix} \tag{5.7}$$

When pole placement control law given by eq. (5.6) is applied, closed loop matrix becomes:

$$\begin{aligned} A_{cl} &= A_{st} + B_{st}K = \\ &= \begin{bmatrix} \dfrac{-C_\alpha^r - C_\alpha^f}{mV_x} & \dfrac{C_\alpha^R b - C_\alpha^f a}{mV_x^2} - 1 \\ \dfrac{C_\alpha^r b - C_\alpha^f a}{J_z} & \dfrac{-C_\alpha^r b^2 - C_\alpha^f a^2}{J_z V_x} \end{bmatrix} + \begin{bmatrix} \dfrac{C_\alpha^f}{mV_x} \\ \dfrac{aC_\alpha^f}{J_z} \end{bmatrix} \cdot \begin{bmatrix} 1 & \dfrac{a}{V_x} \end{bmatrix} = \\ &= \begin{bmatrix} \dfrac{-C_\alpha^r}{mV_x} & \dfrac{C_\alpha^r b}{mV_x^2} - 1 \\ \dfrac{C_\alpha^r b}{J_z} & \dfrac{-C_\alpha^r b^2}{J_z V_x} \end{bmatrix} \end{aligned} \tag{5.8}$$

It can be verified that A_{cl} is equal to AFI model state matrix, given by eq. (5.1). Morever, by dividing B_{st} by the term C_α^f, which represents the effect of eq. (5.4), AFI model control input matrix is obtained:

$$\begin{bmatrix} \dfrac{C_\alpha^f}{mV_x} \\ \dfrac{aC_\alpha^f}{J_z} \end{bmatrix} \cdot \frac{1}{C_\alpha^f} = \begin{bmatrix} \dfrac{1}{mV_x} \\ \dfrac{a}{J_z} \end{bmatrix} \tag{5.9}$$

To summarize, AFI model, given by eq. (5.1), is equivalent to a single-track model, with δ as control input, with the application of pole placement control law given by eq. (5.6). In particular, state feedback matrix K has not

been selected to optimize closed loop poles location, but to obtain a suitable change of variables. Consequently, AFI model displays poor damping of yaw rate and sideslip angle dynamics at high speed. In fact, K matrix terms are a function of vehicle longitudinal speed V_x.

5.3 AFI model stability analysis

To complete a control-oriented analysis of AFI model, which has never been presented so far to the best of author's knowledge, its stability has been analytically assessed. Recalling eq. (5.1), AFI model state matrix is given by:

$$A = \begin{bmatrix} \dfrac{-C_\alpha^r}{mV_x} & \dfrac{C_\alpha^R b}{mV_x^2} - 1 \\ \dfrac{C_\alpha^R b}{J_z} & \dfrac{-C_\alpha^r b^2}{J_z V_x} \end{bmatrix} \tag{5.10}$$

To simplify calculations, we rewrite A as follows:

$$A = \begin{bmatrix} -\sigma & \dfrac{\sigma b}{V_x} - 1 \\ \epsilon & -\dfrac{\epsilon b}{V_x} \end{bmatrix} \tag{5.11}$$

where $\sigma = \frac{C_\alpha^r}{mV_x}$ and $\epsilon = \frac{C_\alpha^R b}{J_z}$. Assuming V_x as a constant, AFI model is a time invariant dynamical system. A linear time invariant dynamic system is asymptotically stable if and only if each of its eigenvalues has a negative real part [10]. Thus, A eigenvalues (λ), given by determinant of $(\lambda I - A)$ have to be computed. The following characteristic equation is obtained:

$$det(\lambda I - A) = det \begin{vmatrix} \lambda + \sigma & 1 - \dfrac{\sigma b}{V_x} \\ -\epsilon & \lambda + \dfrac{\epsilon b}{V_x} \end{vmatrix} = \lambda^2 + \lambda \left(\frac{\epsilon b}{V_x} + \sigma \right) + \epsilon \tag{5.12}$$

As $\epsilon > 0$, asymptotic stability is guaranteed if:

$$\frac{\epsilon b}{V_x} + \sigma > 0. \tag{5.13}$$

which corresponds to:

$$\left(\frac{b^2}{J_z} + \frac{1}{m} \right) \frac{C_\alpha^r}{V_x} > 0 \tag{5.14}$$

As all the parameters involved in eq. (5.14) are positive, AFI model given by eq. (5.1) is asymptotically stable at any vehicle speed. Eq. (5.14) also corresponds to the real part of AFI eigenvalues, which, as it can be observed, is dependent on vehicle speed. In particular, the larger V_x, the smaller eigenvalues real part becomes.

5.4 AFI poles analysis

In general, a linear dynamic system displays an oscillatory behavior when its dominant poles are complex conjugate [10]. By analyzing the roots of characteristic equation given by eq. (5.12), it can be concluded that the undamped nature of yaw rate (and sideslip angle) dynamics emerges only at high speeds, as also confirmed by the numerical example shown in Fig. 5.3. In fact, roots of characteristic equation given by eq. (5.12) are complex when the following inequality holds:

$$\left(\frac{\epsilon b}{V_x} + \sigma\right)^2 - 4\epsilon < 0 \tag{5.15}$$

This inequality is a function of vehicle speed V_x, as it is the only parameter which can vary. Rearranging eq. (5.15), the following expression is obtained:

$$V_x > \sqrt{\frac{C_\alpha^r}{4}\left(\frac{b^3}{J_z} + \frac{2b}{m} + \frac{J_z}{bm^2}\right)} \tag{5.16}$$

Eq. (5.16) defines a speed threshold, below which AFI poles are real and hence no oscillatory behaviour is experienced; above this thresholds, poles are complex conjugate and yaw rate and sideslip angle oscillations arise.

Complex conjugate poles damping ratio can be computed starting from characteristic equation (5.12) [10], yielding:

$$\xi_{AFI} = \frac{\dfrac{b^2 C_\alpha^r}{J_z V_x} + \dfrac{C_\alpha^r}{m V_x}}{2\sqrt{\dfrac{C_\alpha^r b}{J_z}}} \tag{5.17}$$

As highlighted by eq. (5.17), damping is dependent on vehicle longitudinal speed V_x, as expected. Moreover, being this relationship an inverse proportionality, damping ratio decreases as speed increases.
Damping ratio of linear single-track model with δ as control input is equal

to:

$$\xi_\delta = \frac{\frac{b^2 C_\alpha^r + a^2 C_\alpha^f}{J_z V_x} + \frac{C_\alpha^r + C_\alpha^f}{m V_x}}{2\sqrt{\frac{(-C_\alpha^f a + C_\alpha^r b) m V_x^2 + C_\alpha^f C_\alpha^r (a+b)^2}{m V_x^2 J_z}}} \tag{5.18}$$

An analytical proof of the fact that $\xi_{AFI} < \xi_\delta$ at high speed has not been found yet, despite evident from numerical examples, as the one illustrated in Fig. 5.3.
Characteristic equation (5.12) also gives the analytical expression of complex conjugate poles natural frequency ω_n:

$$\omega_n = \sqrt{\epsilon} = \sqrt{\frac{C_\alpha^R b}{J_z}}. \tag{5.19}$$

Eq. (5.19) states that AFI intrinsic pole placement control law (5.25) modifies poles damping, which reduces as vehicle speed increase, while keeping at a constant value their natural frequency ω_n.

5.5 High speed path tracking using AFI model

AFI linear model given by eq. (5.1) is particularly suited to develop path tracking controllers based on the MPC framework, as the ones which have been used at low speeds in [9, 21, 26]. In fact, MPC is capable of easily controlling a linear MIMO system with constraints on both control inputs and system states. However, undamped AFI model yaw rate dynamics not only negatively affects system open loop response at high speed, but also the performance which can be achieved at high speed with a MPC based path tracking controller. In other words, there is no straightforward way that allows to find a tuning of the MPC parameters which ensures low yaw rate oscillations when the car is traveling at high speed. This statement has been numerically proved by designing a MPC path tracking controller, based on AFI model, and by testing it in simulation against a nonlinear single-track model of vehicle dynamics (which has been derived in Section 2.0.3). This simple model has been preferred over a more complex multibody vehicle model, as the ones described in Section 2.1, to get rid of the nonlinear effects given by load transfer, suspension motion and tyre stiffness and damping, so as to highlight how the direct control of F_y^f is enough to obtain yaw rate oscillations at high speed.

The tested MPC path tracking controller solves, at each time step, the following optimization problem:

$$\underset{u(\cdot)}{\text{minimize}} \quad J(x(k), u(\cdot), k) = \sum_{i=0}^{N-1} \left(\|x(k+i)\|_Q^2 + \|u(k+i)\|_R^2 \right) \tag{5.20}$$

$$\text{subject to} \quad x(k+1) = Ax(k) + Bu(k) \tag{5.21}$$

$$|e| \leq 1\,\text{m} \tag{5.22}$$

$$|F_y^f| \leq \mu F_z^f, \tag{5.23}$$

where:

- in eq. (5.20), N is the length of prediction horizon, $u(k) = F_y^f(k)$, Q and R are definite positive diagonal matrices which penalizes states and control inputs moves;
- eq. (5.21) defines system open loop dynamics, which is given by:

$$\begin{aligned} \dot{\beta} &= \left(\frac{-C_\alpha^r}{mV_x} \right) \beta + \left(\frac{C_\alpha^R b}{mV_x^2} - 1 \right) r + \frac{1}{mV_x} F_y^f \\ \dot{r} &= \left(\frac{C_\alpha^R b}{J_z} \right) \beta + \left(\frac{-C_\alpha^r b^2}{J_z V_x} \right) r + \frac{a}{J_z} F_y^f \\ \Delta\dot{\psi} &= r - r_{ref} \\ \dot{e} &= V_x(\Delta\psi + \beta), \end{aligned} \tag{5.24}$$

  where V_x is assumed to be constant, r_{ref} is the reference yaw rate computed as $r_{ref} = V_x \kappa(s)$, where $\kappa(s)$ defines the curvature of the road. In particular, we selected a chicane (s-turn) road profile, with constant curvature, as illustrated in Fig. 5.5;
- eq. (5.22) defines the constraint on path tracking error e, which is needed to force the vehicle to stay within road boundaries;
- eq. (5.23) expresses the upper bound on F_y^f dictated by friction coefficient μ and tyre normal load F_z^f.

Matlab model predictive toolbox[2] has been used to implement MPC controller in Simulink environment. Longitudinal vehicle speed has been set to $30\,ms^{-1}$, with the radius of road turns fixed to $150\,m$. System (5.24) has been discretized with Zero-Order-Hold (ZOH) method with a sampling time of $0.04\,s$ ($25\,Hz$). MPC prediction horizon N has been set to 25 steps,

[2] https://it.mathworks.com/products/mpc.html

Figure 5.5: *Road profile for the testing of the MPC path tracking controller based on AFI model*

so that the automatic driver is looking $1\,s$ ahead of the current position. Fig. 5.6 shows the best results which could be achieved, which are nevertheless characterized by strong yaw rate fluctuations, despite the car is correctly staying within road boundaries.

5.5.1 Pole placement to enhance yaw rate damping

Simulation results illustrated in the previous section let us conclude that AFI model cannot be used for developing an MPC path tracking controller which is capable of driving the car without yaw rate oscillations. An additional control loop, which increases AFI damping at high speed, is necessary. Therefore, we designed a pole-placement control law which increases the damping of AFI poles at high speed, in order to get rid of yaw rate oscillations. In particular, as V_x strongly affects the damping of AFI model as suggested by eq. (5.17), pole-placement has been designed on a selected longitudinal speed V_x. Pole placement control law acts on AFI model state variables, namely vehicle sideslip angle and yaw rate:

$$F_y^{F,pp} = -K_{pp}[\beta, r]^T \tag{5.25}$$

Fig. 5.7 illustrates pole placement control law along with AFI model.

As the aim of pole placement is simply to increase system damping at a given vehicle speed, closed loop poles have been selected to have the same natural frequency of those of AFI model (in particular,as indicated by eq. (5.19), ω_n keeps constant at any vehicle speed) but with a larger damping factor, which, for comfort requirements, has been selected to be at least 0.8. This choice of closed loop poles also minimizes the control effort

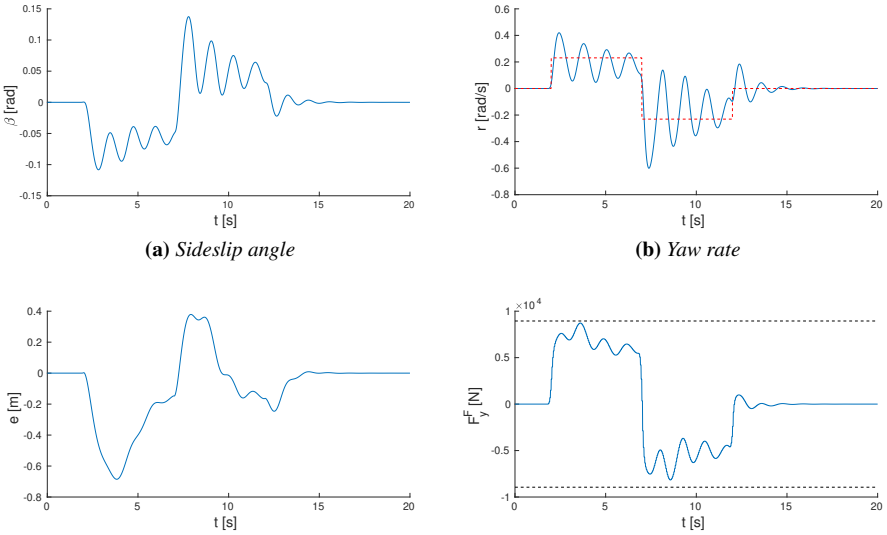

(a) *Sideslip angle* **(b)** *Yaw rate*

(c) *Path tracking error* **(d)** *Front tyre lateral force*

Figure 5.6: *Path tracking with MPC approach and AFI model: simulation results obtained with Sedan vehicle, traveling at a constant speed of* $30\,ms^{-1}$. *Simulation data as blue solid line, reference as red dashed line and saturation limits as black dashed line*

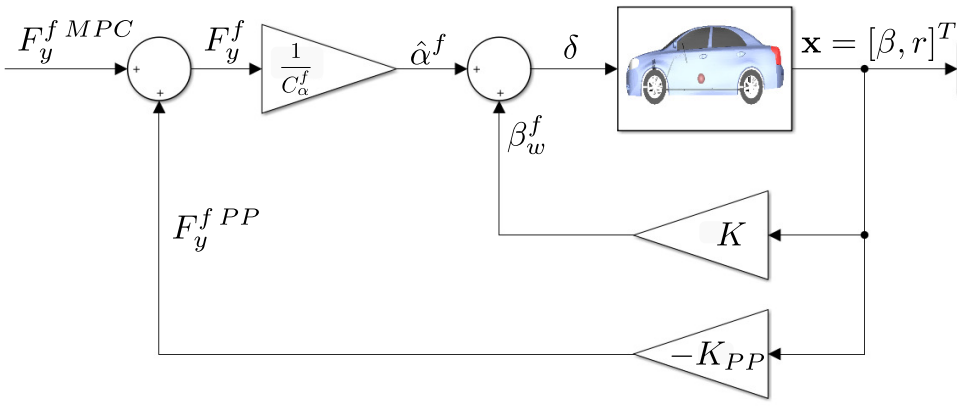

Figure 5.7: *AFI model and pole placement control law*

of pole-placement control law, as suggested in [6].

5.5.2 MPC path tracking controller with pole-placement internal control loop

Once AFI poles have been damped by pole-placement control law given by eq. (5.25), an external MPC controller, which accounts for path tracking, can be designed. Fig. 5.8 illustrates the overall control architecture which is needed to exploit AFI model for high speed path tracking control. MPC

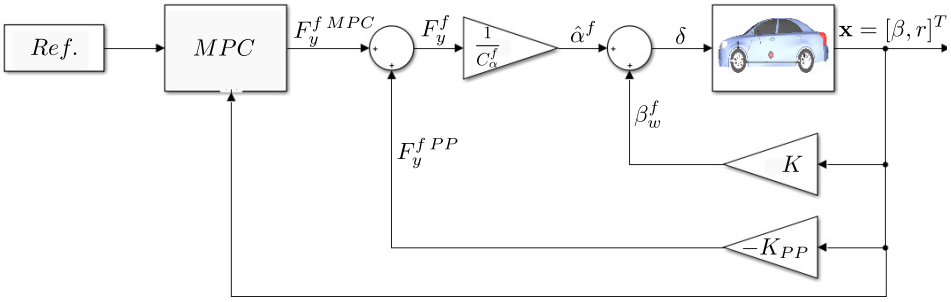

Figure 5.8: *Path tracking with MPC control approach and AFI model at high vehicle speed: overall control architecture*

solves the following optimization problem, at each time step:

$$\underset{u(\cdot)}{\text{minimize}} \quad J(x(k), u(\cdot), k) = \sum_{i=0}^{N-1} \left(\|x(k+i)\|_Q^2 + \|u(k+i)\|_R^2 \right) \tag{5.26}$$

$$\text{subject to} \quad x(k+1) = Ax(k) + Bu(k) \tag{5.27}$$

$$|e| \leq 1\,\text{m} \tag{5.28}$$

$$|F_y^{F,MPC} + F_y^{F\,PP}| \leq \mu F_z^f, \tag{5.29}$$

In particular:

- eq. (5.27) refers to the dynamic system which results from the application of the pole placement control;
- eq. (5.29) highlights that maximum front tyre lateral force available to MPC at each time step, depends on the effort requested by the pole placement to enhance the damping ratio of the AFI model.

Fig. 5.9 illustrates the results achieved on the same simulation scenario which was used in Section 5.5; pole placement control law has been selected in order to set closed loop poles damping ratio to 0.9, while keeping

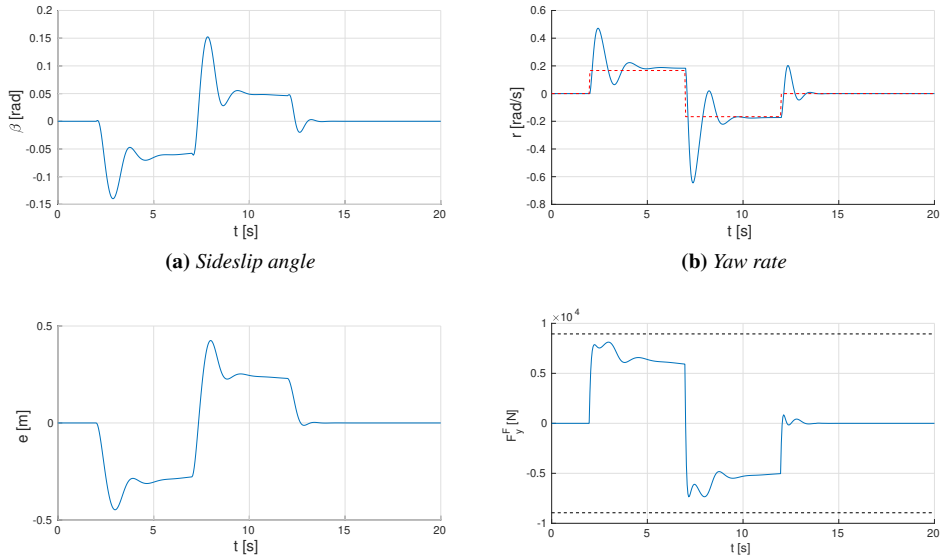

(a) *Sideslip angle* **(b)** *Yaw rate*

(c) *Path tracking error* **(d)** *Front tyre lateral force*

Figure 5.9: *Path tracking with MPC approach, pole placement and AFI model: simulation results obtained with Sedan vehicle, traveling at a constant speed of* $30\,ms^{-1}$ *and damping of AFI closed loop poles equal to* 0.9*. Simulation data as blue solid line, reference as red dashed line and saturation limits as black dashed line*

a constant natural frequency, which was equal to $6.3\,rad\,s^{-1}$. As it can be seen, pole placement control law allows to find a tuning of MPC path tracking controller which ensures no yaw rate oscillations.

5.5.3 Discussion

Although results shown in Section 5.5.2 suggests that it is possible to use AFI model for high speed path tracking at the limits of handling, two issues remain:

- constraint (5.29) implies that, with the developed nested-loops control architecture, MPC controller has to manage the amount of F_y^f which is not being used by pole placement control law to increase AFI damping and avoid yaw rate oscillations. However, when driving a car, the most important requirement is to avoid collisions and to stay on the road. The damping of yaw rate oscillations is a secondary task, which can be addressed only when the car is traveling in a safe condition, without the risk of impeding accidents. This reasoning suggests that the damping of closed loop AFI poles should not be fixed but should

be dynamically adapted to match current situation: when there is the risk of a collision, all control effort should be left to MPC path tracking controller; when there is not risk of collision or no sharp turns have to be navigated, damping and hence pole placement control effort can be increased to improve passengers comfort.
A way of avoiding this issue is to take advantage of a rear-wheel steering mechanism, as it has been done in [2] and in its subsequent works, whose results have been collected in [3]. In these researches, path tracking and yaw damping tasks have been decoupled. More in details, path tracking task, with F_y^f as control variable, has been assigned to front wheel steering angle δ, while yaw dynamics damping has been given to rear wheel steering angle;

- the analysis performed in this Chapter, along with all the works in the literature which have used AFI model, have assumed that steering actuator dynamics is fast enough to be neglected. Moreover, no steering actuator delay has ever been considered. However, when a delay on steering actuation is present, yaw rate oscillations at high speed are further increased, even in presence of pole placement control law presented in Section 5.5.1.

CHAPTER 6

Conclusions and future developments

This work investigated control approaches suited to the development of path tracking controllers able to drive an autonomous car up to its limits of handling.
Chapter 4 showed that LQR is a simple yet robust and effective control approach for drifting stabilization and tracking of a circular path. Moreover, the performed experimental tests has revealed that a low-level longitudinal slip tracking controller is not necessary. LQR is able to automatically adapt F_x^r to a reduction of tyre-ground friction coefficient, thus avoiding car spinning. This interesting phenomenon is due to the feedback of vehicle lateral velocity, which prevents the application of a too large throttle action, and to the fact that the adopted vehicle dynamic model takes into account the effect of F_x^r on vehicle lateral dynamics. In other words, the feedback of lateral velocity, plus the knowledge of the effect of F_x^r on yaw rate and lateral velocity, give to the controller the ability to foresee, and hence avoid, spinning.
Chapter 5 has analyzed and discussed the adoption of the Affine in the Force Input (AFI) model for the design of high speed path tracking controllers, able to exploit all the grip made available by tyre-ground interaction. In fact, the most useful AFI model feature is the easy, i.e., linear expression

of the constraint on the maximum lateral force which can be developed by tyre, that dictates vehicle maximum lateral acceleration. However, when directly controlling front tyre lateral force, yaw rate oscillations arise at vehicle high speed. These fluctuations are due to undamped yaw rate dynamics, which, as illustrated, is due to a hidden control loop, that is closed in order to control F_y^f. Moreover, AFI pole damping decreases as vehicle speed increases, as demonstrated by a simple analytical relation. In the absence of a rear-wheel steering mechanism, the only viable option for increasing the damping of yaw rate dynamics at high speed is to design a pole placement control law, which takes F_y^f as the control variable. This control strategy has been tested in simulation along with a MPC path tracking controller. It was shown that the proposed nested loops control architecture is able to successfully track a reference path, without dangerous yaw rate oscillations at high vehicle speed.
Last but not least, a scaled car was built for the purpose of this research project. Its parameters have been estimated, and the dynamics of its steering actuator has been identified. The most promising result is the accuracy with which nonlinear single-track model, which is the model typically adopted for the design of real car path tracking controllers and ADAS, reproduces vehicle lateral dynamics, up to the limits of handling. In addition, the dynamic similitude between the experimental platform and a Sedan vehicle confirms that a scaled vehicle, in place of a real car, can be used to assess the performances, the robustness and the shortcomings of path tracking controllers, while avoiding the danger and the cost of accidental collisions.

6.1 Future developments

Each chapter of this work has several future developments, which are here discussed.

6.1.1 Scaled car

The most important improvement of scaled car experimental platform consists in making it fully autonomous, i.e., estimating directly onboard all the needed states without relying on any external motion tracking system, thus opening the door to outdoor testing. In particular:

- longitudinal speed V_x could be measured with a wheel encoder. The tight available space poses the biggest challenge for the design and building of such an encoder, preventing the installation of a commer-

cial encoder. Indeed, not only commercial encoders are too big to be installed in the scaled car, but also the smallest ones available on the market cannot be mounted because of very tight mounting tolerances to be satisfied in order to work properly. Nevertheless, we successfully tested an hand-made optical encoder, which is shown in Fig. 6.1, which is made of a chequered paper strip sensed by a photo-reflective infrared sensor. The voltage signal generated by the sensor is squared by means of a Schmidt trigger and then sent to the Arduino, which computes wheel speed. The drawback of this configuration is the large amount of computational resources wasted by the encoder routine, which calls for a dedicated board. A possible and better solution could be the development of an hardware counter, which directly provide pulses number at the Arduino board at a given frequency;

- lateral velocity V_y, or vehicle sideslip angle β, could be estimated with a kinematic estimator, as the one presented in [56], which uses only the measures of V_x, yaw rate r and lateral acceleration a_y, while being also suited for drifting maneuvers. In addition to this, such an estimator would be analogue to those used in real cars, in contrast to the optical-flow based sideslip angle estimator used in [31];

- path tracking states e and $\Delta\psi$ could be estimated with an onboard camera, mounted on car rooftop.

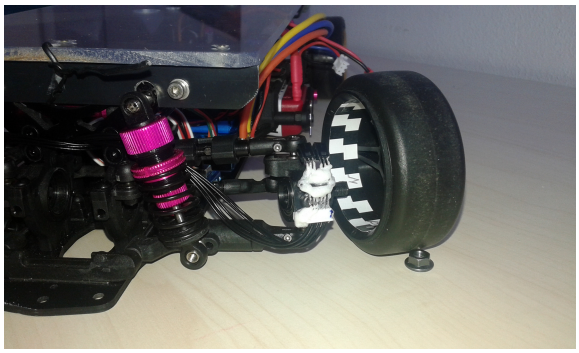

Figure 6.1: *Scaled car hand-made wheel encoder*

Another characteristic of this experimental setup which could be improved is the transmission delay which plagues the transmission of control commands to steering and motor actuators. The delay could be reduced by:

- increasing the serial port frequency, which calls for a board more powerful than the Arduino Uno;
- increasing the speed of PWM signals. Currently, VESC only accepts standard RC PWM signals, with a frequency of $60\,Hz$. Therefore, in order to increase the speed of the connection, either VESC firmware has to be modified or a faster signal (as, for example, a CAN BUS signal) has to be used. Regarding the steering servo, nowadays servos are digital, with an internal working frequency of about $330\,Hz$. Therefore, in theory, it could be possible to increase PWM signal frequency up to this value, even if no tests have been conducted so far.

6.1.2 Drifting stabilization and path tracking

The most straightforward development of this Section lies in the assessment of LQR path tracking capabilities in the presence of a non perfectly circular reference path. For instance, the controller could be tested against a spiral path (which can be though as a circular trajectory, with a non-constant radius), or against a circular path, whose center is translating at constant speed.
Moreover, although the LQR approach is incredibly robust, often control commands exceed actuator saturation limits (see for example Fig. A.2). In these cases, asymptotic stability of closed-loop system cannot be guaranteed. Moreoever, actuator saturation prevented the adoption of a more aggressive control law, which would yield a faster closed-loop response. Therefore, the most straightforward improvement of this research is the development of an MPC circular drifting controller. Indeed, MPC is well-suited to the problem of controlling MIMO systems with limited control actions [44]. MPC main drawback is the need of a large amount of computational resources. Finally, both LQR and MPC drifting path tracking controllers could be designed on a linearized model which takes into account longitudinal load transfer, to assess whether better results can be achieved.

6.1.3 High speed driving with AFI model

The first future development of this Section is the experimental validation, on the scaled car, of the pole placement control law, designed to increase yaw rate damping at high speed. This test has not been conducted so far due to the need of running the car at high speed (about $7\,ms^{-1}$), a velocity which calls for a wider area covered by Motion Tracking system, compared to the current 4 times $4\,m$ available test area. The testing of the complete

path tracking control architecture, which leverages on AFI model, on the scaled car is made complex by MPC, which needs a large amount of computational resources to be run in real time at a sufficiently small sampling time.
In addition to the aspects discussed in Section 5.5.3, another future development of this work is the investigation of an analytical proof of AFI model lower damping of yaw rate dynamics, compared to the damping of yaw rate dynamics of single-track model with δ as control input.
Finally, as already stated before, pole placement control law introduced in Section 5.5.1 has been designed assuming a constant vehicle speed. Therefore, if vehicle velocity changes, pole placement control law has to be designed again. Linear Parameter Varying (LPV) control could be adopted to address this challenge. Furthermore, being AFI model state vector made of just two state variable, pole placement gains can be analytically calculated and hence computed for any vehicle speed. The design of a path tracking controller in the presence of a non-constant vehicle longitudinal speed V_x (which is the case, for example, of a sudden obstacle avoidance manoeuvre) could be alternatively addressed by means of a feedback linearization policy [41], which would yield a linear system even in presence the of a varying V_x. In particular, thanks to the adoption of F_y^f as control input, vehicle and path tracking dynamics are modeled by a nonlinear but affine in the control input system, the class of nonlinear systems for which feedback linearization can be applied [41].

Appendices

APPENDIX $\mathcal{A}$

Autonomous drifting and circular path tracking with LQR approach: additional experimental results

A.1 Drifting stabilization with scaled car newest configuration

LQR autonomous drifting stabilizing controller robustness against external disturbance forces and parameter uncertainties have been assessed by means of the following experiments performed on the scaled car, in addition to the stabilizing test illustrated in Section 4.1.4:

- Fig. A.1 depicts the results achieved by running the car on wood flooring surface. More in details, this experimental test assessed controller robustness to an error on friction coefficient and on front and rear cornering stiffness, which vary on different surfaces, as reported in Table A.1;
- Figs. A.2 and A.3 shows the ability of the LQR drifting stabilization controller to reject lateral force and yaw moment disturbances, while the car is traveling on wood flooring surface. In particular, Fig. A.2 illustrates vehicle response to a yaw moment applied to the car at $23\ s$

Appendix A. Autonomous drifting and circular path tracking with LQR approach: additional experimental results

Table A.1: *Comparison between scaled car parameters on carpet and wood flooring surface, with drifting tyre set*

Parameter	Carpet	Parquet	Increment
μ	0.385	0.255	$-34\,\%$
C_α^f $\left[\mathrm{N\,rad^{-1}}\right]$	50.13	244.51	$-388\,\%$
C_α^r $\left[\mathrm{N\,rad^{-1}}\right]$	122.05	224.41	$-84\,\%$

in order to spin it: the controller automatically counter-steers and releases throttle action to avoid spinning, then throttle action is increased again to increase yaw rate. Fig. A.3 shows vehicle response to a lateral force which simulates the hitting of an obstacle which tends to force the car to exit from sustained drifting at $50\,s$. The controller automatically steers towards the inside of the turn and accelerates more, to increase yaw rate moment and to go back to sustained drifting;

- Fig. A.6 and A.5 show the results achieved by the controller when an additional mass is placed at the rear and at the front of the scaled car, respectively, as depicted in Fig. A.4. These tests allow to evaluate controller robustness against mass, yaw moment of inertia and center of gravity position uncertainty. In particular, additional mass was equal to $0.4\,Kg$ and it has been placed at $40\,mm$ behind car rear axle, inducing the changes of car inertial parameters listed in Table A.2, or at $30\,mm$ behind front axle, inducing the changes of car inertial parameters shown in Table A.3. It was observed that, in general, the controller is more robust against a shift of the center of gravity towards the rear of the car, because when weight is moved towards the front of the car the rear has less available force and hence the car more easily spins.

Finally, in view of developing in the future a drifting stabilization Model Predictive Controller (MPC), which cannot work at a frequency of $100\,Hz$ due to computational load, robustness of LQR controller to a reduction of controller sampling time has been evaluated. It has been verified that the controller still produces satisfying performances down to a frequency of $25\,Hz$, as shown in Fig. A.7. Fig. A.8 displays the results achieved when the controller runs at $20\,Hz$: yaw rate oscillations, due to the additional controller delay, appears, yielding unsatisfactory results.

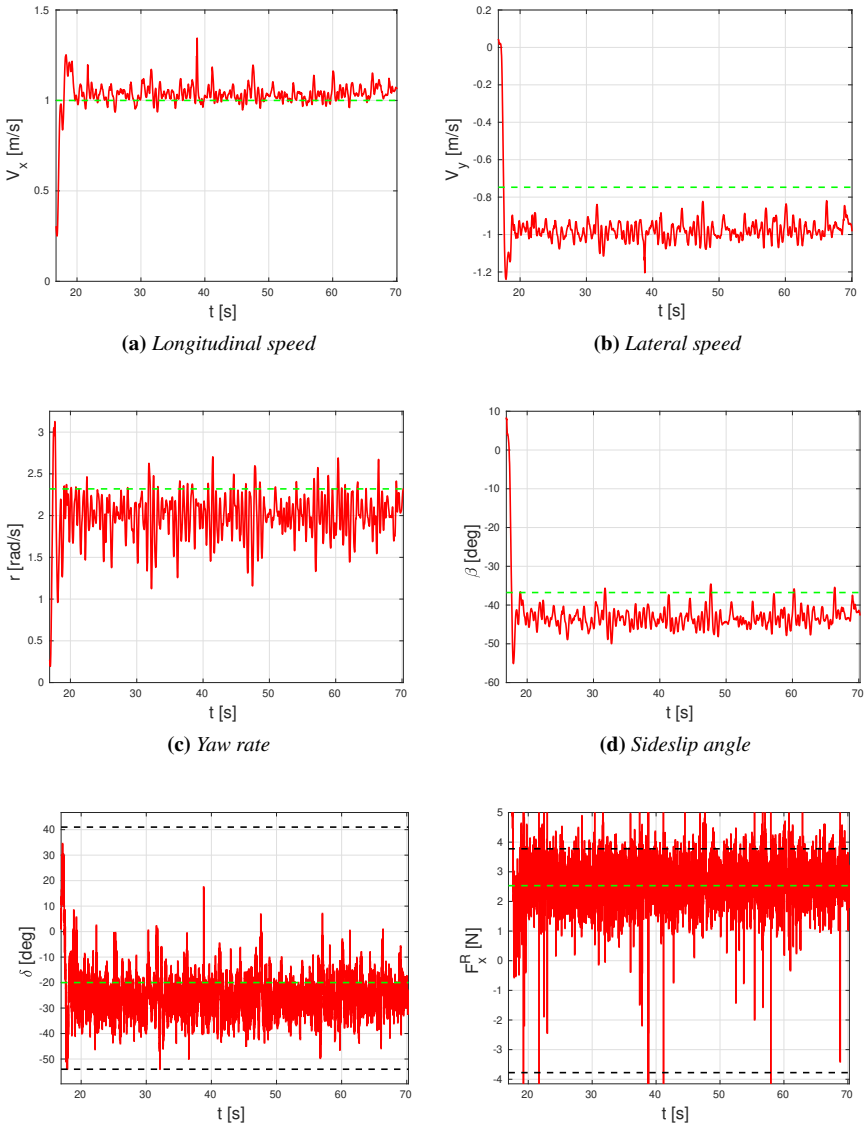

(a) *Longitudinal speed*

(b) *Lateral speed*

(c) *Yaw rate*

(d) *Sideslip angle*

(e) *Steering angle*

(f) *Rear tyre longitudinal force*

Figure A.1: *Drifting stabilization on wood flooring surface, drifting tyre set and scaled car new configuration. Experimental data as red solid line, carpet surface equilibrium value as green dashed line and actuator saturation as black dashed line*

Appendix A. Autonomous drifting and circular path tracking with LQR approach: additional experimental results

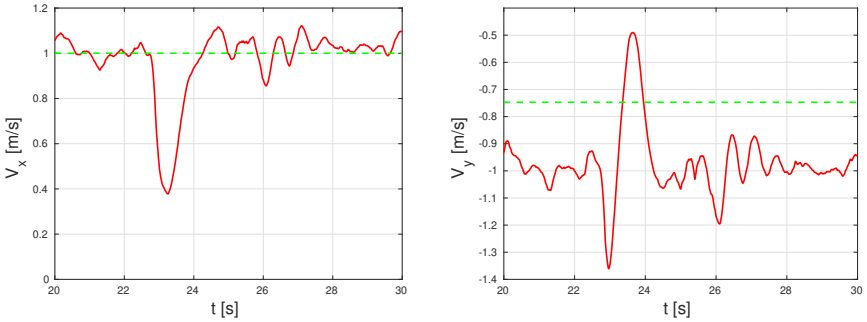

(a) *Longitudinal speed*

(b) *Lateral speed*

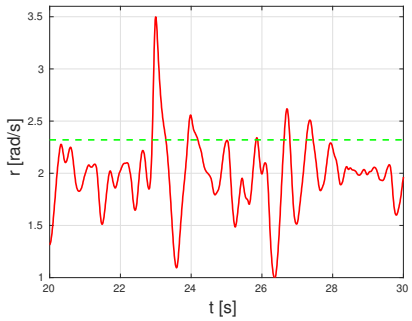

(c) *Yaw rate*

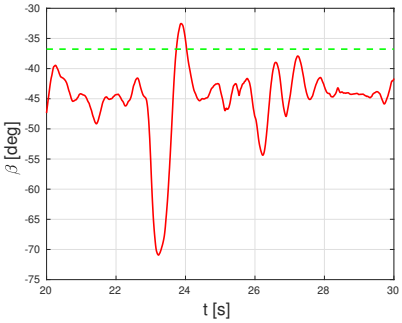

(d) *Sideslip angle*

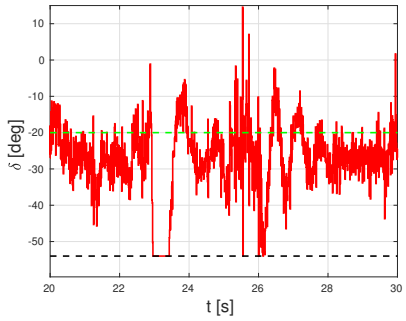

(e) *Steering angle*

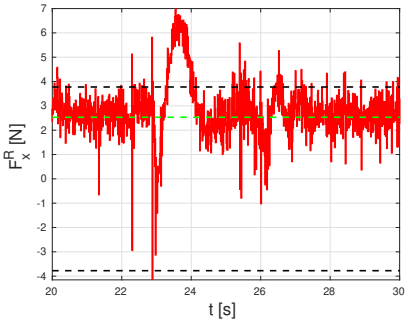

(f) *Rear tyre longitudinal force*

Figure A.2: *Drifting stabilization on wood flooring surface, drifting tyre set and scaled car new configuration, in presence of an external yaw momentum which tends to spin the car. Experimental data as red solid line, carpet surface equilibrium value as green dashed line and actuator saturation as black dashed line*

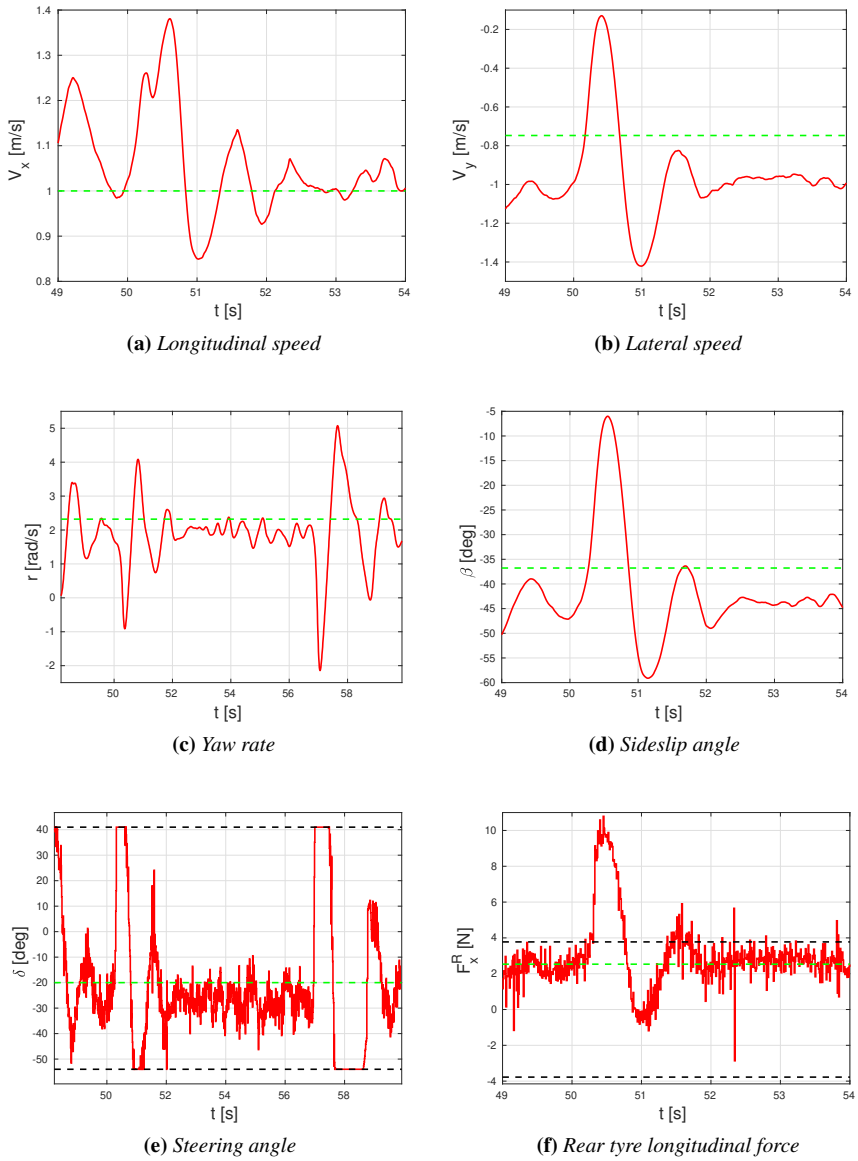

(a) *Longitudinal speed*

(b) *Lateral speed*

(c) *Yaw rate*

(d) *Sideslip angle*

(e) *Steering angle*

(f) *Rear tyre longitudinal force*

Figure A.3: *Drifting stabilization on wood flooring surface, drifting tyre set and scaled car new configuration, in presence of an external lateral force which tends to force the car to exit from sustained drifting. Experimental data as red solid line, carpet surface equilibrium value as green dashed line and actuator saturation as black dashed line*

Appendix A. Autonomous drifting and circular path tracking with LQR approach: additional experimental results

Table A.2: *Scaled car inertial parameters with an additional mass mounted at the rear of the car*

Parameter	Value	Increment
m [Kg]	2.231	$+17\,\%$
a [m]	0.16	$+17\,\%$
b [m]	0.1	$-19\,\%$
J_z [Kg m^2]	0.0363	$+25\,\%$

Table A.3: *Scaled car inertial parameters with an additional mass mounted at the front of the car*

Parameter	Value	Increment
m [Kg]	2.231	$+17\,\%$
a [m]	0.1208	$-12\,\%$
b [m]	0.1392	$+13\,\%$
J_z [Kg m^2]	0.0321	$+11\,\%$

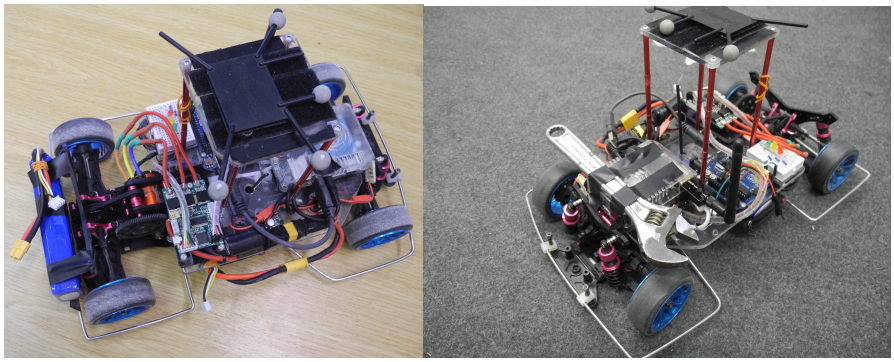

(a) *Rear* **(b)** *Front*

Figure A.4: *Scaled car with additional mass mounted*

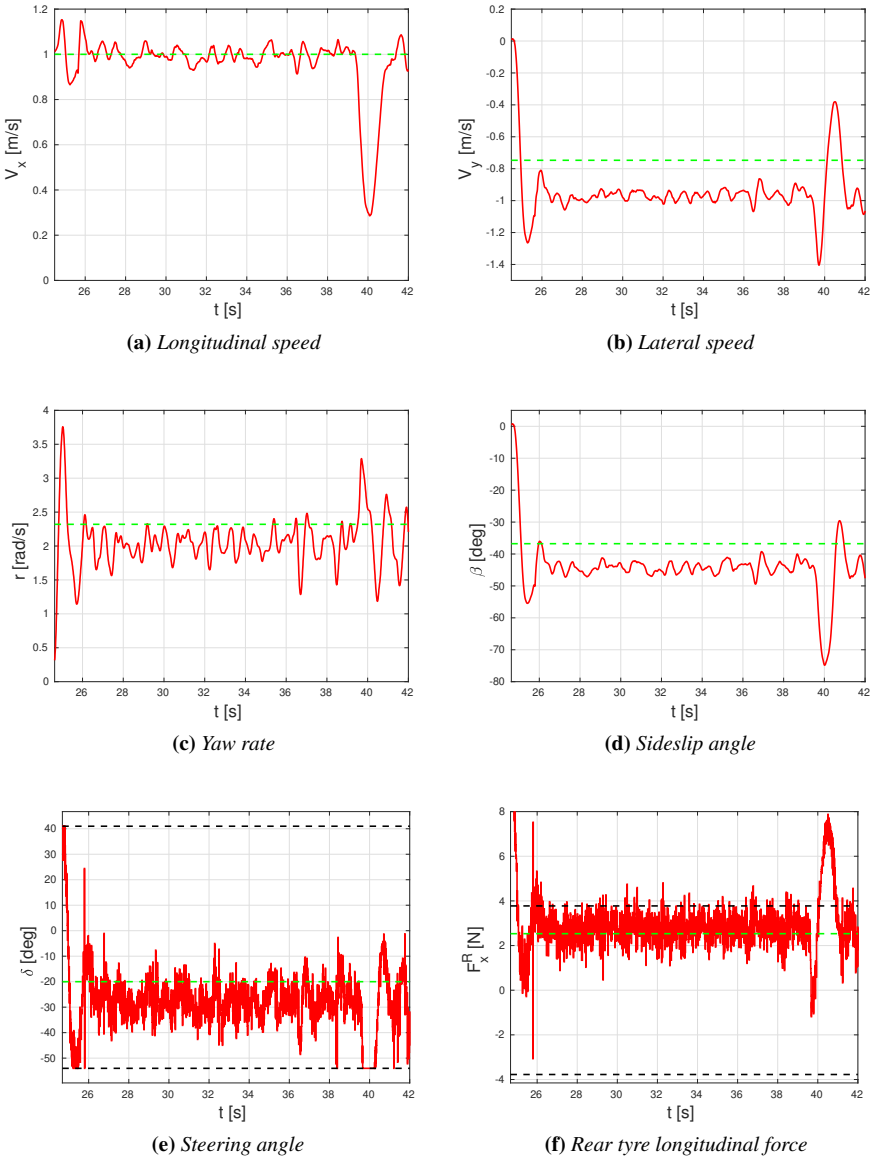

(a) *Longitudinal speed*

(b) *Lateral speed*

(c) *Yaw rate*

(d) *Sideslip angle*

(e) *Steering angle*

(f) *Rear tyre longitudinal force*

Figure A.5: *Drifting stabilization on wood flooring surface, drifting tyre set and scaled car new configuration, in presence of an additional mass on front car axle. At* $40\ s$ *an external yaw moment, which tends to spin the car, is applied. Experimental data as red solid line, carpet surface equilibrium value as green dashed line and actuator saturation as black dashed line*

Appendix A. Autonomous drifting and circular path tracking with LQR approach: additional experimental results

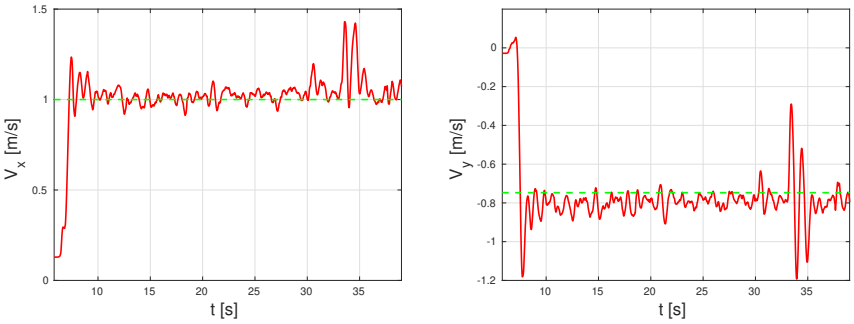

(a) *Longitudinal speed*

(b) *Lateral speed*

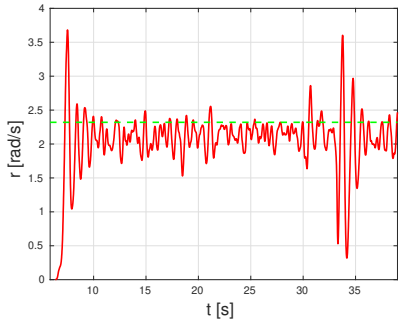

(c) *Yaw rate*

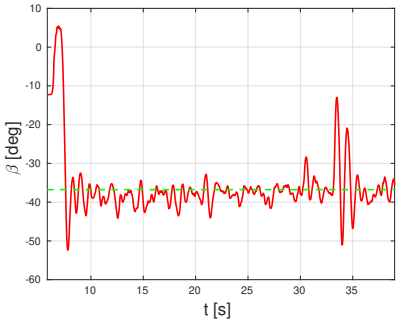

(d) *Sideslip angle*

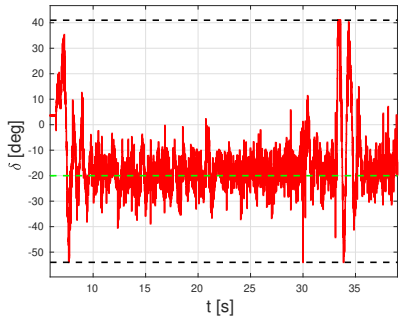

(e) *Steering angle*

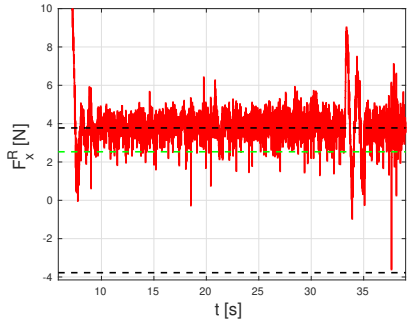

(f) *Rear tyre longitudinal force*

Figure A.6: *Drifting stabilization on wood flooring surface, drifting tyre set and scaled car new configuration, in presence of an additional mass on rear car axle. At* 33 *s an external lateral force, which tends to make the car exit from sustained drifting, is applied. Experimental data as red solid line, carpet surface equilibrium value as green dashed line and actuator saturation as black dashed line*

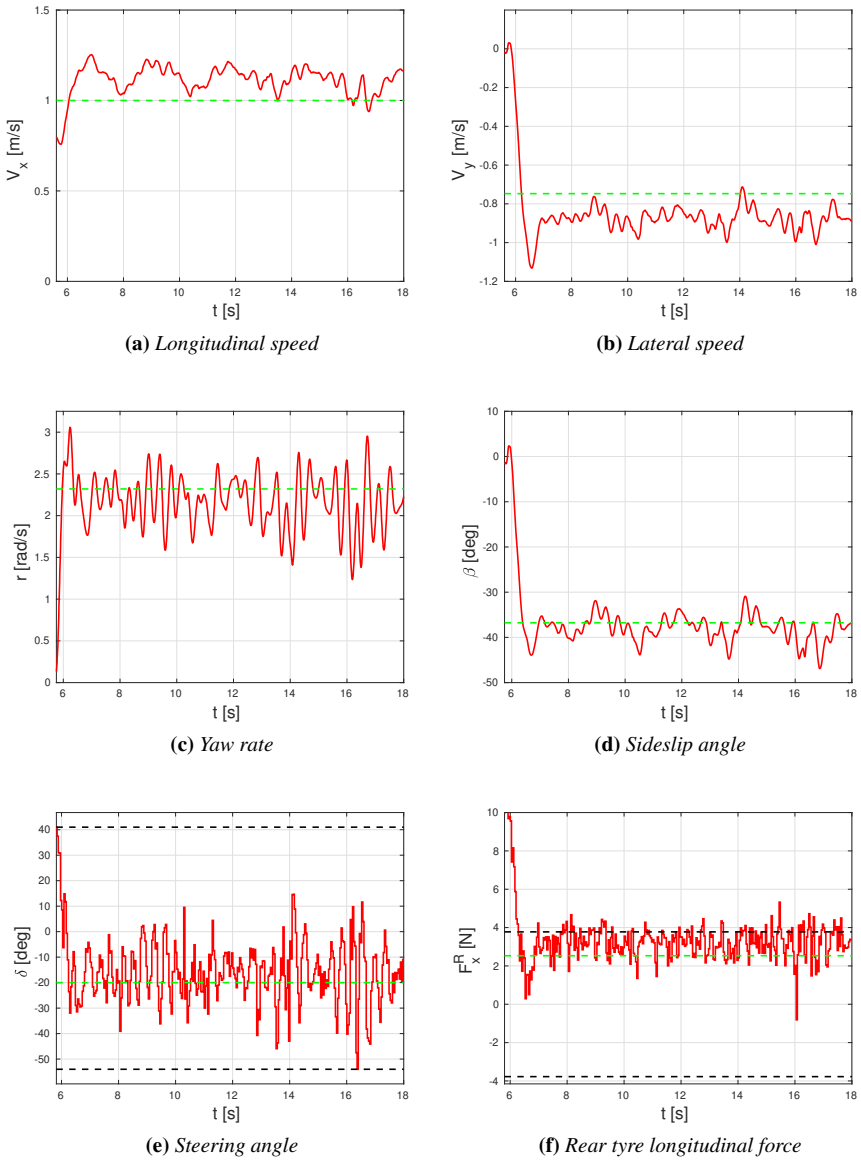

(a) *Longitudinal speed* **(b)** *Lateral speed*

(c) *Yaw rate* **(d)** *Sideslip angle*

(e) *Steering angle* **(f)** *Rear tyre longitudinal force*

Figure A.7: *Drifting stabilization on carpet surface, drifting tyre set and scaled car new configuration, with LQR controller running at* $25\,Hz$*. Experimental data as red solid line, carpet surface equilibrium value as green dashed line and actuator saturation as black dashed line*

Appendix A. Autonomous drifting and circular path tracking with LQR approach: additional experimental results

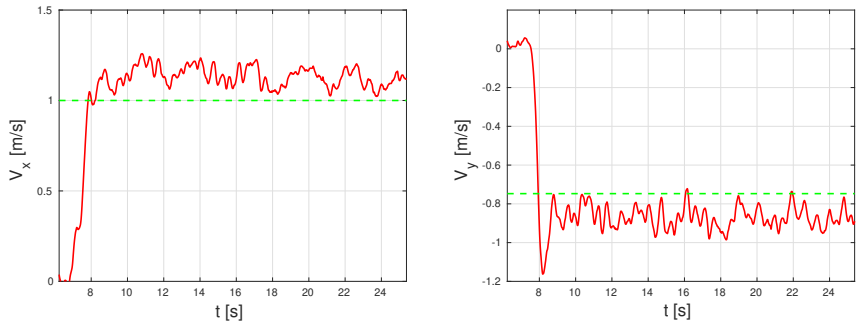

(a) *Longitudinal speed*

(b) *Lateral speed*

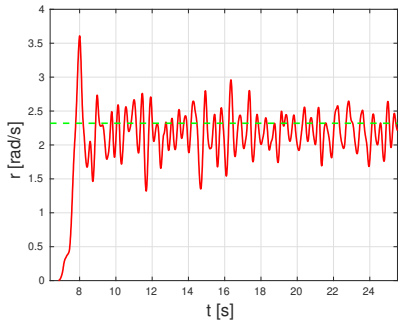

(c) *Yaw rate*

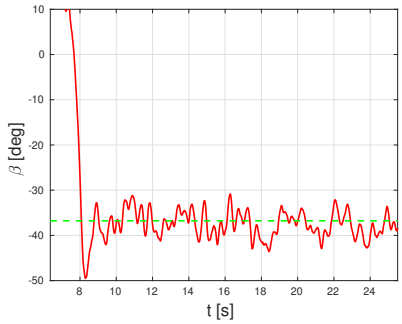

(d) *Sideslip angle*

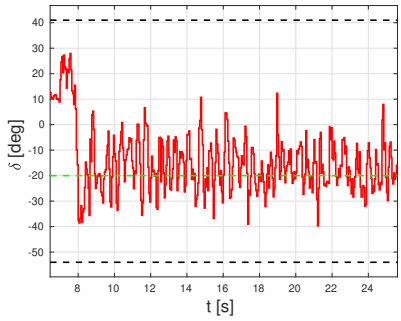

(e) *Steering angle*

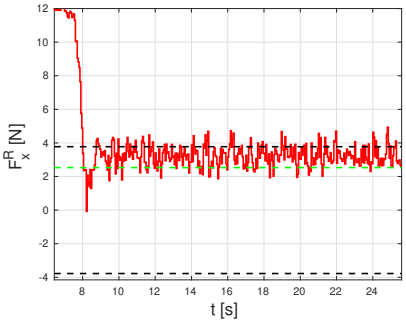

(f) *Rear tyre longitudinal force*

Figure A.8: *Drifting stabilization on carpet surface, drifting tyre set and scaled car new configuration, with LQR controller running at* $20\,Hz$*. Experimental data as red solid line, carpet surface equilibrium value as green dashed line and actuator saturation as black dashed line*

A.2 Circular drifting stabilization with integral action on path tracking error

The circular drifting controller with integral action on path tracking error, which has been presented in Section 4.2, has also been tested on wood flooring surface, assessing controller robustness against uncertainty on friction coefficient and cornering stiffness. Figs. A.9, A.10 and A.11, A.12, along with a video[1], shows the experimental results obtained.

[1] A video of these experiments is available at `https://youtu.be/ond1xtDYx7g`

Appendix A. Autonomous drifting and circular path tracking with LQR approach: additional experimental results

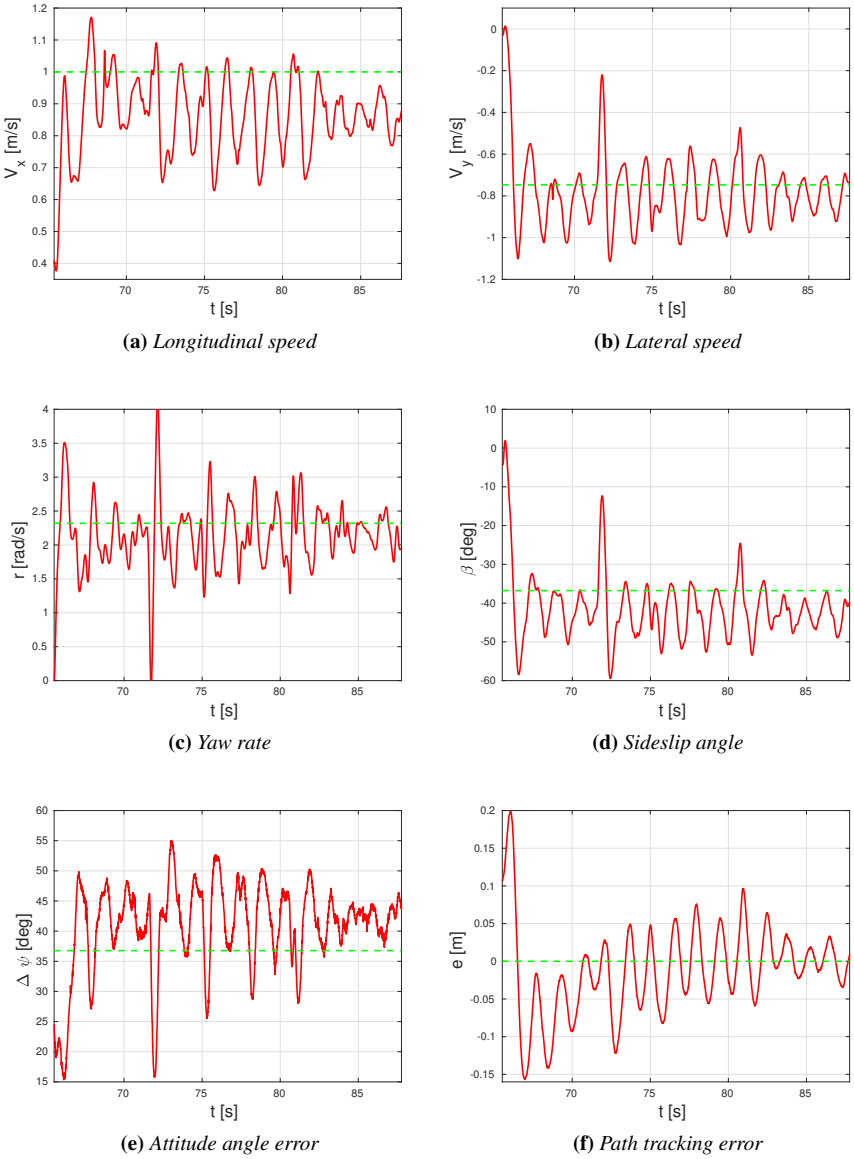

(a) *Longitudinal speed*

(b) *Lateral speed*

(c) *Yaw rate*

(d) *Sideslip angle*

(e) *Attitude angle error*

(f) *Path tracking error*

Figure A.9: *Circular drifting stabilization with path tracking error integral action, wood flooring surface, drifting tyre set and scaled car new configuration. Experimental data as red solid line, carpet surface equilibrium value as green dashed line. In this test, car started inside reference circular path*

A.2. Circular drifting stabilization with integral action on path tracking error

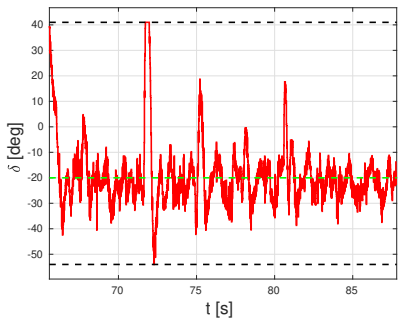

(a) *Steering angle*

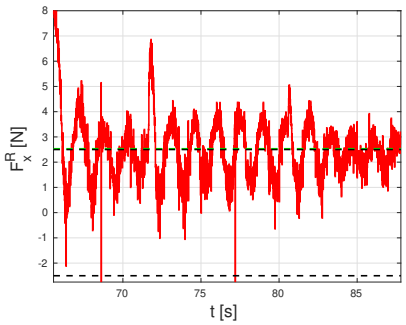

(b) *Rear tyre longitudinal force*

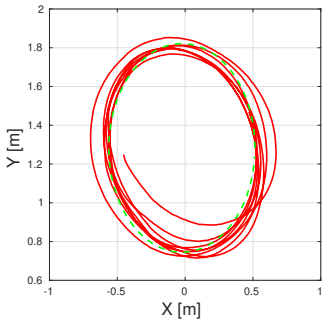

(c) *Followed path*

Figure A.10: *Circular drifting stabilization with path tracking error integral action, wood flooring surface, drifting tyre set and scaled car new configuration. Experimental data as red solid line, carpet surface equilibrium value as green dashed line and actuator saturation as black dashed line. In this test, car started inside reference circular path*

Appendix A. Autonomous drifting and circular path tracking with LQR approach: additional experimental results

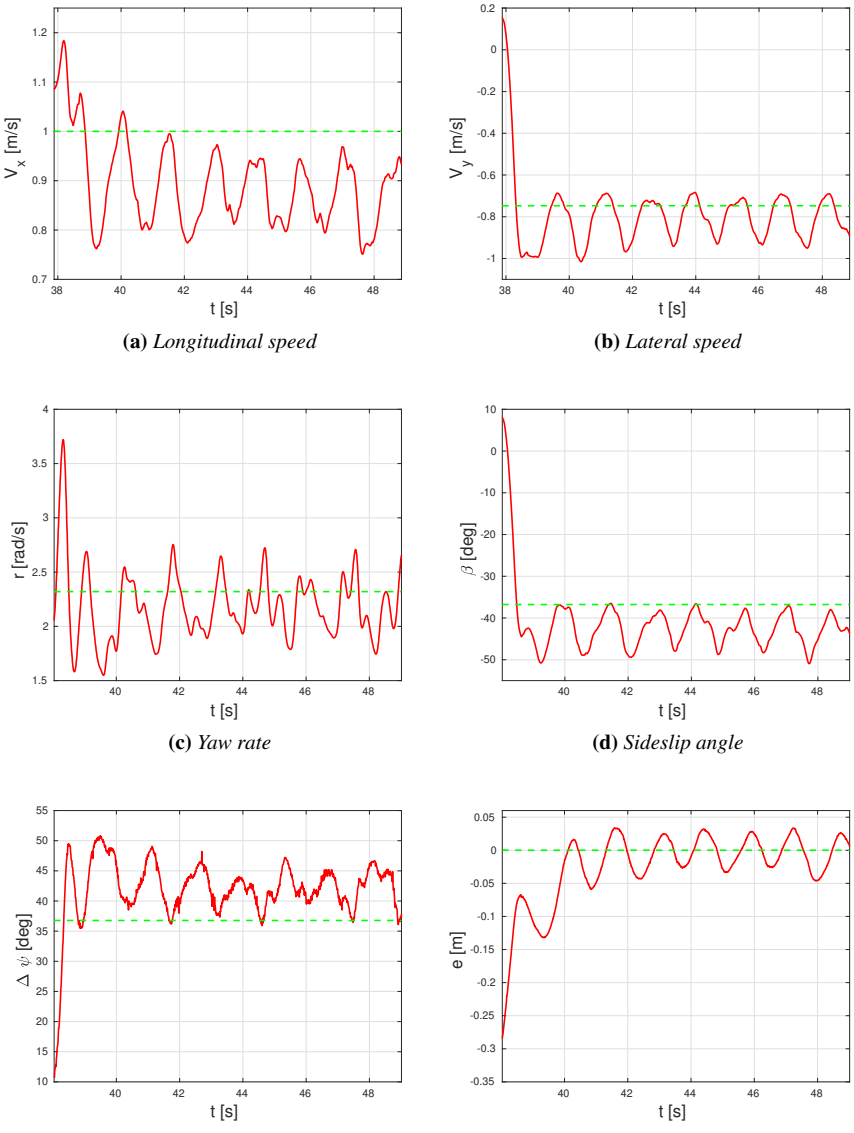

(a) *Longitudinal speed*

(b) *Lateral speed*

(c) *Yaw rate*

(d) *Sideslip angle*

(e) *Attitude angle error*

(f) *Path tracking error*

Figure A.11: *Circular drifting stabilization with path tracking error integral action, wood flooring surface, drifting tyre set and scaled car new configuration. Experimental data as red solid line, carpet surface equilibrium value as green dashed line. In this test, car started outside reference circular path*

A.2. Circular drifting stabilization with integral action on path tracking error

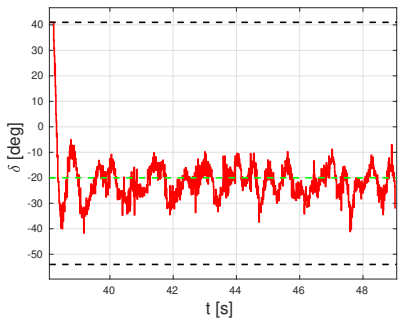

(a) *Steering angle*

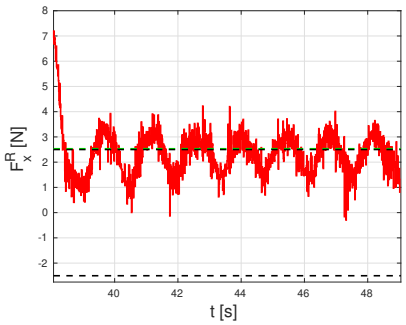

(b) *Rear tyre longitudinal force*

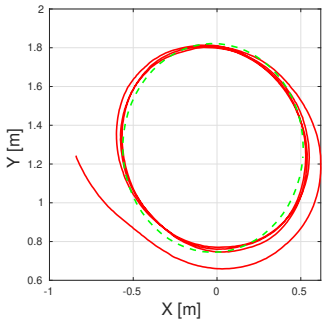

(c) *Followed path*

Figure A.12: *Circular drifting stabilization with path tracking error integral action, wood flooring surface, drifting tyre set and scaled car new configuration. Experimental data as red solid line, carpet surface equilibrium value as green dashed line and actuator saturation as black dashed line. In this test, car started outside reference circular path*

List of Figures

List of Figures

List of Tables

List of Tables

Bibliography

[1] Evan Ackerman. Toyota's gill pratt on self-driving cars and the reality of full autonomy.

[2] Jürgen Ackermann. Robust decoupling, ideal steering dynamics and yaw stabilization of 4ws cars. *Automatica*, 30(11):1761–1768, 1994.

[3] Jürgen Ackermann. *Case Studies in Car Steering*, pages 171–285. Springer London, London, 2002.

[4] M Acosta, S Kanarachos, and ME Fitzpatrick. A hybrid hierarchical rally driver model for autonomous vehicle agile maneuvering in loose surfaces. In *Int. Conf. Inf. Cont., Aut. Rob.*, pages 1–10, 2017.

[5] Heejin Ahn, Andrea Rizzi, Alessandro Colombo, and Domitilla Del Vecchio. Experimental testing of a semi-autonomous multi-vehicle collision avoidance algorithm at an intersection testbed. In *2015 IEEE/RSJ International Conference on Intelligent Robots and Systems (IROS)*, pages 4834–4839. IEEE, 2015.

[6] Luca Bascetta, Paolo Rocco, et al. Digital pole placement control of multi-mode flexible arms. In *International Congress ANIPLA 2006*, pages 1–6, 2006.

[7] Marco Baur and Luca Bascetta. An experimentally validated lqr approach to autonomous drifting stabilization. In *2019 18th European Control Conference (ECC)*, pages 732–737. IEEE, 2019.

[8] Craig E Beal and J Christian Gerdes. A method for incorporating nonlinear tire behavior into model predictive control for vehicle stability. In *Proceedings of the ASME 2010 Dynamic Systems and Control Conference*, 2010.

[9] Craig Earl Beal and J Christian Gerdes. Model predictive control for vehicle stabilization at the limits of handling. *IEEE Transactions on Control Systems Technology*, 21(4):1258–1269, 2012.

[10] Paolo Giuseppe Emilio Bolzern, Riccardo Scattolini, and Nicola Luigi Schiavoni. *Fondamenti di controlli automatici*. McGraw-Hill, 2008.

[11] Sean Brennan and Andrew Alleyne. Using a scale testbed: Controller design and evaluation. *IEEE Control Systems Magazine*, 21(3):15–26, 2001.

Bibliography

[12] Sean N Brennan. Modeling and control issues associated with scaled vehicles. Master's thesis, University of Illinois at urbana-Champaign Urbana, Ill., USA, 1999.

[13] Matthew Brown, Joseph Funke, Stephen Erlien, and J Christian Gerdes. Safe driving envelopes for path tracking in autonomous vehicles. *Control Engineering Practice*, 61:307–316, 2017.

[14] Ashwin Carvalho, Yiqi Gao, Andrew Gray, H Eric Tseng, and Francesco Borrelli. Predictive control of an autonomous ground vehicle using an iterative linearization approach. In *Intelligent Transportation Systems-(ITSC), 2013 16th International IEEE Conference on*, pages 2335–2340. IEEE, 2013.

[15] Ashwin Carvalho, Stéphanie Lefévre, Georg Schildbach, Jason Kong, and Francesco Borrelli. Automated driving: The role of forecasts and uncertainty - a control perspective. *European Journal of Control*, 24:14–32, 2015.

[16] Gianluca Cesari, Georg Schildbach, Ashwin Carvalho, and Francesco Borrelli. Scenario model predictive control for lane change assistance and autonomous driving on highways. *IEEE Intelligent Transportation Systems Magazine*, 9(3):23–35, 2017.

[17] Salim Chaib, Mariana S Netto, and Said Mammar. H/sub/spl infin//, adaptive, pid and fuzzy control: a comparison of controllers for vehicle lane keeping. In *Intelligent Vehicles Symposium, 2004 IEEE*, pages 139–144. IEEE, 2004.

[18] Matteo Corno, Alberto Lucchetti, Ivo Boniolo, and Sergio M Savaresi. Coordinated lateral and longitudinal vehicle dynamics control of a scale rc vehicle. In *2015 American Control Conference (ACC)*, pages 1433–1438. IEEE, 2015.

[19] F. Della Rossa, G. Mastinu, and C. Piccardi. Bifurcation analysis of an automobile model negotiating a curve. *Vehic. Sys. Dyn.*, 50(10):1539–1562, 2012.

[20] J. Edelmann and M. Plochl. Handling characteristics and stability of the steady-state power-slide motion of an automobile. *Regular and Chaotic Dynamics*, 14(6):682–692, 2009.

[21] Stephen M Erlien, Joseph Funke, and J Christian Gerdes. Incorporating non-linear tire dynamics into a convex approach to shared steering control. In *2014 American Control Conference*, pages 3468–3473. IEEE, 2014.

[22] Lorenzo Fagiano, Marco Lauricella, Daniele Angelosante, and Enrico Ragaini. Identification of induction motors using smart circuit breakers. *IEEE Transactions on Control Systems Technology*, 2018.

[23] Peter Fairley. Self-driving cars have a bicycle problem. *IEEE Spectrum*, 54(3):12 – 13, March 2017.

[24] Paolo Falcone, Francesco Borrelli, J Asgari, HE Tseng, and Davor Hrovat. Low complexity mpc schemes for integrated vehicle dynamics control problems. In *9th international symposium on advanced vehicle control*, 2008.

[25] Paolo Falcone, Francesco Borrelli, H Eric Tseng, Jahan Asgari, and Davor Hrovat. A hierarchical model predictive control framework for autonomous ground vehicles. In *American Control Conference, 2008*, pages 3719–3724. IEEE, 2008.

[26] Joseph Funke, Matthew Brown, Stephen M Erlien, and J Christian Gerdes. Collision avoidance and stabilization for autonomous vehicles in emergency scenarios. *IEEE Transactions on Control Systems Technology*, 25(4):1204–1216, 2016.

[27] Giancarlo Genta. *Meccanica dell'autoveicolo*. Levrotto & Bella, 5 edition, 2000.

[28] T.D. Gillespie. *Fundamentals of Vehicle Dynamics*. Premiere Series Bks. Society of Automotive Engineers, 1992.

[29] Jonathan Y Goh and J Christian Gerdes. Simultaneous stabilization and tracking of basic automobile drifting trajectories. In *Int. Vehic. Symp.*, pages 597–602, 2016.

[30] Brian Goldfain, Paul Drews, Changxi You, Matthew Barulic, Orlin Velev, Panagiotis Tsiotras, and James M Rehg. Autorally: An open platform for aggressive autonomous driving. *IEEE Control Systems Magazine*, 39(1):26–55, 2019.

[31] J Gonzales, F Zhang, K Li, and F Borrelli. Autonomous drifting with onboard sensors. In *Advanced Vehicle Control: Proceedings of the 13th International Symposium on Advanced Vehicle Control (AVEC 2016), September 13-16, 2016, Munich, Germany*, page 133, 2016.

[32] Andrew Gray, Yiqi Gao, Theresa Lin, J Karl Hedrick, H Eric Tseng, and Francesco Borrelli. Predictive control for agile semi-autonomous ground vehicles using motion primitives. In *American Control Conference (ACC), 2012*, pages 4239–4244. IEEE, 2012.

[33] M. Guiggiani. *The Science of Vehicle Dynamics: Handling, Braking, and Ride of Road and Race Cars*. SpringerLink : Bücher. Springer Netherlands, 2014.

[34] Benjamin Gutjahr, Lutz Gröll, and Moritz Werling. Lateral vehicle trajectory optimization using constrained linear time-varying mpc. *IEEE Transactions on Intelligent Transportation Systems*, 18(6):1586–1595, 2017.

[35] R.Y. Hindiyeh and J.C. Gerdes. A controller framework for autonomous drifting: Design, stability, and experimental validation. *Journal of Dynamic Systems, Measurement and Control, Transactions of the ASME*, 136(5), 2014.

[36] ISO Central Secretary. Passenger cars - straight-ahead braking on surfaces with split coefficient of friction - open-loop test method. Standard ISO 14512:1999(E), International Organization for Standardization, Geneva, CH, 1999.

[37] Edo Jelavic, J Gonzales, and Francesco Borrelli. Autonomous drift parking using a switched control strategy with onboard sensors. *IFAC-PapersOnLine*, 50(1):3714–3719, 2017.

[38] N.R. Kapania and J.C. Gerdes. Design of a feedback-feedforward steering controller for accurate path tracking and stability at the limits of handling. *Vehicle System Dynamics*, 53(12):1687–1704, 2015.

[39] Alexander Katriniok, Jan P Maschuw, Fréderic Christen, Lutz Eckstein, and Dirk Abel. Optimal vehicle dynamics control for combined longitudinal and lateral autonomous vehicle guidance. In *Control Conference (ECC), 2013 European*, pages 974–979. IEEE, 2013.

[40] Tamás Keviczky, Paolo Falcone, Francesco Borrelli, Jahan Asgari, and Davor Hrovat. Predictive control approach to autonomous vehicle steering. In *American Control Conference, 2006*, pages 6–pp. IEEE, 2006.

[41] Hassan K Khalil. Nonlinear systems. *Upper Saddle River*, 2002.

[42] Krisada Kritayakirana and J Christian Gerdes. Using the centre of percussion to design a steering controller for an autonomous race car. *Vehicle System Dynamics*, 50(sup1):33–51, 2012.

[43] Alexander Liniger, Alexander Domahidi, and Manfred Morari. Optimization-based autonomous racing of 1: 43 scale rc cars. *Optimal Control Applications and Methods*, 36(5):628–647, 2015.

[44] L. Magni and R. Scattolini. *Advanced and multivariable control*. Pitagora, 2014.

[45] Carlos Massera Filho and Denis F Wolf. Dynamic inversion-based control for front wheel drive autonomous ground vehicles near the limits of handling. In *17th International IEEE Conference on Intelligent Transportation Systems (ITSC)*, pages 2138–2143. IEEE, 2014.

[46] B. Michini, T.J. Walsh, A.-A. Agha-Mohammadi, and J.P. How. Bayesian nonparametric reward learning from demonstration. *IEEE Transactions on Robotics*, 31(2):369–386, 2015.

Bibliography

[47] Hiroshi Nakano, Ken Okayama, Jun Kinugawa, and Kazuhiro Kosuge. Control of an electric vehicle with a large sideslip angle using driving forces of four independently-driven wheels and steer angle of front wheels. In *Int. Conf. Adv. Int. Mech.*, pages 1073–1078, 2014.

[48] Hans Pacejka. *Tire and vehicle dynamics*. Elsevier, 2005.

[49] Satyajit Patwardhan, Han-Shue Tan, and Jiirgen Guldner. A general framework for automatic steering control: System analysis. In *American Control Conference, 1997. Proceedings of the 1997*, volume 3, pages 1598–1602. IEEE, 1997.

[50] Steven C Peters, Emilio Frazzoli, and Karl Iagnemma. Differential flatness of a front-steered vehicle with tire force control. In *Intelligent Robots and Systems (IROS), 2011 IEEE/RSJ International Conference on*, pages 298–304. IEEE, 2011.

[51] Vaughan Pratt. Direct least-squares fitting of algebraic surfaces. In *ACM SIGGRAPH computer graphics*, volume 21, pages 145–152. ACM, 1987.

[52] E Raffone, C Rei, and M Rossi. Optimal look-ahead vehicle lane centering control design and application for mid-high speed and curved roads. In *2019 18th European Control Conference (ECC)*, pages 2024–2029. IEEE, 2019.

[53] R. Rajamani. *Vehicle Dynamics and Control*. Mechanical Engineering Series. Springer US, 2011.

[54] SAE. Vehicle Dynamics Terminology. Technical Report J 670, January 2008.

[55] SAE. Taxonomy and Definitions for Terms Related to On-Road Motor Vehicle Automated Driving Systems. Technical Report J 3016, January 2014.

[56] Donald Selmanaj, Matteo Corno, Giulio Panzani, and Sergio M Savaresi. Vehicle sideslip estimation: A kinematic based approach. *Control Engineering Practice*, 67:1–12, 2017.

[57] John K Subosits and J Christian Gerdes. A synthetic input approach to slip angle based steering control for autonomous vehicles. In *2017 American Control Conference (ACC)*, pages 2297–2302. IEEE, 2017.

[58] Gilles Tagne, Reine Talj, and Ali Charara. Higher-order sliding mode control for lateral dynamics of autonomous vehicles, with experimental validation. In *2013 IEEE Intelligent Vehicles Symposium (IV)*, pages 678–683. IEEE, 2013.

[59] D. Tavernini, M. Massaro, E. Velenis, D.I. Katzourakis, and R. Lot. Minimum time cornering: The effect of road surface and car transmission layout. *Vehicle System Dynamics*, 51(10):1533–1547, 2013.

[60] D. Tavernini, E. Velenis, R. Lot, and M. Massaro. The optimality of the handbrake cornering technique. *Journal of Dynamic Systems, Measurement and Control, Transactions of the ASME*, 136(4), 2014.

[61] E. Velenis, P. Tsiotras, and J. Lu. Optimality properties and driver input parameterization for trail-braking cornering. *European Journal of Control*, 14(4):308–320, 2008.

[62] Efstathios Velenis, Diomidis Katzourakis, Emilio Frazzoli, Panagiotis Tsiotras, and Riender Happee. Steady-state drifting stabilization of rwd vehicles. *Control Engineering Practice*, 19(11):1363–1376, 2011.

[63] C. Voser, R.Y. Hindiyeh, and J.C. Gerdes. Analysis and control of high sideslip manoeuvres. *Vehicle System Dynamics*, 48(SUPPL. 1):317–336, 2010.

[64] M. Werling, P. Reinisch, and L. Gröll. Robust power-slide control for a production vehicle. *International Journal of Vehicle Autonomous Systems*, 13(1):27–42, 2015.

[65] Grady Williams, Paul Drews, Brian Goldfain, James M Rehg, and Evangelos A Theodorou. Aggressive driving with model predictive path integral control. In *2016 IEEE International Conference on Robotics and Automation (ICRA)*, pages 1433–1440. IEEE, 2016.

[66] F Zhang, J Gonzales, K Li, and F Borrelli. Autonomous drift cornering with mixed open-loop and closed-loop control. *IFAC-PapersOnLine*, 50(1):1916–1922, 2017.